Computational study of flow structure and forces on a cylinder vibrating transversely and in-line to a steady flow: effects of sub-harmonic excitation

by

Paris G. Perdikaris

Submitted to the Department of Naval Architecture and Marine Engineering
in partial fulfillment of the requirements for the degrees of

Diploma in Naval Architecture

and

Marine Engineering

at the

NATIONAL TECHNICAL UNIVERSITY OF ATHENS

June 2009

Signature of Author .....
Department of Naval Architecture and Marine Engineering
5 June 2009

Certified by .....
George S. Triantafyllou
Professor, Division of Marine Hydrodynamics
Research Head, Thesis Supervisor

Certified by .....
Lambros Kaiktsis
Assistant Professor, Division of Marine Engineering
Thesis Supervisor

Accepted by .....
George D. Tzabiras
Professor, Division of Marine Hydrodynamics

Computational study of flow structure and forces on a cylinder vibrating transversely and in-line to a steady flow: effects of sub-harmonic excitation

by

Paris G. Perdikaris

Submitted to the Department of Naval Architecture and Marine Engineering
on 5 June 2009, in partial fulfillment of the
requirements for the degrees of
Diploma in Naval Architecture
and
Marine Engineering

Abstract

In this work, we present computational results of the flow structure and forces on a cylinder vibrating both transversely and in-line to a uniform stream. The in-line frequency is equal to twice the transverse frequency, while the ratio of the in-line to the transverse oscillation amplitude is equal to 0.2, 0.4 or 0.6. The cylinder thus follows an "eight"-like trajectory, emulating the motion of real cylindrical structures undergoing vortex-induced vibrations. For a flow from left to right, we distinguish between a "counter-clockwise" mode (if the upper part of the trajectory is traversed counter-clockwise) and a "clockwise" mode (if the upper part of the trajectory is traversed clockwise). Here, we use a spectral element method, and perform simulations for a Reynolds number of 400. We focus on a value of the transverse oscillation frequency equal to half the natural frequency of the Kármán vortex street (sub-harmonic excitation). Results are compared against cases corresponding to resonant and near-resonant forcing. We find that, in all cases, results are greatly influenced by the direction in which the cylinder is traversed. In particular, the "counter-clockwise" mode is characterized by higher values of the forces acting on the cylinder, as well as by higher values of the power transfer from the flow to the cylinder. The case of sub-harmonic excitation is unique, in that the power transfer remains negative for all values of the non-dimensional oscillation amplitude, i.e. corresponds to damping. Flow visualization reveals a variety of vortex patterns in the wake, with complex vortex streets at large oscillation amplitudes.

Research Head, Thesis Supervisor: George S. Triantafyllou
Title: Professor, Division of Marine Hydrodynamics

Thesis Supervisor: Lambros Kaiktsis
Title: Assistant Professor, Division of Marine Engineering

Υπολογιστική μελέτη της αλληλεπίδρασης ροής με κατασκευή που εκτελεί υπο-αρμονική ταλάντωση

Πάρις-Γεώργιος Περδικάρης

Διπλωματική Εργασία

Εθνικό Μετσόβιο Πολυτεχνείο
Τμήμα Ναυπηγών Μηχανολόγων Μηχανικών
Τομέας Ναυτικής και Θαλάσσιας Υδροδυναμικής

Περίληψη

Στην παρούσα εργασία παρουσιάζουμε υπολογιστικά αποτελέσματα της ροής και των δυνάμεων που ασκούνται σε κύλινδρο ο οποίος εκτελεί υπο-αρμονική ταλάντωση με δύο βαθμούς ελευθερίας σε ρεύμα σταθερής ταχύτητας. Η συχνότητα της ταλάντωσης στην παράλληλη με τη ροή κατεύθυνση είναι ίση με το διπλάσιο της αντίστοιχης συχνότητας στην κάθετη κατεύθυνση. Ο αδιάστατος λόγος του πλάτους της ταλάντωσης στην παράλληλη προς την εγκάρσια κατεύθυνση λαμβάνει τιμές απο μηδέν (ταλάντωση του κυλίνδρου μόνο εγκάρσια στη ροή) εως άπειρο (ταλάντωση του κυλίνδρου μόνο παράλληλα προς τη ροή). Για όλες τις ενδιάμεσες τιμές, ο κύλιδρος ακολουθεί τροχιά στον διδιάστατο χώρο διάγράφοντας τον αριθμό 8, εξομοιώνοτας έτσι την κίνηση πραγματικών κυλινδρικών κατασκευών που εκτελούν ταλάντωση λόγω σχηματισμού δινών στον ομόρρου τους. Θεωρώντας μια σταθερή ροή ρευστού απο τα αριστερά προς τα δεξιά, διαχωρίζουμε μεταξύ μιας "αντι-ωρολογιακής" τροχιάς (όταν το άνω τμήμα της τροχιάς διαγράφεται με φορά αντίθετη των δεικτών του ρολογίου) και μιας "ωρολογιακής" τροχιάς (όταν το άνω τμήμα της τροχιάς διαγράφεται με τη φορά των δεικτών του ρολογιού). Η αριθμητική επίλυση των εξισώσεων Navier-Stokes επιτυγχάνεται με χρήση μιας μεθόδου φασματικών πεπερασμένων στοιχείων. Η προσομοίωση γίνεται για διδιάστατη ροή σε αριθμό Reynolds ίσο με 400. Η μελέτη μας επικεντρώνεται σε τιμές της συχνότητας ταλάντωσης στη διεύθυνση κάθετα στη ροή ίσες με το μισό της φυσικής συχνότητας σχηματισμού του δρόμου δινών Von Kármán (υπο-αρμονική διέγερση). Τα αποτελέσματα που προκύπτουν συγκρίνονται με αντίστοιχες περιπτώσεις επιβαλλόμενων ταλαντώσεων με συχνότητα στην περιοχή γύρω απο τη φυσική συχνότητα του δρόμου δινών (συχνότητα Strouhal). Σε όλες τις μελετηθήσες περιπτώσεις, τα χαρακτηριστικά της ροής επιρρεάζονται άμεσα απο την τροχιά που ακολουθεί η ταλάντωση του κυλίνδρου. Συγκεκριμένα, κατά την "αντι-ωρολογιακή" τροχιά ταλάντωσης, παρατηρούμε υψηλότερες τιμές των δυνάμεων που ασκούνται στον κύλινδρο, καθώς επίσης και υψηλότερες τιμές της μεταφερόμενης ισχύος απο τη ροή στη κατασκευή. Η περίπτωση της υπο-αρμονικής διέγερσης ειναι μοναδική διότι η μεταφερόμενη ενέργεια απο τη ροή στον κύλινδρο λαμβάνει συνεχώς αρνητικές τιμές για όλα τα εξεταζόμενα πλάτη διέγερσης, γεγονός που υποδηλώνει πως η ροή δρά ως αποσβεστήρας στην ταλάντωση του κυλίνδρου. Τέλος, η οπτικοποίηση των αποτελεσμάτων φανερώνει μια πληθώρα σχηματισμών δινών στον ομόρρου, με χαρακτηριστικό τις συνήθεις μορφές δινών στην περίπτωση της υπο-αρμονικής διέγερσης χαμηλού πλάτους (δρόμοι δινών τύπου 2S) και τους πλέον περίπλοκους σχηματισμούς για περιπτώσεις διέγερσης μεγάλου πλάτους.

Εξεταστική Επιτροπή :

Επιβλέπων : **Τριανταφύλλου Γεώργιος**, *Καθηγητής*, Τομέας Ναυτικής και Θαλάσσιας Υδροδυναμικής
Επιβλέπων : **Καϊκτσής Λάμπρος**, *Επίκουρος Καθηγητής*, Τομέας Ναυτικής Μηχανολογίας
Μέλος : **Τζαμπίρας Γεώργιος**, *Καθηγητής*, Τομέας Ναυτικής και Θαλάσσιας Υδροδυναμικής

05/06/2009

Acknowledgements

This section is devoted to everyone who helped and assisted me during the elaboration of this thesis. Many people deserve heartfelt thanks for their time, patience and desire to assist me during my last years of study at NTUA.

First of all I wish to thank my supervisors, Professor George Triantafyllou and Assistant Professor Lambros Kaiktsis for their technical vision, guidance and support throughout the research process. This thesis was inspired by their ideas. Both professionally and personally, I feel truly grateful to have such supervisors, continuously committed to actively participate in the research of their students. Moreover, I am deeply indebted for their unconditional support and encouragement towards my decision to pursue graduate studies.

I also wish to express my thanks to Professor George Tzabiras not only for his time and patience but also for his will to support me with his recommendations.

I would like to thank each member of my family for constant encouragement throughout these years. It is certainly assuring to know how much they love and support me. This thesis is dedicated to them with boundless appreciation.

Last but not least I would like to thank all my great friends ("you know who you are") for being there for me whenever I need them.

Paris Perdikaris,
March 2009.

Contents

List of Figures

Nomenclature

General

- Symbols are generally defined where they appear in the text for the first time.

- Over-dots signify differentiation with respect to time.

- Over-line signify mean value or generalized value.

Abbreviations

CFD	Computational Fluid Dynamics
DNS	Direct Numerical Simulation
DOF	Degrees of freedom
DVM	Discrete vortex method
Eqn.	Equation
Fig.	Figure
MIT	Massachusetts Institute of Technology
NTUA	National Technical University of Athens
PDE	Partial Differential Equation
RANS	Reynolds averaged Navier-Stokes
rms	Root mean square
Sec.	Section
VIV	Vortex induced vibrations

Roman Symbols

A	Oscillation amplitude
A_y	Transverse amplitude (y-direction)
A_x	In-line amplitude (x-direction)
A/D	Reduced amplitude
A_y/D	Transverse reduced amplitude (y-direction)
A_x/D	In-line reduced amplitude (x-direction)
C_D	Drag coefficient
C_{D_a}	Inertia force (added mass) coefficient in in-line direction
C_{D_v}	Excitation force coefficient in in-line direction
$< C_D >$	Time-averaged drag coefficient
$C_{D,rms}$	Drag coefficient r.m.s fluctuations
C_L	Lift coefficient
C_{L_a}	Inertia force (added mass) coefficient in transverse direction
C_{L_v}	Excitation force coefficient in transverse direction
$< C_L >$	Time-averaged lift coefficient
$C_{L,rms}$	Drag coefficient r.m.s fluctuations
C_M	Inertia force (added mass) coefficient in transverse direction
C_{M_x}	Inertia force (added mass) coefficient in in-line direction
D	Cylinder diameter
i	Imaginary unit, $\sqrt{-1}$
F	Force; Reduced oscillation frequency, $\frac{f_{ex}}{f_{st}}$
F_{hydro}	Total hydrodynamic force
F_x	Hydrodynamic force in in-line direction
F_y	Hydrodynamic force in transverse direction
F_v	Excitation force in transverse direction
F_M	Inertia (added mass) force in transverse direction
f	Frequency
f_{ex}	Excitation frequency
f_{st}	Natural frequency of the Kármán vortex street (Strouhal frequency)
P	Total power transfer
P_x	Power transfer in in-line direction
P_y	Power transfer in transverse direction
p	Fluid pressure
R_e	Reynolds number, $\frac{U_\infty D}{\nu}$
T	Oscillation period
t	Time
U_∞	Fluid velocity far upstream
$\overrightarrow{u}$	Fluid velocity vector

Greek Symbols

δ	Boundary layer thickness
ϵ	Excitation amplitudes ratio, $\frac{A_x}{A_y}$
ξ	Nondimensional excitation amplitude-over-diameter ratio, A/D
λ	Wavelength
η	Instantaneous cylinder displacement from the mean position
ν	Kinematic viscosity
π	Pi number, 3.141592..
ρ	Fluid density
ω	Circular frequency, $2\pi f$

Chapter 1

Introduction

1.1 Motivation and Background

It is widely known that vortex induced vibrations (VIV) are possible whenever a bluff (not streamlined) object is exposed to a flowing fluid. In most engineering applications, the induced vibrations of interest are those of the bluff body itself, typically a beam or a cable exposed to a cross flow of air or water, examples of which are bridges, stacks, transmission lines, aircraft control surfaces, offshore structures, thermowells, engines, heat exchangers, marine cables, towed cables, drilling and production risers in petroleum production, mooring cables, moored structures, tethered structures, buoyancy and spar hulls, pipelines, cable-laying, members of jacketed structures, and other hydrodynamic and hydroacoustic applications. Evidently, such structures, may be damaged or even fail by severe oscillations of this type.

In recent years, a major aim in the oil and gas industry is to deliver fluids from subterranean sources to the surface at the lowest costs compatible with the constraints imposed by technology and the environment. These constraints are often related; despite continuing developments there is a need to fully address a number of complex problems that remain poorly understood. Such problems affect both the design of new structures and the cost effectiveness of existing operations. Specifically, new deep water oil and gas fields have been developed in areas with very irregular seabed conditions, and this trend is expected to continue in the coming years. Ocean currents will here lead to separated flow and vortex shedding. These vortices will again induce forces on the structure that may result in horizontal and vertical oscillations. These oscillations will give time varying stresses in the structure, and hence lead to accumulation of fatigue damage.

One of the most important challenges is to effectively predict the dynamical response of offshore marine risers and under-sea pipelines to fluid dynamic forces. These can arise from the fluids being conveyed inside flexible pipelines and from sea currents that produce oscillatory lift and drag on structures. Great savings in cost are possible by being able to predict fatigue rates in marine-risers due to environmental and fluid excitation.

A significant cause of fatigue is vortex induced vibrations (VIV) due to sea currents. As the frequency of vortex shedding approaches one of the natural frequencies of a structure, resonant vibrations often occur, the amplitude of which depends on the damping in the system and the motion of the fluid relative to the structure. Such oscillations may lead the system to a "lock-in" state that may cause hazardous amplification and fatigue failure.

Despite several decades of intensive efforts to construct effective models that can accurately account for VIV in material structures over useful parameter domains most analyses rely on semi-empirical formulations that employ considerable amounts of experimental data as input. One of the important drawbacks of the empirical models is that they rarely treat the continuum mechanics of the structural elements that initiate vortex shedding in sufficient generality for them to be applicable to the problem of VIV in marine risers and flexible pipelines. In particular the existence of coupled torsional and flexural modes of vibration will modify the vortex shedding pattern in ways not accommodated in such models. Therefore, although some models have the virtue of simplicity, by employing a small number of effective degrees of freedom to approximate both the continuum nature of the structure and the fluid they are inevitably of limited applicability.

It is straightforward to realize that a failure of a submarine structure (a pipeline for example) is considered unacceptable from an environmental perspective and repair of deep water structures is also extremely expensive. Hence, the acceptable probability of failure is low (typically 10^{-4}). Due to the uncertainty in the models for prediction of fatigue damage, high safety factors are applied on the estimated result in order to achieve the desired safety level. Finally, increased confidence in fatigue rate predictions would yield enormous future benefits to the oil and gas industry. It could permit the introduction of fundamentally new concepts that were not previously considered feasible, including the use of larger diameter risers, steel catenary risers and large multiple arrays leading to increased production rates.

1.2 Approach of the Present Work

The work presented in this thesis integrates the previous studies of L.Kaiktsis and G.S.Triantafyllou [1], [2] on computational simulations of the flow structure and forces acting on a vibrating cylinder in a steady stream. Particularly, in this work we examine the case of excitation at a frequency lower than the natural frequency of the von Kármán vortex street (sub-harmonic forcing).

As can be seen in Fig.1.2.1(b), taken from Blevins [3], a cylinder may exhibit excitation at frequencies different than the natural frequency of the Kármán vortex street. It is legitimate to notice that sub-harmonic excitation may be important for flow-induced vibrations, especially if it leads to the formation of a "locked-in" wake.

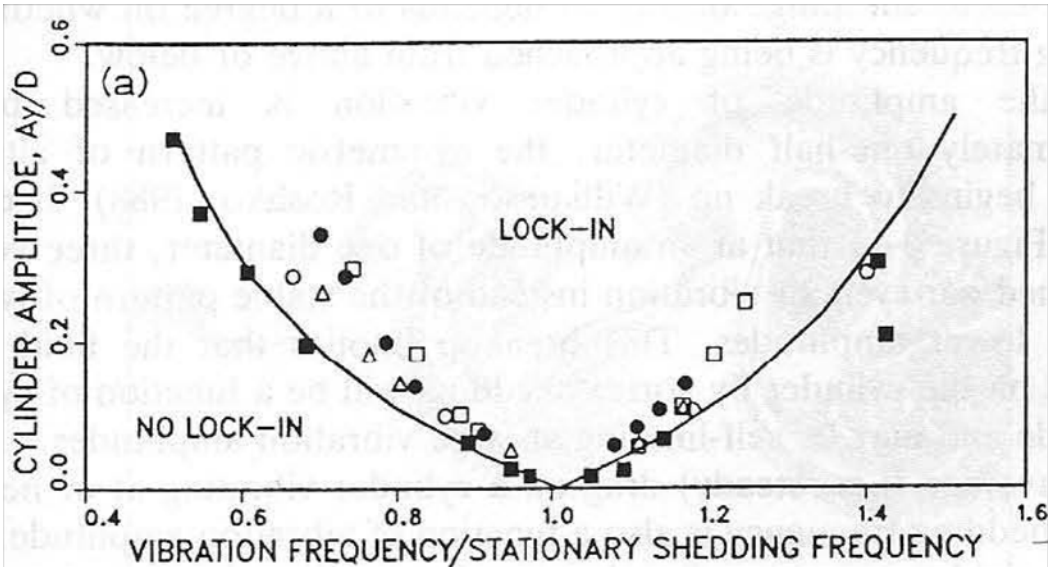

(a)

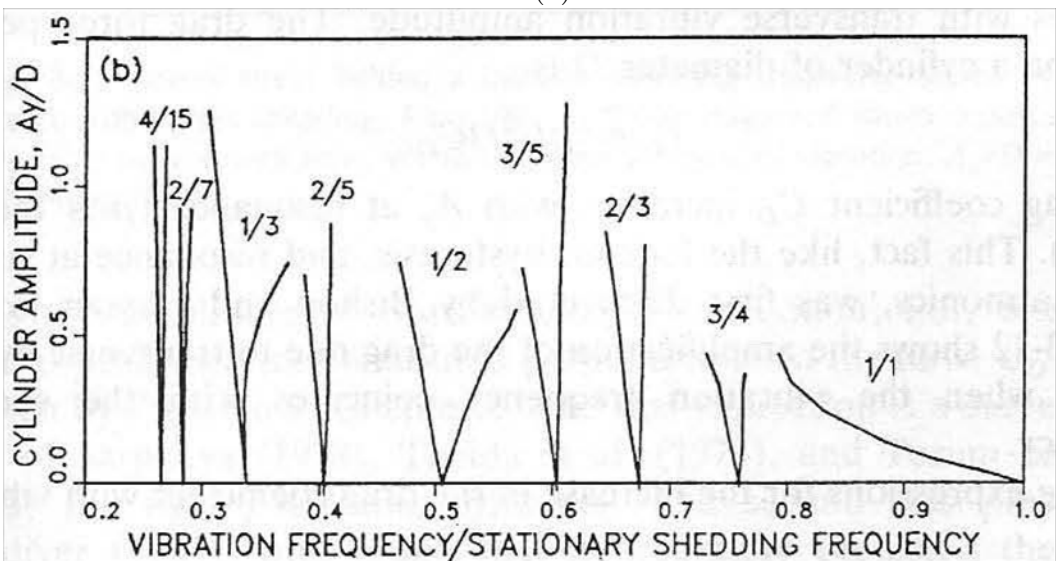

(b)

Figure 1.2.1: Lock-in bands for synchronization of vortex shedding with transverse cylinder vibration. A_y is the amplitude of the transverse oscillation and D the cylinder diameter. Experimental data: Koopman (1967), $\square$ for $R_e = 100$, $\bullet$ for $R_e = 200$ and $\triangle$ for $R_e = 300$; Stansby (1976), $\blacksquare$ for $R_e = 3600$, $\bigcirc$ for $R_e = 9200$; Olinger and Sreenivasan (1988) for sub-harmonic bands.

Vortex induced vibration of structures has been the subject of extensive research for several decades. However, the response in the in-line direction has often been neglected in earlier VIV studies mainly because the transverse (cross flow) response amplitudes are larger. Yet, studies have shown that fatigue damage due to in-line response may become significant and even more critical than the cross flow (transverse) response. Two reasons exist for this:

1. The in-line response is initiated at lower current velocity than the transverse response, and will hence take place more often.

2. The in-line response will take place at two times the frequency of the transverse response, which practically means that number of stress cycles due to in-line vibrations will become two times the number of transverse cycles.

Moreover, it is well known that vortex-induced vibrations of cylinder are often characterized by an "eight"-like trajectory and that in-line oscillations of the cylinder can significantly alter the fluid forces on the cylinder. Hence, in order to perform meaningful simulations of the phenomena, one should take into consideration both the in-line and transverse oscillation directions.

Driven by the above and extending the previous studies of Kaiktsis and Triantafyllou [1], [2] (resonant forcing simulations), this work presents a computational study of the flow structure and forces on a cylinder vibrating both transversely and in-line to a uniform stream for the case of forcing at below the natural frequency of the von Kármán vortex street. The main question is whether this case can lead to "lock-in" regions, self-excited vibrations of the cylinder and positive energy transfer from the fluid flow to the vibrating structure.

Chapter 2

Theoretical Background

The theoretical background of the present work is formed by the basic concepts of fluid mechanics. The reader is assumed to be familiar with these concepts, so only some basic definitions and results are summarized in this chapter mainly for establishing a consistent system of notation and later reference. We briefly cover the topics of the Navier-Stokes and Bernoulli equations, boundary layers and vortex formation, vortex shedding and vortex shedding modes as well as flow regimes.

Moreover, another intention of this chapter is to give a brief introduction to the phenomenology of VIV, including the main characteristics of vortex induced vibrations and a summary of the most significant scientific methods used for the investigation and prediction of VIV.

For further information and details regarding to the prescribed topics, the reader is referred to the corresponding bibliography ([3]-[9]).

2.1 Vortex Shedding

2.1.1 The Navier-Stokes Equation

Incompressible viscous fluid flows are described by the Navier-Stokes equation:

$$\frac{\partial \overrightarrow{u}}{\partial t} + \overrightarrow{u} \cdot \nabla \overrightarrow{u} = -\frac{1}{\rho}\nabla p + v\nabla^2 \overrightarrow{u} + \frac{1}{\rho}\overrightarrow{F} \tag{2.1.1}$$

where $\overrightarrow{u}$ is the fluid velocity vector $[u\ v\ w]^T$, ∇ is the differential operator, ρ is the density of the fluid, p is the pressure, v is the kinematic viscosity and $\overrightarrow{F}$ is the body force term. Ignoring the effects of viscosity, the Navier-Stokes equation reduces to the well known Bernoulli equation:

$$\rho\frac{\partial \phi}{\partial t} + p + \frac{1}{2}\rho U_\infty^2 + \rho g z = \text{constant} \tag{2.1.2}$$

2.1.2 Boundary Layer and Vortex Formation

In an ideal fluid the flow lines around a cylinder in uniform current can be drawn as indicated in Fig.2.1.1. For such flow conditions, also referred to as potential flow, the water particles will have the same velocity in the region of the downstream stagnation point as in the upstream. Hence, the water particles are accelerated upstream, reaching a maximum velocity at $\vartheta = 90°$, and decelerated

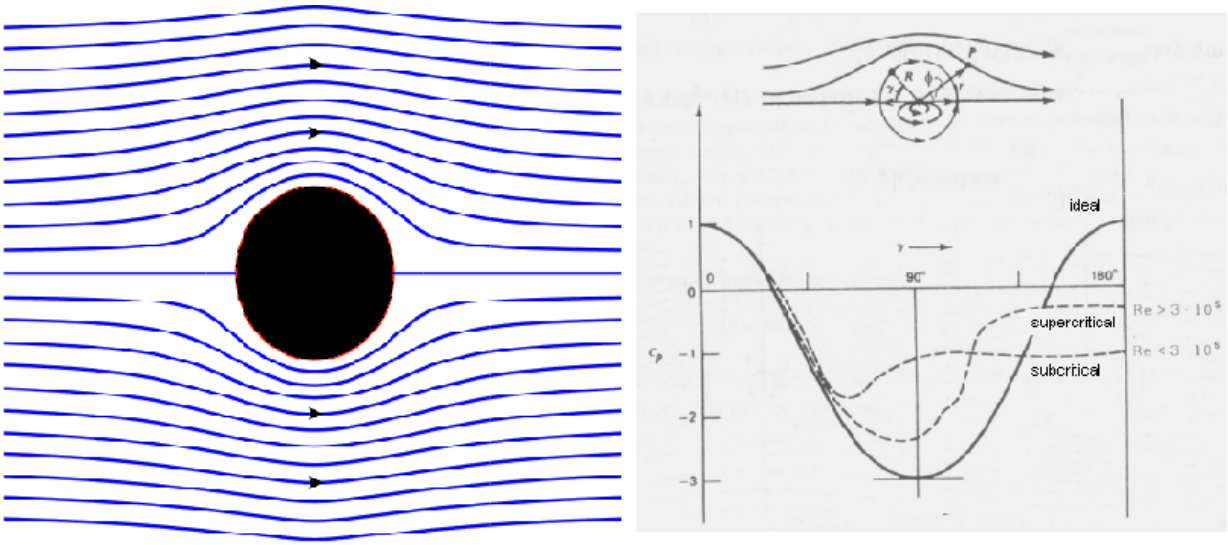

Figure 2.1.1: Potential flow streamlines and pressure distribution (Tsagaris 1995).

downstream. For this ideal fluid case the Bernoulli equation is valid (see Eq.2.1.2), and we readily see that velocity variation causes a pressure drop upstream and a pressure increase downstream. The diagram presented in Fig.2.1.1 presents the pressure distribution over the cylinder for an ideal fluid. The pressure distribution is symmetric, leading to zero drag, which is known as d'Alembert's paradox. In a viscous flow the particles close to the cylinder will loose energy due to friction. The particles may then not have enough kinetic energy to meet the increased pressure field downstream. In the case of viscous flows, the pressure distribution is asymmetric. This leads to a drag force on the cylinder.

When the Reynolds number is large one might think that the viscosity could be ignored altogether, in which case we return to nonviscous fluid mechanics. However, we once again encounter d'Alembert's paradox–that a nonviscous fluid exerts no drag on a solid body–so we are at a loss when it comes to explaining aerodynamic drag. The important insight in resolving this paradox is due to L. Prandtl, who in 1904 suggested that the viscosity could be ignored everywhere except in a thin layer close to the surface of a body. Understanding the behavior of this boundary layer has been crucial to the development of modern fluid mechanics and aerodynamics.

The boundary layer is the layer in which the flow velocity is increased from zero at the body surface to the free stream velocity at some distance away from the surface, see Fig.2.1.2. The fluid field can then be divided into two parts:

1. Near the body surface where the velocity gradient normal to the body surface is large, and the shear stress can not be neglected.

2. Outside the boundary layer where the viscosity can be neglected and the flow can be determined by potential theory, i.e. the Bernoulli equation is valid (Eq.2.1.2).

Several ways of defining the thickness, δ, of the boundary layer have been proposed. One is to define the thickness as the distance between the surface and where the flow velocity is 99% of the free flow velocity. The boundary layer

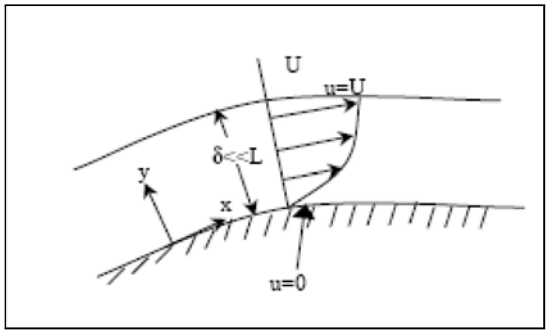

Figure 2.1.2: Boundary layer sketch.

thickness increases with increasing viscosity. When the kinetic energy of the water particles in the boundary layer is not high enough to overcome the downstream pressure field, the flow will separate from the cylinder. The point on the cylinder where this happens is referred to as the separation point. Upstream the separation point is the boundary layer region. Downstream the separation point is the wake region. The continuation of the boundary layer, downstream the separation point, is referred to as the shear layer.

In general, the point of separation on a cylinder depends not only on the pressure gradient but also on the type of unsteadiness of the ambient flow (e.g., sinusoidal), turbulence upstream of the separation points, roughness of the surface or other excrescences, symmetry or the asymmetry of the cylinder, taper along the rod, presence of salient edges, and the mode of vortex (or vorticity) shedding.

In most situations it is inevitable that the boundary layer becomes detached from a solid body, as in Fig.2.1.3. This boundary layer separation results in a large increase in the drag on the body. We can understand this by returning to the flow of a nonviscous fluid around a cylinder. The pressure distribution is the same on the downstream side of the cylinder as on the upstream side; thus, there were no unbalanced forces on the cylinder and therefore no drag (d'Alembert's paradox again!). If the flow of a viscous fluid about a body is such that the boundary layer remains attached, then we have almost the same result–we'll just have a small drag due to the skin friction. However, if the boundary layer separates from the cylinder, then the pressure on the downstream side of the cylinder is essentially constant, and equal to the low pressure on the top and bottom points of the cylinder. This pressure is much lower than the large pressure which occurs at the stagnation point on the upstream side of the cylinder, leading to a pressure imbalance and a large pressure drag on the cylinder. For instance, for a cylinder in a flow with a Reynolds number in the range $10^3 \prec R_e \prec 10^5$, the boundary layer separates and the coefficient of drag is $C_D \sim 1.2$, much larger that the coefficient of drag due to skin friction, which is estimated to be about 10^{-2}(see Fig.2.1.4).

Back flow from behind the cylinder meets with the flow from ahead in the separation point and subsequently advances outwards, separating the shear layer from the cylinder. The vortex formed behind the cylinder feeds on the circulation from the separated shear layer. As it grows, it attracts the shear layer from the other side of the wake. The approaching shear layer with oppositely signed circulation eventually cuts off the supply of vorticity to the growing vortex. The vortex is then shed and moves downstream with the local velocity and together with other vortices form the von Kármán vortex street (see Fig. 2.1.5).

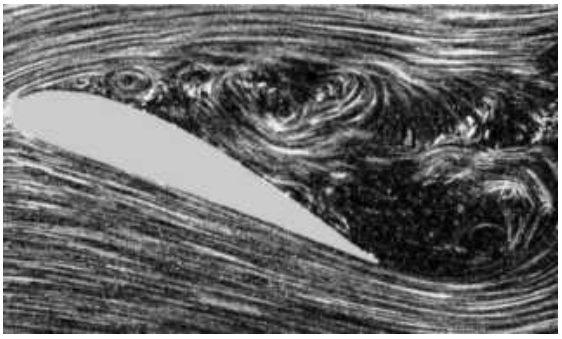

Figure 2.1.3: Airflow separating from a wing which is at a high angle of attack.

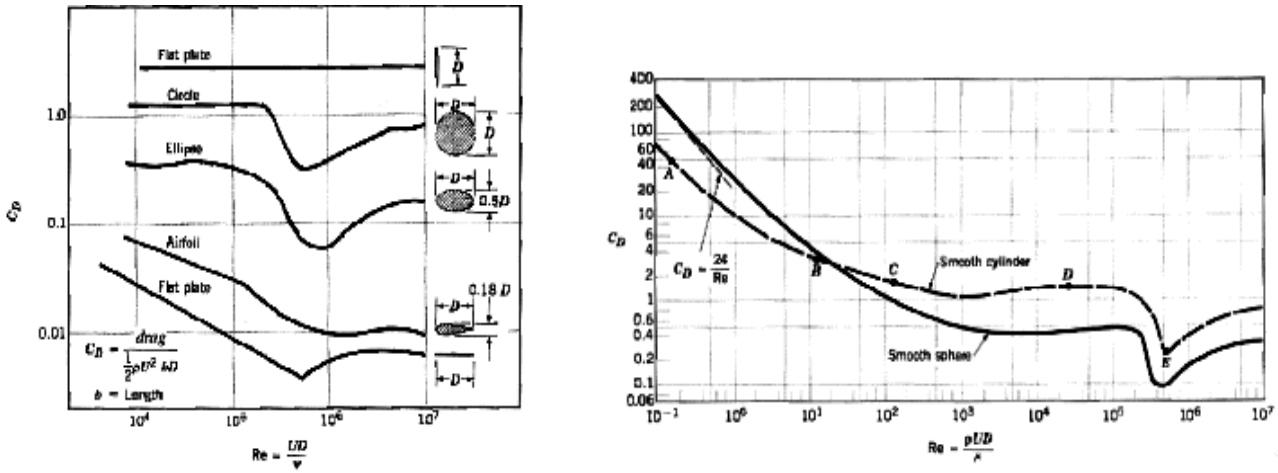

Figure 2.1.4: Drag coefficients of blunt and streamlined bodies and C_D as a function of Reynolds number for smooth circular cylinders and smooth spheres (Munson 2002).

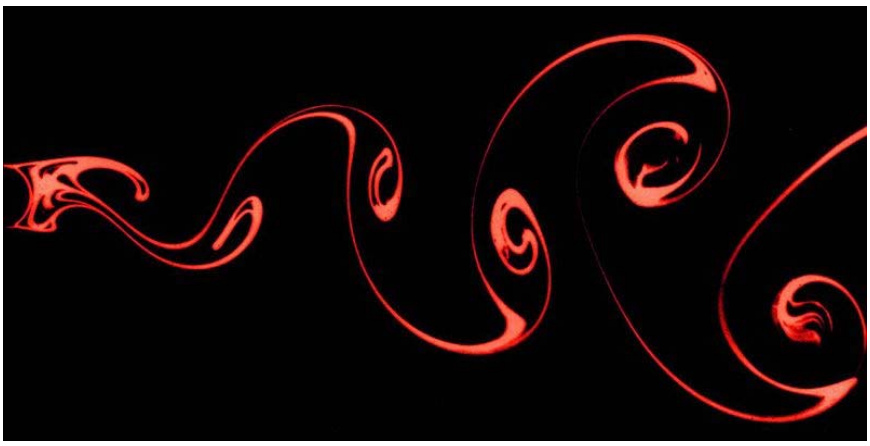

Figure 2.1.5: Von Kármán vortex street behind a circular cylinder. The flow is from the left to the right. Part of the cylinder can be seen at the left edge of the image (Techet 2005).

2.1.3 Flow Regimes

The Reynolds number is a qualitative measure of the importance of viscous forces in the boundary layer compared to inertia forces and is defined as:

$$R_e = \frac{U_\infty L}{v} = \frac{inertia\ forces}{viscous\ forces} \tag{2.1.3}$$

where U_∞ denotes the fluid flow velocity far upstream. For many marine hydrodynamics problems the characteristic lengths and velocities are $L \succeq 1m$ and $U \succeq 1\frac{m}{s}$ respectively. The kinematic viscosity in water is v_{water} $=10^{-6}\frac{m^2}{s}$ leading thus to typical Reynolds numbers with respect to U_∞ and L in the order of 10^6.

The flow past a circular cylinder is associated with various instabilities. These instabilities involve the wake, separated shear layer and boundary layer. Williamson [9] has given a comprehensive description of the flow phenomena at different R_e numbers. Up to $R_e = 47$, the flow is steady with two symmetric vortices on each side of the wake center line. The first wake instability, manifestation of a Hopf bifurcation (Williamson [9], Strogatz [10]), occurs at $R_e = 47$. For $R_e \succ 47$, although it remains laminar, the flow becomes unsteady and asymmetric. Von Kármán vortex shedding is observed for slightly larger R_e. At $R_e = 190$, three-dimensional instabilities, such as formation of vortex loops, deformation of primary vortices and streamwise/spanwise vortices appear in wake. The wake undergoes a series of complex three-dimensional instabilities and, eventually, becomes turbulent. The study of Karniadakis & Triantafyllou [11] suggested that the wake becomes three dimensional as a result of a secondary instability of the 2-D vortex street, which is confirmed by Barkley & Henderson [12]. Karniadakis & Triantafyllou state that, as R_e is increased, the wake velocity fluctuations indicate a cascade of period-doubling bifurcations, which create a chaotic state in the flow at around $R_e = 500$.

Beyond a certain critical R_e, the shear layers separating from the upper and lower surface of the cylinder, start becoming unstable via the Kelvin-Helmholtz mode of instability (Williamson [9]). The transition point, beyond which the separated layer becomes unstable, moves upstream with increase in R_e. At $R_e \sim 2{\times}10^5$, the boundary layer on the cylinder surface undergoes a transition from laminar to turbulent. This transition leads to a displacement of the boundary layer separation point on the aft part of the cylinder surface, causing a substantial reduction in the drag force that the cylinder experiences. The prescribed phenomenon is often referred to as drag crisis.

A crude division of the flow regimes is given by Blevins [3] (also see Fig2.1.6):

- $300 \prec R_e \prec 1.5 \times 10^5$, Subcritical regime
- $1.5 \times 10^5 \prec R_e \prec 3.5 \times 10^5$,Transitional regime
- $R_e \succ 3.5 \times 10^5$, Supercritical regime

2.1.4 Vortex Shedding Frequency

The frequency at which vortex shedding takes place for a cylinder can be derived using the following equation (Eq.2.1.4), defining the Strouhal number. Vincenc Strouhal was the first to discover that for varying current velocity U_∞,

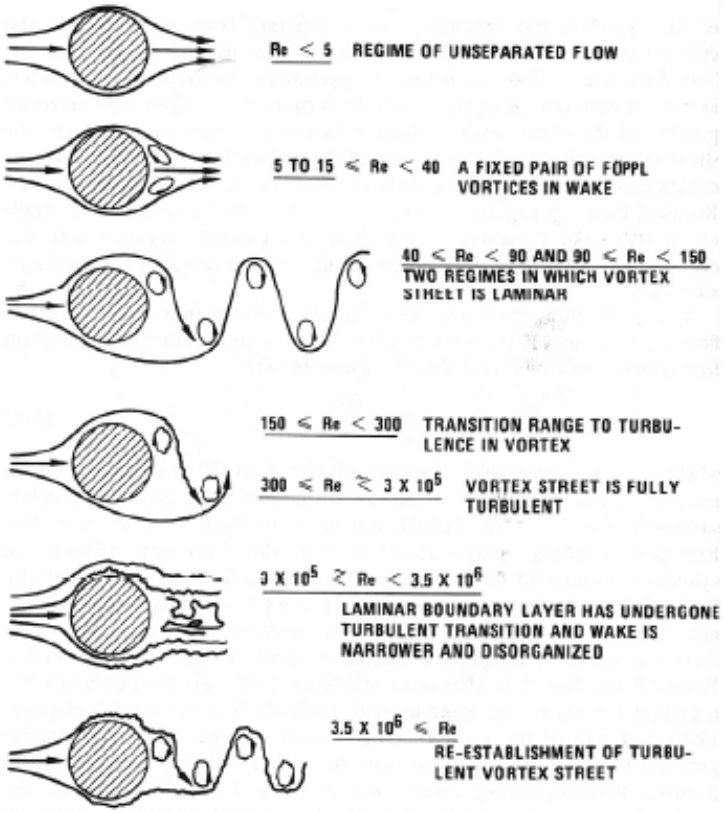

Figure 2.1.6: Regimes of fluid flow across smooth circular cylinders.(Wiggins, 2005)

the vortex shedding frequency behind a stationary cylinder f_{st} is proportional to $\frac{U_\infty}{D}$. The Strouhal number depends on the body shape and on the R_e number (see Fig.2.1.7).

$$S_t = \frac{f_{st} D}{U_\infty} \tag{2.1.4}$$

As show in Fig.2.1.7, the Strouhal number remains nearly equal to 0.2 for $300 \leq R_e \leq 100.000$. Hence, in this range of Reynolds numbers, the vortices are shed from a cylinder at a frequency directly proportional to $0.2\frac{U_\infty}{D}$.

2.2 Vortex Induced Vibrations

2.2.1 Bluff Bodies

An all inclusive definition of a self-exciting "bluff body" does not exist. According to Sarpkaya [5] "a bluff body can be described only in general terms by relying on the readers' "imagination"". Trying to give an implicit definition one can claim that it is an elastic or elastically mounted fore-and-aft body of proper mass, material damping, and shape whose cross-section facing the ambient flow at high-enough Reynolds numbers gives rise to separated flow and hence to two shear layers, which interact with each other and bound an unsteady wake. A more generic approach is to refer to the so called "VIV-Body", a term used to describe a body capable of giving rise to VIV.

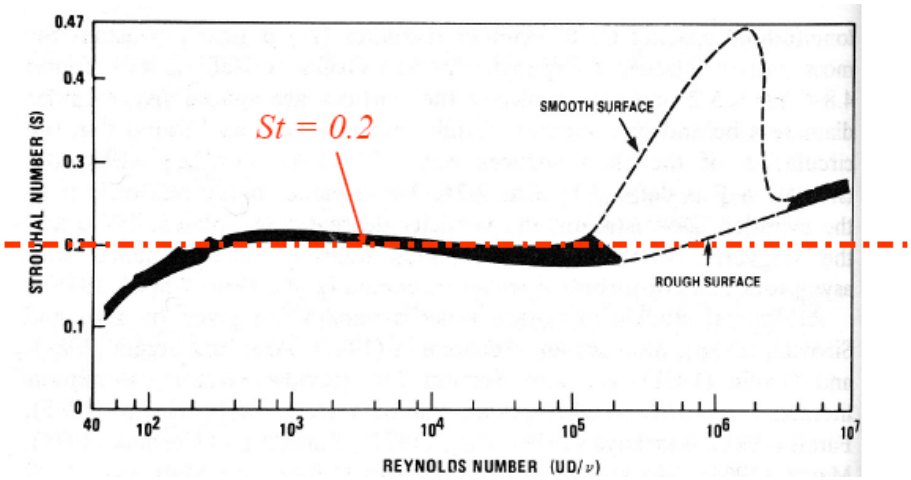

Figure 2.1.7: The Strouhal number as a function of the Reynolds number for a stationary circular cylinder. (Lienhard 1966; Rosko 1955;Techet 2005)

As stated by Sarpkaya [5], a VIV-body (e.g., a circular- or square-section cylinder) may be excited by the vortices it sheds if it is mounted on springs and exposed to a steady uniform flow. When the prevailing vortex shedding frequency f_{vs} (not always close to f_{st}) and the excitation frequency f_{ex} of the body approach a common frequency f_{com}, the body begins to experience relatively small vortex induced oscillations. These are controlled by the spring constant, body mass, structural damping, the density and the motion of the fluid surrounding the body, plus a number of difficult-to-quantify influencing parameters.

2.2.2 Oscillating Lift Force

The shedding of vortices generates time varying pressure over the cylinder. Integrated over the cylinder surface this can give rise to time varying forces both in-line with the flow and transverse to the flow. The frequency of the oscillating force transverse in the flow direction is given by the vortex shedding frequency, while the oscillating frequency in the in-line direction has a frequency twice the vortex shedding frequency.

The time varying transverse force F_y is referred to as the lift force. The lift coefficient C_L is defined as:

$$C_L = \frac{F_y}{\frac{1}{2}\rho U_\infty^2 D} \tag{2.2.1}$$

2.2.3 Characteristics of VIV

The origin of the phenomenon is the separated flow, as described in the previous section, where the two shear layers interact with each other and cause an unsteady wake. When the shedding frequency and the natural frequency of the "bluff body" approach a common frequency, the body starts to experience small oscillations (due to dynamic amplification). These small oscillations will help to increase the correlation length of the vortices, which is one of the characteristic properties of VIV. If a cylinder is free to oscillate in both the transverse and in-

line directions, the common frequencies of the body and the driving forces in their respective directions may lead to lock-in and the axis of the body traces the path of figure eight (Moe and Wu, 1990 [13]; Moe et. al., 1994 [14]; Sarpkaya, 1995 [15]). The figure-eight loop is caused by the considerable variation of drag force during large amplitude oscillation. For a fixed cylinder the vortex shedding process is correlated only a few diameters along the length of the cylinder, typically 3-6 diameters for the subcritical flow regime (see Blevins [3]). Hence, the force acting on the cylinder has different phase over the length of the cylinder and the resulting force is small. When the correlation increases, the resulting force on the cylinder increases and the oscillation amplitude will also increase. When the oscillation amplitude in the cross flow direction reaches approximately $0.1D$ (or $0.02D$ in the in-line direction), increased vortex strength is seen (Sarpkaya [5]). This will further contribute to increasing the oscillation amplitude. If the flow velocity and thus the oscillation amplitude is further increased, the spacing between the shear layers defining the virtual body increases. This apparent increase in D is compensated by the increased flow velocity, thus keeping the shedding frequency nearly constant (see Eqn.2.1.4). This represents a change from the linear increase in shedding frequency for increasing flow velocity, i.e. the shedding frequency is lower than predicted by the Strouhal relation. This represents the start of the self-excitation region, or more commonly known as the lock-in region. The vortex shedding frequency matches the oscillation frequency of the body at a frequency apparently dominated by the still water natural frequency of body. However, the frequency is changed somewhat due to a change in virtual mass (i.e. added mass or hydrodynamic mass) caused by the vortex shedding process. The effect of the change in hydrodynamic mass is influenced by the mass ratio of the body. The oscillation frequency is more influenced by this change in for low mass ratio bodies than for heavier bodies. For increasing flow velocity the oscillation amplitude will increase until some maximum value is reached. This value is typically $1.0D$ for purely transverse oscillations at subcritical flow conditions and $Re \prec 15.000$, $1.2D$ for $Re \succ 15.000$, and up to $1.5D$ (see Jauvtis and Williamson [8]) for a body free to oscillate both in-line with and transverse to the flow. As the oscillation frequency to a large degree is controlled by the natural frequency of the body and the oscillation amplitudes reach a maximum value, VIV is considered a self-limiting resonance phenomenon.

Regarding vortex shedding modes in the wake of a circular cylinder, Williamson and Roshko ([16], 1988) described, in the range $300 \prec R_e \prec 1000$, the emergence of various regimes (see Fig.2.2.1) in a map (often referred to as the "Williamson-Roshko" map) of $\frac{A}{D}$ versus $\frac{f_{st}}{f_{ex}}$ (as well as $\frac{\lambda}{D} = \frac{U_\infty}{f_{ex}D}$), where λ is the wavelength. This map is based on experiments in which the cylinder was forced to oscillate transversely to a steady flow.

2.3 Methods for Investigation of VIV

A detailed listing of the methods applied for investigating VIV is beyond the purpose of the present work. Sarpkaya [5], Bearman [17] and Williamson and Govardhan [18] provide an integrated approach on the intrinsic nature of VIV, reviewing the research carried out during the past few decades. However, preserving consistency, this section summarizes the basic experimental and computational

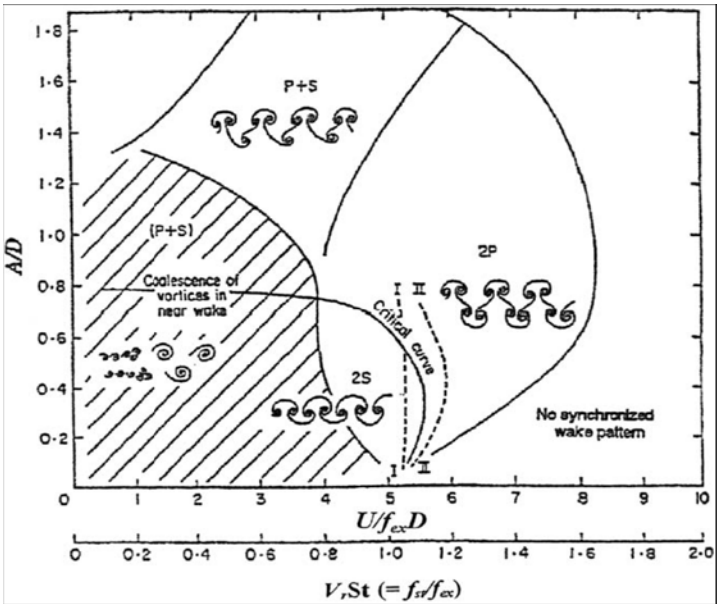

Figure 2.2.1: Map of vortex patterns of a vertical cylinder forced to move along a sinusoidal path in the Re range of $300 \prec R_e \prec 1000$. The critical curve marks the transition from one mode of vortex shedding to another (Williamson and Roshko[16], 1988).

approaches for the investigation and prediction of VIV.

2.3.1 Free Vibration Experiments

A large number of free vibration or self-excitation VIV experiments have been carried out since the pioneers started in the 1960s. Sarpkaya [5] gives references to the publications on the topic. In the discussion given therein the free vibration experiments have been divided into two groups based on how the eigenfrequency of the system is generated. These are:

- Rigid cylinder tests, in which the test cylinder is supported by springs in the oscillation direction, and the eigenfrequency is controlled by the spring stiffness and mass of the oscillating parts.
- Flexible beam tests where the eigenfrequencies are controlled by the mass, bending stiffness, axial tension and length of the beam. In the first group, oscillations can be restrained in either cross-flow or in-line direction, or the cylinder may be free to oscillate in both degrees of freedom.

The second type of free vibration experiments (flexible beam tests) is often performed as scaled models of real slender marine structures. The eigenfrequencies of these structures are associated with eigenmodes or modeshapes. Hence, when the structure oscillates the oscillation amplitude varies over the length of the structure. Stationary response for experiments with uniform flow along the beam is reached when there is a balance between excitation from forces in zones with low and moderate oscillation amplitudes, damping in zones with high oscillation amplitudes and structural damping. Maximum response amplitudes seen for flexible beams are expected to be higher than seen for rigid cylinder experiments.

2.3.2 Forced Oscillations Experiments

In a forced oscillation experiment the test cylinder is given a prescribed motion. The wake behind the cylinder responds to this motion, and the force from the wake acting on the cylinder can be measured. If this method should give relevant data for real VIV, the prescribed motions must be identical to the response in free vibrations. Free vibration experiments of short rigid cylinders indicate that the response is harmonic. Hence, forced oscillation experiments have been performed using prescribed harmonic motions. The result from a forced oscillation experiment is knowledge of the hydrodynamic force acting on the cylinder under the tested conditions.

Forced oscillation experiments can be performed both in a towing tank and in a water tunnel. A motion generation system is required, in order to generate the desired oscillations, in addition to force sensors. It is important that the apparatus has a high stiffness so that structural eigenfrequencies in the apparatus do not interact with the oscillation frequencies. Measuring the correct phase between the force and the motion is essential in this type of experiment. Hence, motion sensors, in addition to those used by the control system, are mandatory. A data acquisition system capable of recording data at all channels simultaneously, or with a known delay, is also required.

2.3.3 Numerical Simulations

The numerical simulation of flow past a circular cylinder undergoing VIV at relatively small Reynolds numbers (particularly in the range R_e = 100-1,000) is complicated by some of the most difficult problems of fluid mechanics such as separation excursions, incomplete transition in the shear layers, and the coherence length based on a yet unexplained coupling mechanism between the dynamics of the near-wake and that of the structure. Most of the disparity between the experiments and numerical simulations is attributable to the fact the mean position of the line of transition to turbulence does not reach upstream enough for Re less than about 15,000 to 20,000, even though VIV with two degrees of freedom (2-DOF) may precipitate the instability somewhat sooner. At present, none of the methods available ensures sufficient generality in a large parameter space as far as VIV is concerned.

The approach to the bluff body wake problem from direct numerical simulations (DNS) has received a great deal of attention recently. Not only are the mean parameters such as the Strouhal number, drag force and stresses in the wake well predicted, but the simulations provide a tool to understand the physics of the flow, as has been indicated by numerous examples of studies. The agreement among the computations and with the experiments is now remarkably good.

Many models of turbulence, for every occasion, are described in numerous papers. However, DNS does not require 'modeling'. It deals only and purely with the numerical problem of solving the time-dependent Navier–Stokes equations, albeit at relatively small Reynolds numbers. Large eddy simulations (LESs) appeared to be a compromise. As Grinstein and Karniadakis [19] noted: "After more than 30 years of intense research on LESs of turbulent flows based on eddy-viscosity subfilter models, there is now consensus that such an approach is subject to fundamental limitations. It has been demonstrated for a number of different flows that the shear stress and strain tensors involved in subfilter eddy-viscosity models have

different topological features rendering scalar eddy-viscosity models inaccurate.". Other computational methods include the discrete-vortex method (DVM), the use of Reynolds Averaged Navier-Stokes (RANS) simulations, or the combination of a number of them.

2.3.4 Models for Prediction of VIV

The complexity of VIV phenomena introduce considerable uncertainties when dealing with cases of industrial use. The most sufficient way to overcome these real life uncertainties is to incorporate integrated models and empirical formulations (such as strip theory) for the excitation and the response prediction of engineering structures. Parametric response models the most used models for predicting response due to VIV, especially for free spanning pipelines. This method utilizes data obtained from free vibration experiments in order to estimate, based on tabulated data and mathematical formulations, response characteristics such as oscillation amplitudes and frequencies. However, the imposed high safety factors lead to rather conservative modeling and design approaches. One other method is the empirical force coefficient method (this method is used in the computer program VIVANA) , which is primarily used for estimating VIV of marine risers. The fundamental difference from the parametric response model method is that here the hydrodynamic forces caused by the vortex shedding process are modeled and the response is estimated by applying the forces on a finite element model. The main limitation of the method is that it is valid only for pure cross-flow VIV.

Chapter 3

Formulation and Numerical Method

In the present work we investigate the forces acting on a cylinder subject to both transverse (y-direction) and in-line (x-direction) excitation to a uniform stream. The cylinder is tracing a "figure 8" path in the two-dimensional space, emulating the motion of real cylindrical structures undergoing vortex-induced vibrations. The frequency of the in-line oscillation is considered to be equal with the resonant vortex shedding frequency of the cylinder f_{st}, while the frequency of the transverse oscillation equals half this frequency (subharmonic forcing). The Reynolds number is held constant to a value of 400, falling into the regime where shear layer instabilities introduce a three dimensional flow character. This three dimensional behavior over a two dimensional setup enhances the complexity of the phenomena and leads to a time-dependent wake that illustrates very rich dynamics.

3.1 Formulation

3.1.1 Dimensional Analysis

Dimensional analysis is a conceptual mathematical tool often applied in science and engineering, to understand physical situations involving a mix of different kinds of physical quantities. It is routinely used to check the plausibility of derived equations and computations. It is also used to form reasonable hypotheses about complex physical situations that can be tested by experiment or by more developed theories of the phenomena.

In the present work, a set of non-dimensional control parameters is used in order to establish a consistent framework of notation so that the results obtained can be easily compared to outcomes of previous studies. Therefore, we introduce the following non-dimensional parameters:

- The Reynolds number (see Section 2.1.3): $R_e = \dfrac{U_\infty L}{v}$.
- The non-dimensional excitation amplitude-over-diameter ratio $\xi = \dfrac{A}{D}$ (reduced amplitude), where A is the excitation amplitude and D the cylinder diameter. In each case, we distinguish between the in-line and transverse

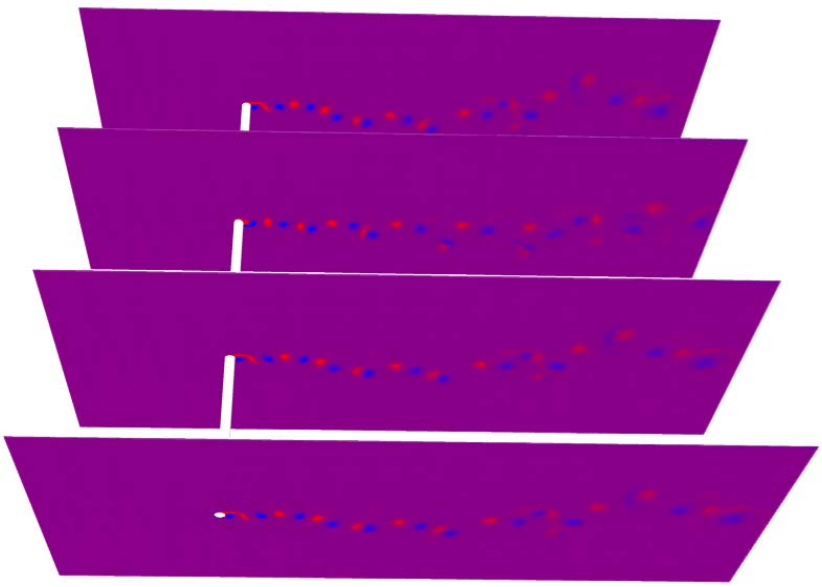

Figure 3.1.1: Resulting three dimensional dynamical behaviour from a two dimensional problem setup.

oscillation directions by using the ratios $\frac{A_y}{D}$ and $\frac{A_x}{D}$, where A_y is the excitation amplitude in the transverse to the flow direction (y-direction), while A_x is the excitation amplitude corresponding to in-line oscillation (x-direction).

- The reduced oscillation frequency $F = \frac{f_{ex}}{f_{st}}$, where f_{ex} is the excitation frequency and $f_{st} \equiv S_t$, the Strouhal number (see Sec.2.1.4). Note that decreasing the reduced frequency F corresponds to increasing the wavelength parameter λ/D of the Williamson-Roshko map (see Fig.2.2.1).
- The excitation amplitudes ratio $\epsilon = \frac{A_x}{A_y}$.

Dimensional analysis shows that we can express the system dynamics as a function of the following parameters:

$$Dynamics = f(R_e, \frac{A_y}{D}, F, \frac{A_x}{A_y}, direction\ in\ which\ the\ cylinder\ is\ traversed) \tag{3.1.1}$$

3.1.2 Problem Setup

A smooth circular cylinder is forced to oscillate both transversely and in-line to a uniform stream. Spatial description of the flow and the cylinder motion is derived from a Cartesian coordinate system formed by the x-axis (parallel to the incoming flow) and the y-axis (normal to the incoming flow). The velocity of the fluid far upstream is U_∞, the density of the fluid is ρ and the kinematic viscosity v. The cylinder has diameter D and is oscillating transversely and in-line with amplitudes A_y and A_x, respectively. The excitation frequency frequency

is denoted by f_{ex}, and is defined as the oscillation frequency in the transverse direction. The in-line frequency is equal to twice the transverse frequency. In the present work, f_{ex} is equal to half the vortex shedding frequency f_{st} of a flow past a stationary cylinder, i.e corresponds to sub-harmonic forcing. The corresponding circular frequency is denoted by $\omega = 2\pi f$. The cylinder is traversing the fluid domain tracing a "figure-8" path with instantaneous displacement from the mean position described by:

$$\begin{aligned} \eta_x &= \pm A_x \sin(4\pi f_{ex} t) \\ \eta_y &= A_y \sin(2\pi f_{ex} t) \end{aligned} \tag{3.1.2}$$

where the $\pm$ sign of η_x indicates whether the cylinder is being traversed in a "clockwise" ($-$ sign) or "counter-clockwise" ($+$ sign) direction (in the upper x-y plane).

3.2 Force decomposition

3.2.1 Lift Force

Integrating the pressure and the viscous stresses around the cylinder we obtain the total fluid force acting on the cylinder. Analyzing this force into its two components we take F_x and F_y as the drag and the lift force respectively (per cylinder unit length). For a locked-in wake (see Sec.2.1.4), F_y is a harmonic function of time with frequency equal to f_{ex} and thus can be decomposed into the excitation force and the inertia or added mass components:

$$F_y = F_v \cos(2\pi f_{ex} t) + F_M \sin(2\pi f_{ex} t) \tag{3.2.1}$$

where F_v and F_M are the amplitudes of the excitation and added mass forces, respectively. We must note that according to this decomposition, F_v is a force in phase with the cylinder's velocity while the added mass force F_M is 180^o degrees out of phase with the cylinder's acceleration.

Following the assumption that F_y is a harmonic function of time, we can calculate its corresponding components, F_v and F_M using the relation:

$$F_v + iF_M = \frac{2}{T}\int_0^T F_y e^{i\omega t} dt \tag{3.2.2}$$

where $i = \sqrt{-1}$, $T = \dfrac{2\pi}{\omega}$ the period of the cylinder's oscillation and $\omega = 2\pi f_{ex}$ the oscillation's circular frequency.

Introducing the non-dimensional parameters C_{L_v} and C_M we can scale F_v and F_M as follows:

$$F_v = \frac{1}{2}\rho U_\infty^2 D C_{L_v} \tag{3.2.3}$$

$$F_M = \frac{\pi}{4}\rho D^2 A_y \omega^2 C_M \tag{3.2.4}$$

Interpreting this scaling, F_v is a force proportional to the dynamic pressure $\dfrac{1}{2}\rho U_\infty^2$ while F_M is proportional to the cylinder's acceleration. However, a consistency issue arises and we should be cautious with this scaling since F_v and F_M are

components of the same force (F_y). Thus, we will consider scaling F_M with the dynamic pressure as well :

$$F_M = \frac{1}{2}\rho U_\infty^2 D C_{L_a} \tag{3.2.5}$$

where C_{L_a} is a new non-dimensional parameter.

Using the definitions presented above in combination with Eq.3.2.4 and Eq.3.2.5, it is straightforward to show the relation between C_M and C_{L_a}:

$$C_{L_a} = 2\pi^3 (\frac{A}{D})(\frac{D}{U_\infty T})^2 C_M \tag{3.2.6}$$

Moreover, utilizing Eq.3.2.2, we can calculate C_{L_v}, C_{L_a} and C_M as follows:

$$C_{L_v} = \frac{2}{T}\int_0^T C_L \cos(\omega t) dt \tag{3.2.7}$$

$$C_{L_a} = \frac{2}{T}\int_0^T C_L \sin(\omega t) dt \tag{3.2.8}$$

$$C_M = \frac{2}{T}\int_0^T \frac{1}{2\pi^3} C_L \sin(\omega t) \frac{1}{(\frac{A}{D})} \frac{1}{(\frac{D}{U_\infty T})^2} dt \tag{3.2.9}$$

Having scaled both F_v and F_M with the dynamic pressure, is reasonable to scale the same way the lift force F_y:

$$F_y = \frac{1}{2}\rho U_\infty^2 D C_L \tag{3.2.10}$$

where C_L is the non-dimensional lift coefficient. This last term is a function of time and can also be decomposed into the time averaged value $\langle C_L \rangle$ and its instantaneous fluctuations C_L'. Consequently, we can characterize the fluctuations of the lift force by calculating the root mean square (r.m.s) value of C_L', denoted here by $C_{L,rms}$. Specifically, when the force on the cylinder is harmonic in time (lock-in region) the value of $C_{L,rms}$ is:

$$C_{L,rms} = \frac{1}{\sqrt{2}}\sqrt{C_{L_v}^2 + C_{L_a}^2} \tag{3.2.11}$$

However, in the present study, in order to quantify the r.m.s values of the hydrodynamic forces, we use the following definition for the r.m.s values of a signal's fluctuations:

$$C_{L,rms} = \sqrt{\overline{[(C_L - \langle C_L \rangle)^2]}} \tag{3.2.12}$$

, where the over-line signify mean value.

Notice that dimensional analysis assures that C_{L_v}, C_{L_a}, C_M and C_L are all functions of the reduced amplitude $\xi = \frac{A_y}{D}$, the non-dimensional excitation frequency $f_{ex} = \frac{\omega D}{2\pi U_\infty}$ and the Reynolds number.

3.2.2 Drag Force

Additionally, the incoming fluid flow generates a force parallel to the stream (drag force) on the cylinder. Let F_x denote this drag force (per cylinder unit length). As above, we can define the drag force coefficient C_D:

$$F_x = \frac{1}{2}\rho U_\infty^2 D C_D \tag{3.2.13}$$

Following the methodology presented above, we can decompose the drag force into its excitation and inertia components. The resulting normalized coefficients are denoted by C_{D_v}(excitation force coefficient), C_{M_x}(inertia force coefficient scaled with the cylinder acceleration) and C_{D_a}(inertia force coefficient scaled with the dynamic pressure).

Similarly, the drag coefficient can be decomposed into its time averaged component $\langle C_D \rangle$ and its fluctuating component C'_D:

$$C_D = \langle C_D \rangle + C'_D \tag{3.2.14}$$

where the time-averaged component $\langle C_D \rangle$ is calculated by:

$$\langle C_D \rangle = \frac{1}{T}\int_0^T C_D dt \tag{3.2.15}$$

Finally, the root mean square value of C_D will be denoted by $C_{D,rms}$.

3.2.3 Power Transfer

Here, we consider the power transfer, i.e. the energy per cylinder unit length, between the flow and the cylinder. By definition, the power transfer is given by:

$$P(t) = F_{hydro}(t) \cdot \frac{d}{dt}\vec{\eta}(t) \tag{3.2.16}$$

where $\eta(t)$ is the instantaneous displacement of the cylinder from its mean position, hence its time derivative describes the instantaneous cylinder velocity.

In the presence of both in-line and transverse cylinder oscillation, the total power transfer parameter, P, consists as the sum of the corresponding contributions:

$$P = P_x + P_y \tag{3.2.17}$$

where P_x and P_y denote the power transfer in the in-line and the transverse direction respectively. In general, these two components can be calculated by taking their time averaged values:

$$P = \lim_{T\to\infty}\frac{1}{T}\int_t^{t+T}[F_x(t)\cdot\frac{d}{dt}\eta_x(t) + F_y(t)\cdot\frac{d}{dt}\eta_y(t)]dt \tag{3.2.18}$$

Finally, the computed time-averaged power transfer can be normalized by $\frac{1}{2}\rho U_\infty^3 D$ to yield the non-dimensional "power transfer parameter".

3.3 Mathematical Modeling

3.3.1 Governing Equations

The governing equations are the two-dimensional Navier-Stokes equations and the incompressibility equations. All lenghts have been non-dimensionalized with respect to the cylinder's diameter D, all velocities with respect to the free stream velocity U_∞, time with respect to $\frac{D}{U_\infty}$ and pressure with respect to ρU_∞^2.Therefore the system of partial differential equations that describe the flow in our fluid domain is comprised by:

$$\nabla \cdot \overrightarrow{u} = 0 \tag{3.3.1}$$

$$\frac{\partial \overrightarrow{u}}{\partial t} + \overrightarrow{u} \cdot \nabla \overrightarrow{u} = -\nabla p + \frac{1}{R_e} \nabla^2 \overrightarrow{u} \tag{3.3.2}$$

where R_e is the Reynolds number of the flow.

3.3.2 Boundary Conditions

In order to obtain a solution from the above system of equations, the appropriate boundary conditions must be introduced. Thus we have the following (also see Fig.3.3.1):

- On the instantaneous position of the cylinder the velocity of the fluid is equal to that of the cylinder:

$$\overrightarrow{u} = \frac{d\eta_x}{dt} \overrightarrow{i} + \frac{d\eta_y}{dt} \overrightarrow{j} \tag{3.3.3}$$

  where η is the instantaneous displacement of the cylinder from its mean position, and $\overrightarrow{i}$ and $\overrightarrow{j}$ is the corresponding unit vectors.

- Far upstream and at the sides of the fluid domain we assume uniform flow (the dimensional velocity is equal to U_∞) :

$$\overrightarrow{u} = U_\infty = 1 \overrightarrow{i} \tag{3.3.4}$$

  where $\overrightarrow{i}$ is the unit vector in the x-direction.

- Far downstream a Neuman-type condition for the velocity is imposed:

$$\frac{\partial \overrightarrow{u}}{\partial n} \approx 0 \tag{3.3.5}$$

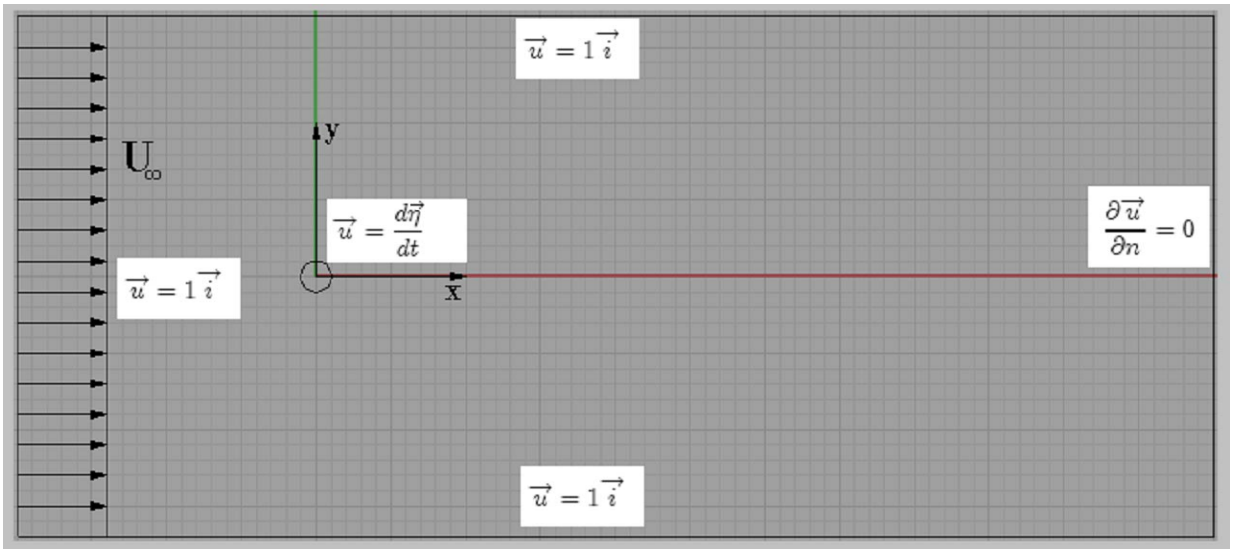

Figure 3.3.1: Boundary conditions sketch.

3.4 Numerical Method

3.4.1 Spectral Element Methods

Traditional boundary and finite element methods employ low-order polynomial expansions that rely on mesh refinement to achieve high accuracy. In contrast, spectral element methods employ high-order expansions with spectral accuracy with large element size.

The spectral element method is an elegant formulation of the finite element method with a high degree piecewise polynomial basis. The method is capable to numerically solve certain partial differential equation (PDE) configurations, demonstrating high efficiency especially on elliptic boundary value problems. Where applicable, spectral element methods have excellent error properties, with the so called "exponential convergence" being the fastest possible.

Introduced in a 1984 paper by A. T. Patera [20], the abstract begins: "A spectral element method that combines the generality of the finite element method with the accuracy of spectral techniques...". Generally speaking, the spectral element method is a high-order finite element technique that combines the geometric flexibility of finite elements with the high accuracy of spectral methods. This method was pioneered in the mid 1980's by Anthony Patera at MIT and Yvon Maday at Pierre and Marie Curie University (Paris, France). It exhibits several favorable computational properties, such as the use of tensor products, naturally diagonal mass matrices and adequacy to implementations in a parallel computer system. Due to these advantages, the spectral element method is a viable alternative to currently popular methods such as finite volumes and finite elements, if accurate solutions of regular problems are sought.

The spectral element method expands the solution in high degree piecewise polynomial basis functions, therefore a chief advantage is that the resulting method is of very high order and, in other words, is achieving a very high order of accuracy. The main technical features of this method are the following:

- *Lagrange interpolants shape functions*: The method is implemented by using

tensor-product Lagrange interpolants within each element, where the nodes of these shape functions are placed at the zeros of Legendre polynomials (Gauss-Lobatto points). For smooth functions it can be shown that the resulting interpolants converge exponentially fast as the order of the interpolant is increased.

- *Gauss-Lobatto quadrature*: Efficiency is achieved by using Gauss-Lobatto quadrature for evaluating elemental integrals. The quadrature points reside at the nodal points, which enables fast tensor-product techniques to be used for iterative matrix solution methods. Gauss-Lobatto quadrature results naturally in diagonal mass matrices.

A main issue in the implementation of the spectral element methodology is the identification of a complete set of proper element nodes that allows for uniform and fast convergence of the nodal expansion.

Further details and foundations of this method can be found in the books of Karniadakis & Sherwin [21] and Pozrikidis [22], [23].

3.4.2 Computational Setup

The model we implement in this study uses a moving-grid technique to solve the Navier-Stokes equations expressed in the arbitrary Lagrangian-Eulerian kinematics. The discretization in space is based on the spectral element method. The coupling of the fluid equations and the moving-grid equations is essentially done through the conditions on the moving boundaries.

Utilizing this moving-grid technique implies that we must modify accordingly the corresponding equations and boundary conditions. Therefore, while the incompressibility equation (Eq.3.3.1) remains unchanged, the Navier-Stokes equations (Eq.3.3.2) become:

$$\frac{\partial \overrightarrow{u}}{\partial t} + \overrightarrow{u} \cdot \nabla \overrightarrow{u} = -\nabla p + \frac{1}{R_e} \nabla^2 \overrightarrow{u} - \frac{d^2 \eta_x}{dt^2} \overrightarrow{i} - \frac{d^2 \eta_y}{dt^2} \overrightarrow{j} \tag{3.4.1}$$

where we have the appearance of a D'Alambert acceleration term at the right-hand side (by η we denote the instantaneous cylinder displacement from the mean position). Hence, in order to calculate the actual total force acting on the cylinder's surface, we have to subtract from the computed force a "dynamic Archimedes" force equal to $-\frac{\pi}{4}\rho D^2(\frac{d^2\eta_x}{dt^2}\overrightarrow{i} + \frac{d^2\eta_y}{dt^2}\overrightarrow{j})$.

Moreover, the boundary conditions are modified as follows:

- On the cylinder's surface the velocity is reduced to:

$$\overrightarrow{u} = 0 \tag{3.4.2}$$

- At the inflow and the lateral boundaries:

$$\overrightarrow{u} = (U_\infty - \frac{d\eta_x}{dt}\overrightarrow{i}) - \frac{d\eta_y}{dt}\overrightarrow{j} \tag{3.4.3}$$

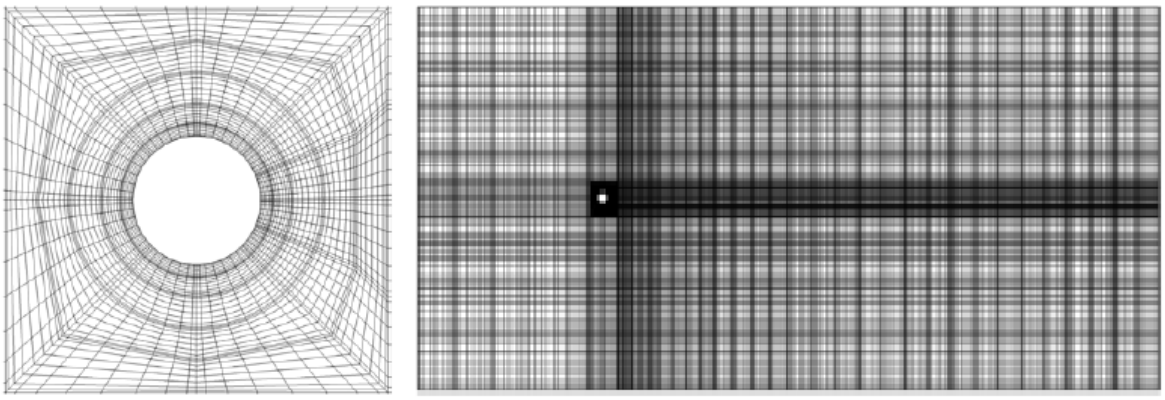

Figure 3.4.1: Spectral element computational grid and grid details close to the cylinder.

- The Newmman condition is maintained at the ouflow boundary (y-direction velocity component equals to zero):

$$\frac{\partial \overrightarrow{u}}{\partial n} = 0 \tag{3.4.4}$$

The above PDE boundary value problem comprising of the partial differential equations 3.3.1 and 3.4.1, and the boundary conditions 3.4.2, 3.4.3 and 3.4.4, is solved using a Legendre spectral element method (see Karniadakis [22]), with the time discretization based on a second order accurate mixed stiffly stable scheme (Karniadakis et. al. [23]). The same numerical methodology has been successfully implemented in numerous previous studies (Kaiktsis et. al. [1]; Delaunay and Kaiktsis [26]; Kaiktsis and Monkewitz [27]).

The spectral element computational grid used is demonstrated in Fig.3.4.1, with the inflow boundary located at $\frac{x}{D} = -20$, the lateral boundaries at $\frac{y}{D} = \pm 17$, while the outflow boundary is at $\frac{x}{D} = 60$. The discretization consists of 464 macro-elements, with 9×9 elemental resolution. The values of the chosen numerical time step were of the order of 0.0015. Experience from previous numerical studies (Evangelinos and Karniadakis [28]; Blackburn and Henderson [29]) offers valuable guidance in selecting the domain size and resolution parameters. Resolution tests, illustrating the adequacy and efficacy of the present discretization, can be found from Kaiktsis et. al. [1].

Chapter 4

Results

In this chapter we present detailed results of our two dimensional simulations. We have considered five different cases in which we vary the amplitude ratio ϵ for a number of reduced oscillation amplitudes ξ (see Table.4.0.1). As described in Chapter 3, we adopt a direct numerical simulation (DNS) approach by using a spectral element scheme that solves the corresponding 2-dimensional Navier-Stokes equations on a coordinate system fixed on the cylinder. When steady-state behavior is reached, lift and drag forces are computed. Finally, through force decomposition analysis and flow visualization we are able to quantify the impact of our non dimensional control parameters and reach a conclusion about whether this problem setup can lead to self excited vortex induced vibrations of the cylinder.

Table 4.0.1 summarizes the parameter values used in our simulations:

R_e	$\xi = \frac{A_y}{D}$	F	$\epsilon = \frac{A_x}{A_y}$	*x-y plane oscillation direction*
400	$0.0 \div 0.30$	0.5	$0, 0.2, 0.4, 0.6, \infty$	"*clockwise*" *or* "*counter-clockwise*"

(4.0.1)

Parameter values used in our simulations.

Simulations for a stationary cylinder in a uniform flow were performed to determine the drag coefficient and the Strouhal number. The values obtained are $f_{st} = 0.22017$ for the Strouhal frequency and $C_D = 1.4169$ for the time-averaged drag coefficient.

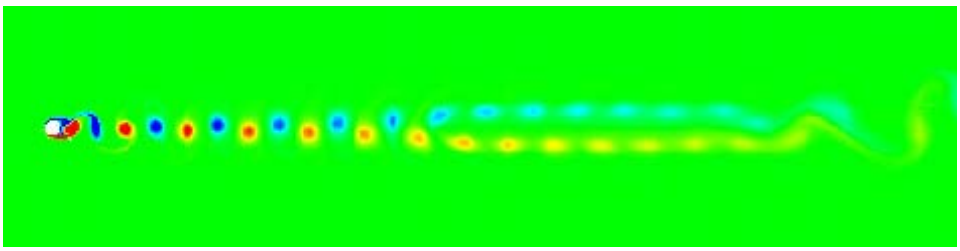

Figure 4.0.1: Instantaneous vorticity iso-contours illustrating the formation of the Kármán vortex street in the wake of a stationary cylinder.

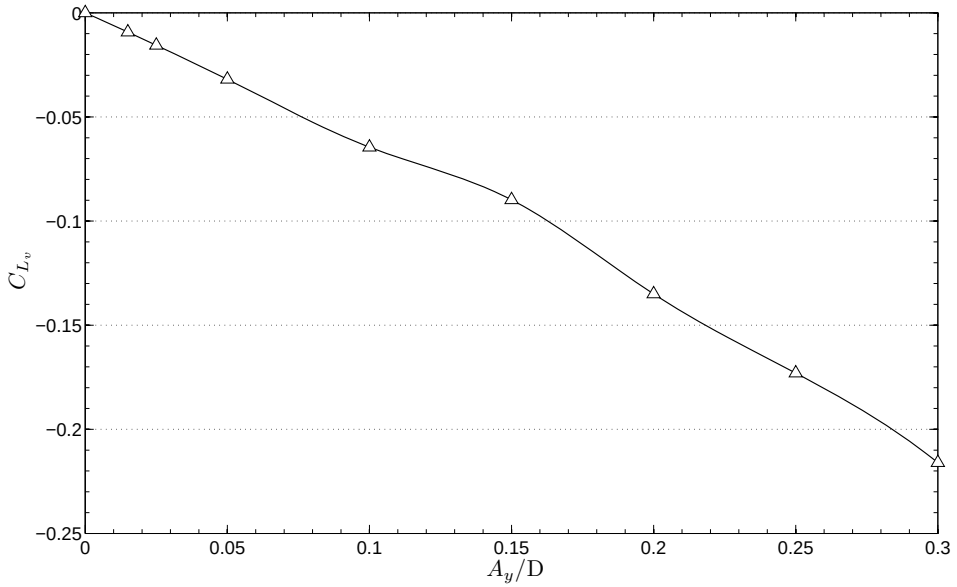

Figure 4.1.1: Excitation force coefficient C_{L_v} versus nondimensional excitation amplitude, for $\epsilon = 0$.

4.1 Variation of the Hydrodynamic Coefficients

For each combination of $\{\xi, \epsilon\}$ and when the flow has reached a statistical steady state we compute both the lift and drag forces. Then, it is meaningful to decompose the computed forces into their excitation and inertia force components as described in Chapter 3. Following the methodology presented in Chapter 3, the excitation forces are always scaled with the dynamic pressure while for the inertia components we examine scaling not only with the acceleration of the cylinder but with the dynamic pressure as well (see Sec.3.2.1). Finally, we calculate the statistical character of the resulting lift and drag forces as depicted by their mean and fluctuating parts.

4.1.1 One degree of freedom excitation

Our first simulations include two cases of unique interest. In both cases the cylinder is forced to oscillate in only one direction, transversely or in-line. The first case examines a cylinder vibrating transversely to a steady flow at a frequency that equals half the vortex shedding frequency of the stationary cylinder ($\epsilon = 0, F = 0.5$). For the second case we consider a cylinder forced to vibrate in-line to a steady stream at a frequency equal to the natural frequency of vortex shedding ($\varepsilon \rightarrow \infty, F = 1.0$). The variation of the coefficients $C_{L_v}, C_{D_v}, C_M, C_{M_x}, C_{L_a}, C_{D_a}$ and the time-averaged values and fluctuations of C_L and C_D are presented in Figs.4.1.1-12. Note that for the first case the variation of the hydrodynamic coefficients is a function of the reduced amplitude A_y/D, while for the second case the reduced amplitude is A_x/D.

We observe that, in each case, the corresponding excitation force coefficient, C_{L_v} or C_{D_v}, is decreasing smoothly and almost linearly while we increase the reduced oscillation amplitude. Moreover, it takes always negative values, indicating

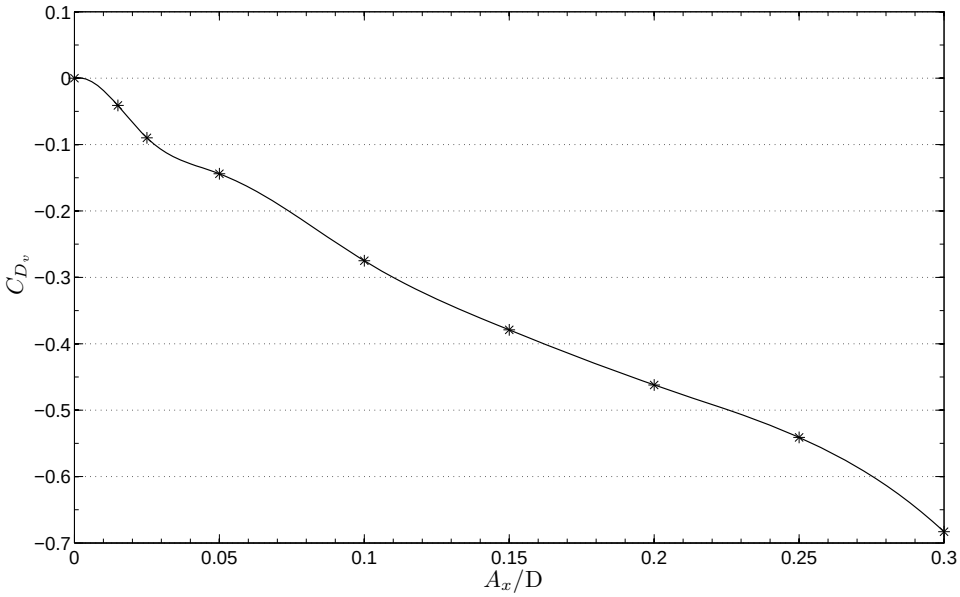

Figure 4.1.2: Excitation force coefficient C_{D_v} versus nondimensional excitation amplitude, for $\epsilon \to \infty$.

that energy flows from the cylinder to the flow and, as of that, the fluid force has damping effects on the structure. Note that for the transverse (y-direction) oscillation case, the excitation force coefficient C_{L_v} takes values between 0 and -0.25 in contrast with C_{D_v} which falls to negative values up to -0.7.

In Figs.4.1.3-4 we can see that the added mass coefficient initially takes negative values for small reduced amplitudes and then increases to reach positive values as we increase ξ. C_M increases continuously and reaches a maximum value close to 0.5 for $A_y/D = 0.30$, while C_{M_x} has a local maximum close to 0.7 for $A_x/D \approx 0.04$ and afterwards decreases slightly for larger reduced amplitudes. Interestingly, we note a divergence as $A/D \to 0$ for both cases of excitation. This kind of behavior was also observed for resonant forcing simulations for the $\epsilon = 0$ case (see Kaiktsis et. al. [1]). This results suggests, as stated by Kaiktsis et. al. [1], that the term "added mass" or "inertia" force does not seem the most appropriate from a physical point of view, since the corresponding component of the force is not 180 degrees out of phase with the acceleration. Consequently, we consider scaling the inertia force component with the dynamic pressure (see Sec.3.2.1), introducing the coefficients C_{L_a} and C_{D_a} for each case. As we can see in Figs.4.1.5-6, scaling the inertia force with the dynamic pressure is overall preferable since it gives more meaningful values for the coefficients C_{L_a} and C_{D_a}, especially for low amplitudes.

In Figs.4.1.7-8 we can see the variation of the lift force fluctuations for each case of forcing. For $\epsilon = 0$, the r.m.s fluctuations seem to be constant, equal to 0.765 with no dependence on the increasing amplitude. However, for $\epsilon \to \infty$ the fluctuations exhibit an increasing trend for reduced amplitudes greater than $A_x/D = 0.15$. This behavior can be associated with the appearance and development of a consistent vortex structure in the wake of the cylinder (see Fig.) and the large increase of the drag force acting upon the structure (see Fig.4.1.10). Also, note that in the x-oscillation case ($\epsilon \to \infty$) the excitation frequency is equal to the natural vortex shedding frequency of the stationary cylinder.

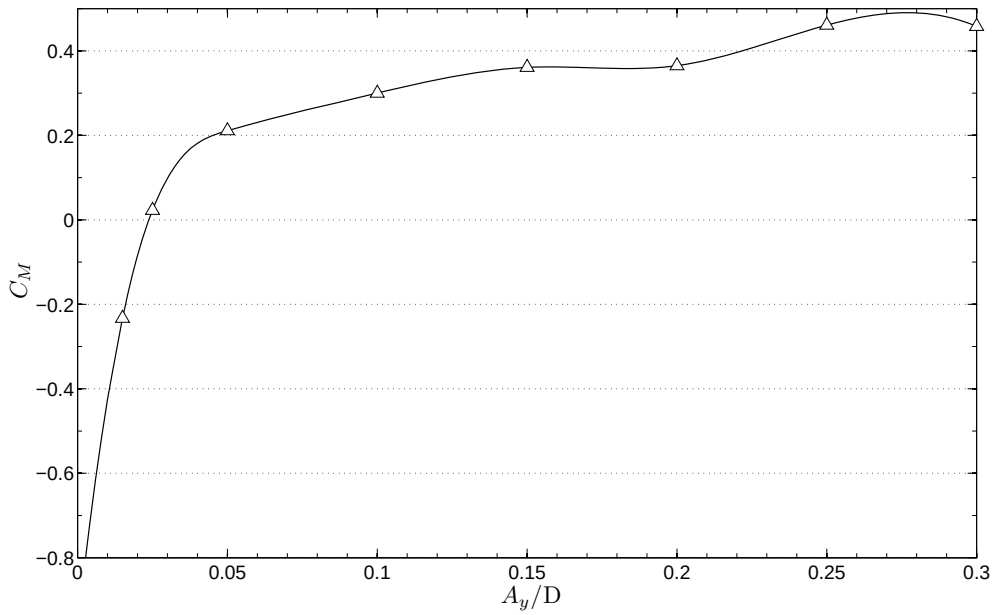

Figure 4.1.3: Inertia force coefficient C_M versus nondimensional excitation amplitude, for $\epsilon = 0$.

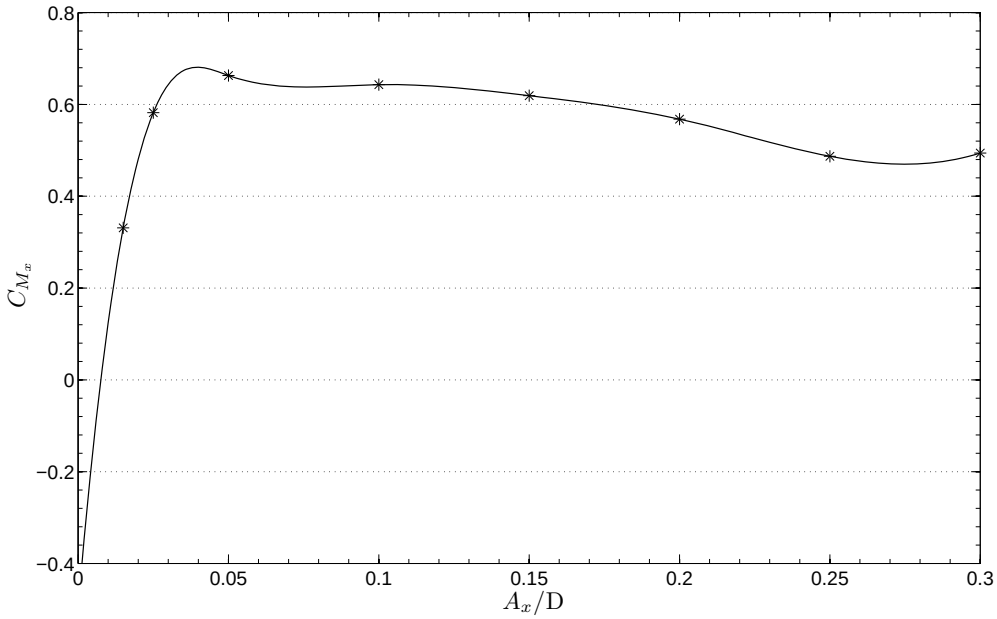

Figure 4.1.4: Inertia force coefficient C_{M_x} versus nondimensional excitation amplitude, for $\epsilon \to \infty$.

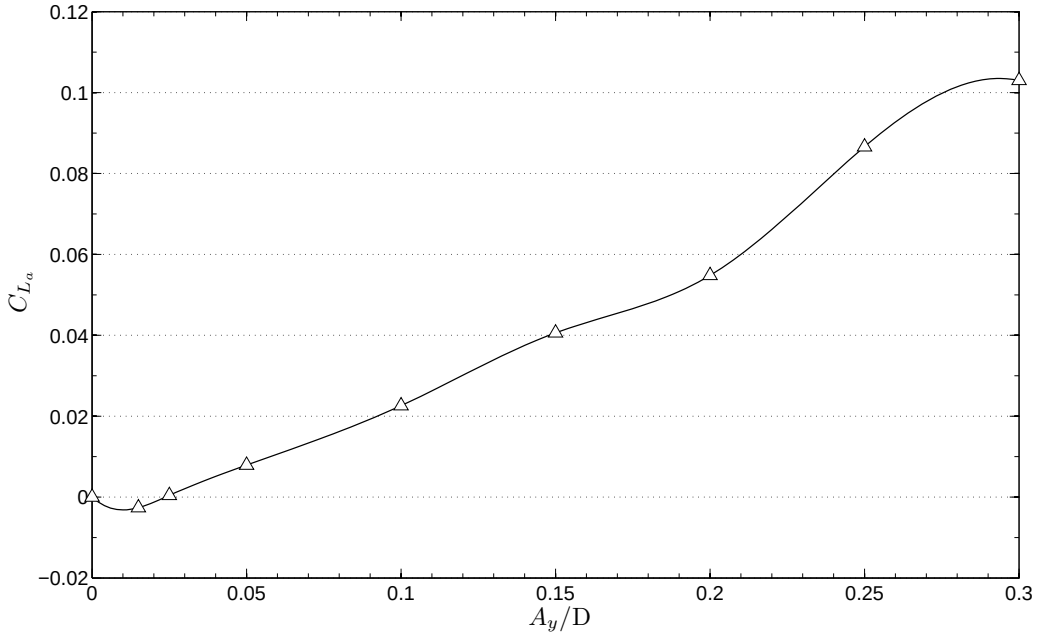

Figure 4.1.5: Inertia force coefficient C_{L_a} versus nondimensional excitation amplitude, for $\epsilon = 0$.

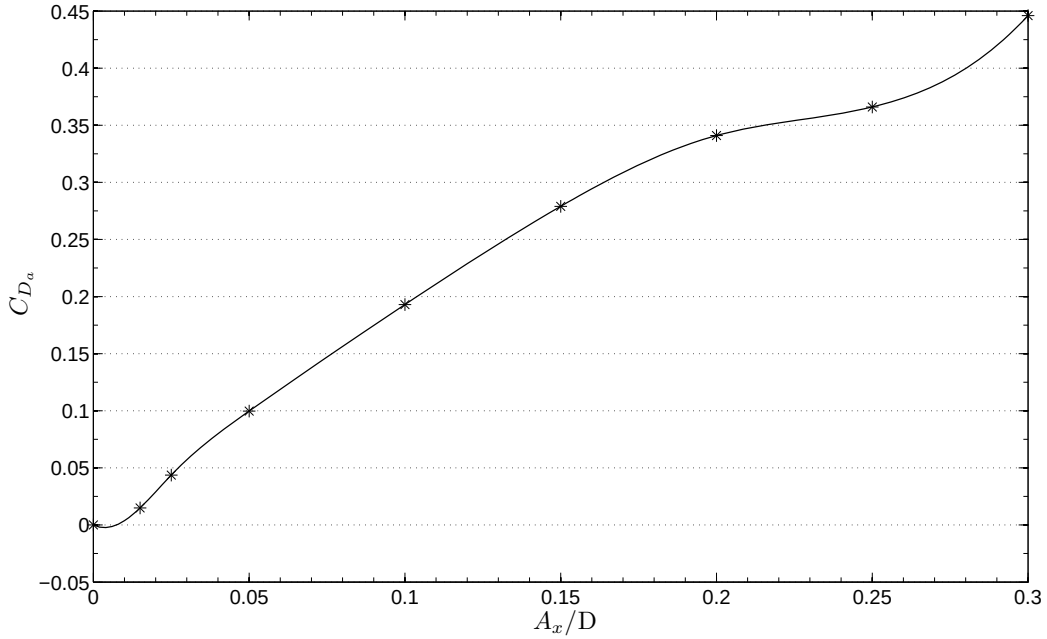

Figure 4.1.6: Inertia force coefficient C_{D_a} versus nondimensional excitation amplitude, for $\epsilon \to \infty$.

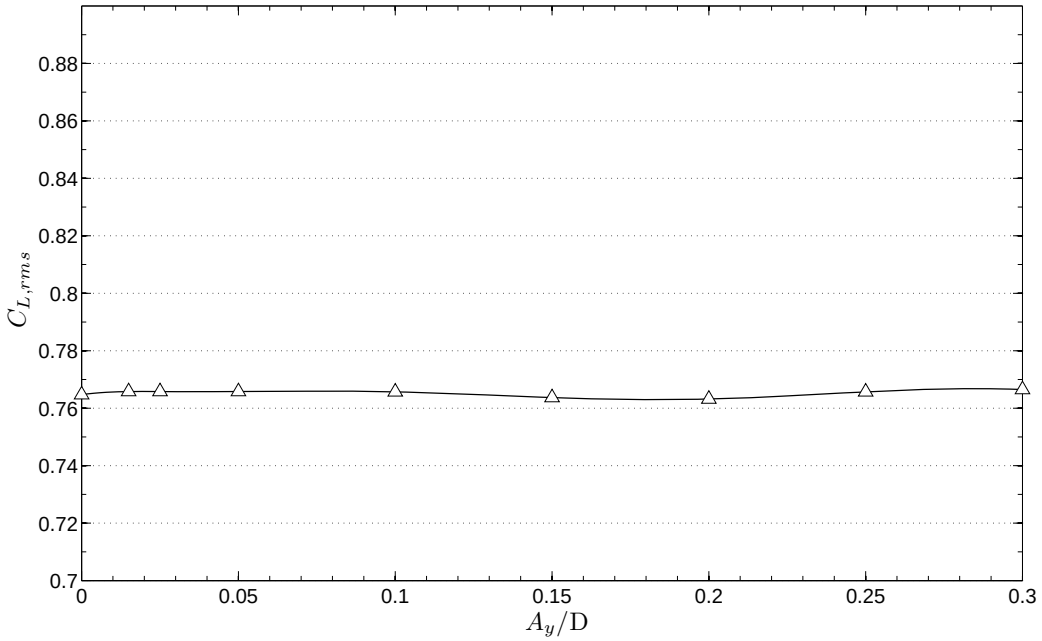

Figure 4.1.7: R.m.s fluctuation intensity of the lift coefficient versus nondimensional excitation amplitude for $\epsilon = 0$.

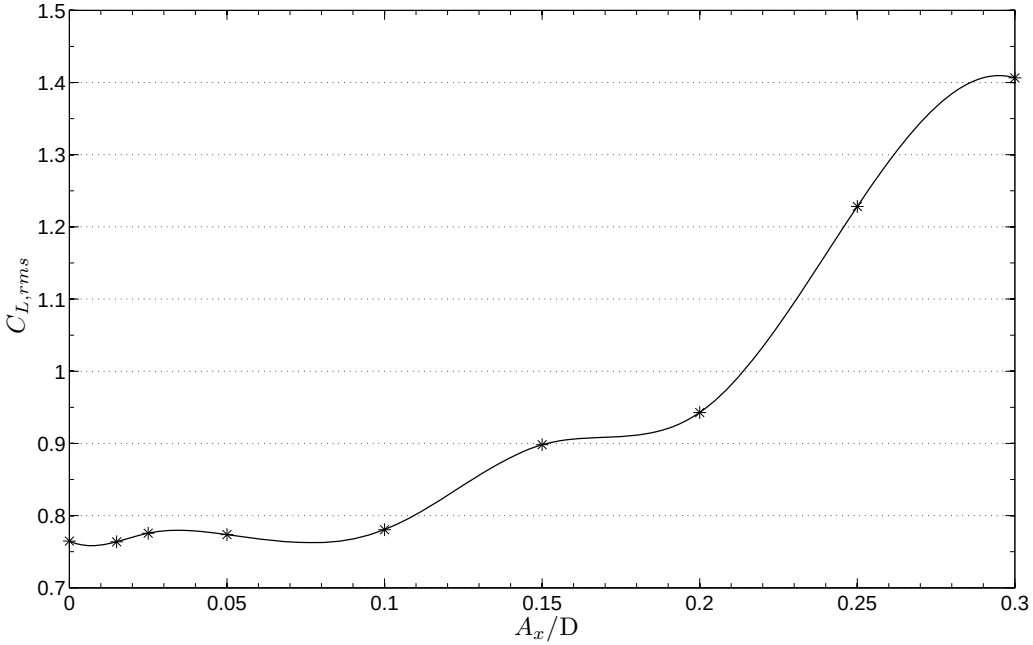

Figure 4.1.8: R.m.s fluctuation intensity of the lift coefficient versus nondimesnional excitation amplitude for $\epsilon \to \infty$.

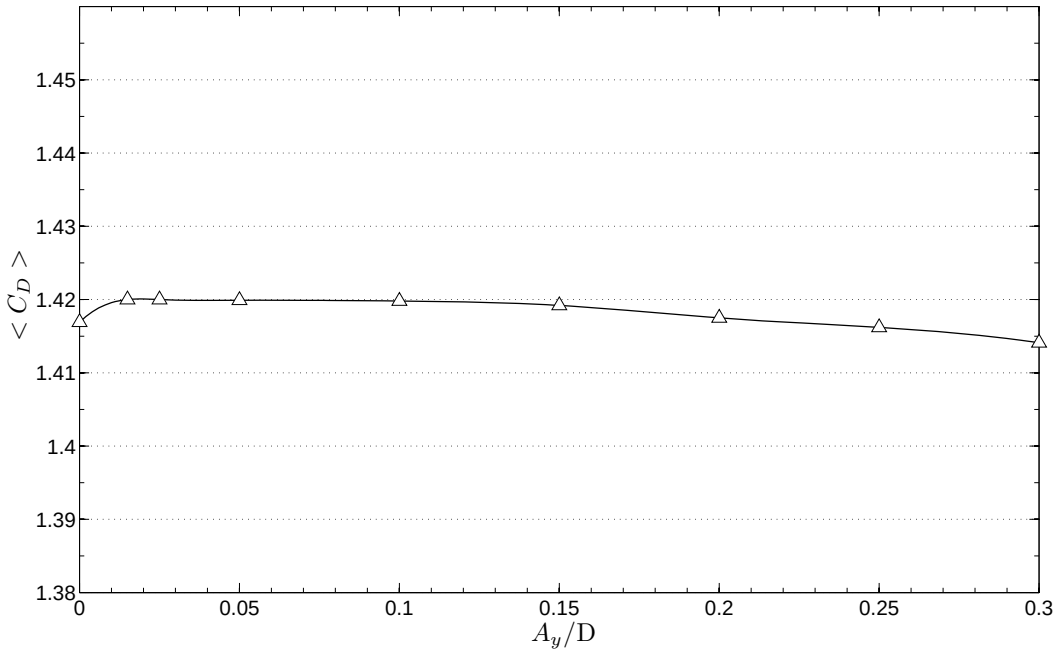

Figure 4.1.9: Time-averaged drag coefficient versus non-dimensional excitation amplitude for $\epsilon = 0$.

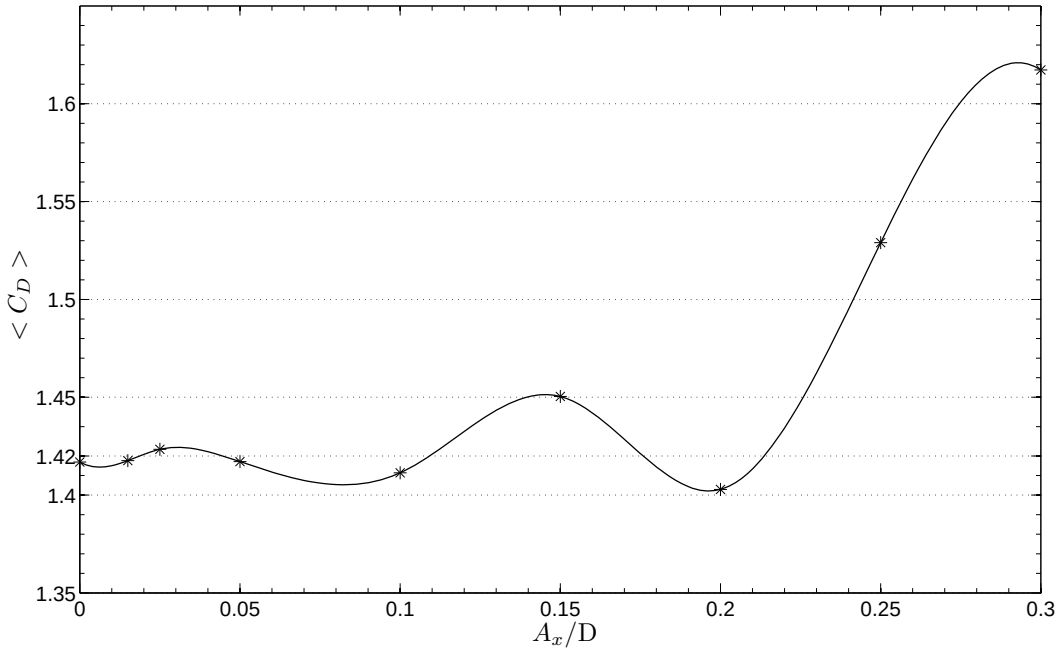

Figure 4.1.10: Time-averaged drag coefficient versus non-dimensional excitation amplitude for $\epsilon \to \infty$.

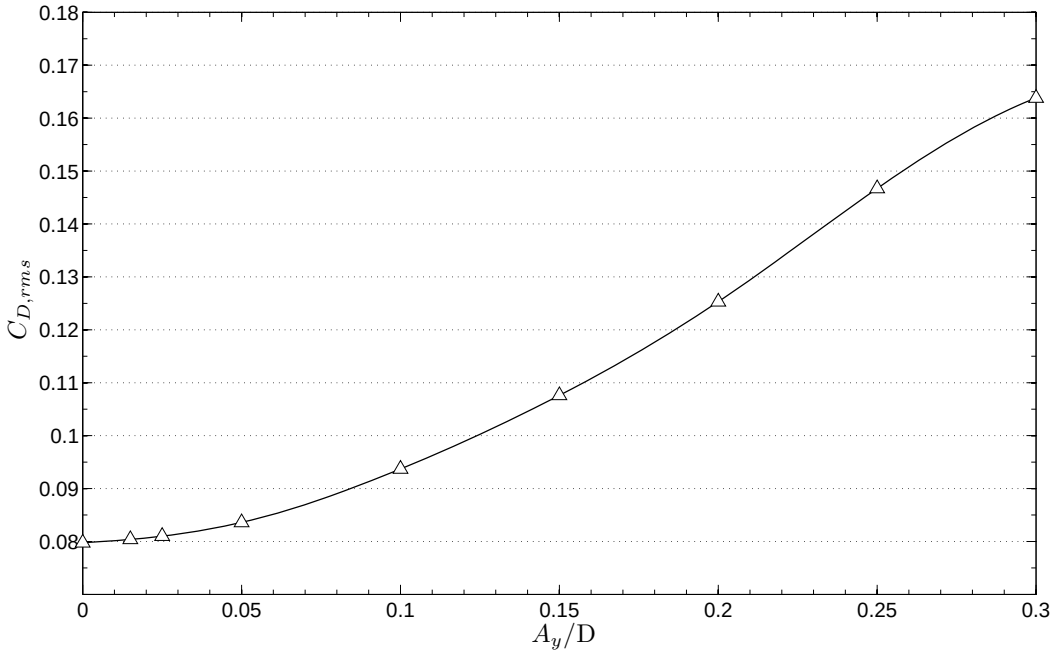

Figure 4.1.11: R.m.s fluctuation intensity of the drag coefficient versus nondimensional excitation amplitude for $\epsilon = 0$.

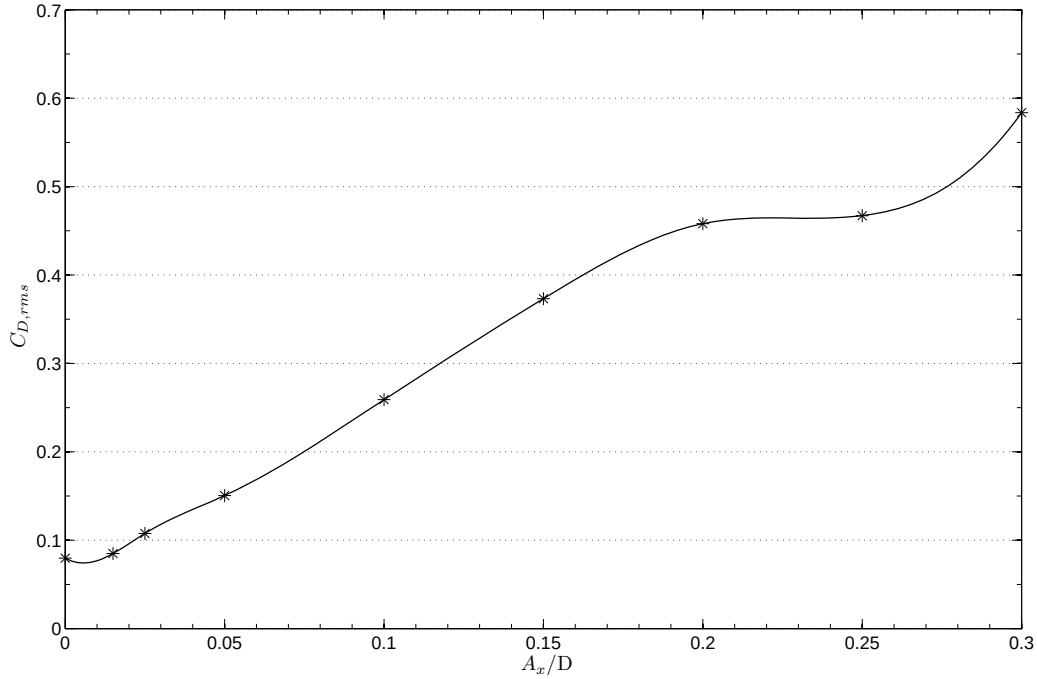

Figure 4.1.12: R.m.s fluctuation intensity of the drag coefficient versus nondimensional excitation amplitude for $\epsilon \to \infty$.

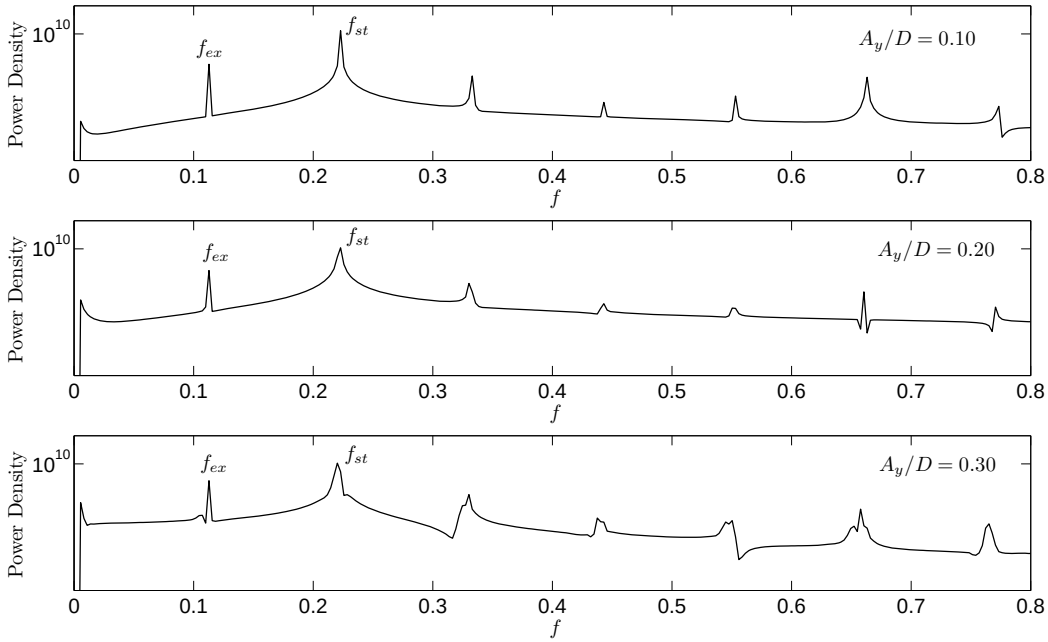

Figure 4.1.13: Lift force frequency spectra for sub-harmonic forcing and purely transverse cylinder oscillation ($F = 0.5$, $\epsilon = 0.5$).

We observe that the time-averaged drag coefficient remains constant and close to a value of 1.42 for $\epsilon = 0$, but demonstrates a large increase up to a value of 1.62 for $\epsilon \to \infty$ and amplitudes greater than $A_x/D \geq 0.15$. In the other hand, the r.m.s drag fluctuations exhibit a similar behavior for both cases, increasing smoothly with the reduced amplitude, but with the fluctuation intensity being much stronger for the $\epsilon \to \infty$ case.

Moreover, by examing the power content of the lift and drag forces in each case we can see that lock-in does not occur in neither case for every reduced oscillation amplitude imposed (ranging from 0˜0.30). Specifically, in Fig.4.1.13 we present the lift force power spectra for the purely transverse cylinder motion case ($\epsilon = 0$), while in Fig.4.1.14 a drag force spectra plot is provided for the pure in-line motion case ($\epsilon \to \infty$).

4.1.2 Two degrees of freedom excitation

In this section we present detailed results that quantify the variation of the hydrodynamic forces acting upon a cylinder forced to vibrate both transversely and in-line to a steady stream. The cylinder traces a "figure 8" path in the x-y plane, emulating the trajectory of a cylinder undergoing free vortex induced vibrations. We have performed numerical simulations for a constant value of R_e equal to 400. The transverse vibration frequency equals half the natural vortex shedding frequency f_{st} (sub-harmonic excitation) while the in-line frequency is equal to twice the transverse frequency and thus equal to f_{st}. The ratio of the in-line to the transverse oscillation amplitude ϵ is equal to 0.2, 0.4 or 0.6.

Previous studies (see Kaiktsis and Triantafyllou [2]) have shown that the oscillation mode ("clockwise" or "counter-clockwise") defines a different physical

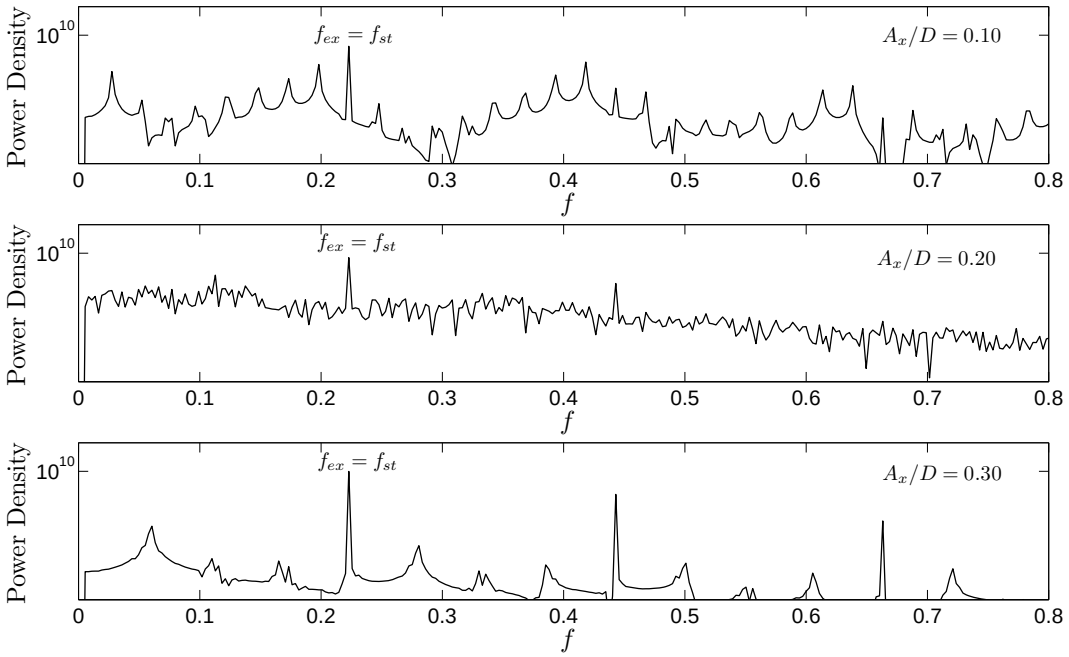

Figure 4.1.14: Drag force frequency spectra for harmonic forcing and purely in-line cylinder oscillation ($F = 1$, $\epsilon \to \infty$).

problem, with the "counter-clockwise" mode being characterized by higher values of the forces acting on the cylinder, as well as by higher values of the power transfer from the flow to the cylinder. Therefore our simulations were primarily focused on the "counter-clockwise" vibration mode, with "clockwise" mode simulations being performed only for $\epsilon = 0.2$, mainly for comparison purposes. Following this setup, we examined four different cases of oscillation depending on the ratio of the in-line to the transverse oscillation amplitude ϵ and the oscillation mode.

In Figs.4.1.15-23 we present the variation of the hydrodynamic coefficients (as in 4.1.1) as well as the time-averaged values and fluctuations of the lift and the drag force coefficients (C_L and C_D).

Note that the lift force excitation coefficient C_{L_v} jumps to real values for $\epsilon = 0.6$ and $A_y/D \succeq 0.24$. Although that positive values of C_{L_v} usually indicate positive power transfer i.e. positive energy flow from the fluid to the cylinder and thus self-excitation, in our case this transition does not affect the overall behavior of the structure. As we can see in Fig.4.2.3, the total power transfer remains negative for all cases of excitation and the positive values of C_{L_v} are only related with the y-direction power transfer component for $\epsilon = 0.6$. In all the other cases, we observe that the excitation force coefficients consistently take negative values. Moreover, Figs.4.2.1-2 give a qualitative picture of the contribution of each of the excitation force components acting upon the cylinder in the transverse or in-line direction. We also note the higher values of both C_{L_v} and C_{D_v} for $\epsilon = 0.2$ and "counter-clockwise" cylinder motion in comparison with the "clockwise" oscillation mode.

As seen in Sec.4.1.1, we scale the inertia force components both with the cylinder acceleration and the dynamic pressure. The second method provides more meaningful results and overcomes the divergence issue that arises when scaling with the acceleration as $A_y/D \to 0$. In Figs.4.1.17-18 we can observe distinct

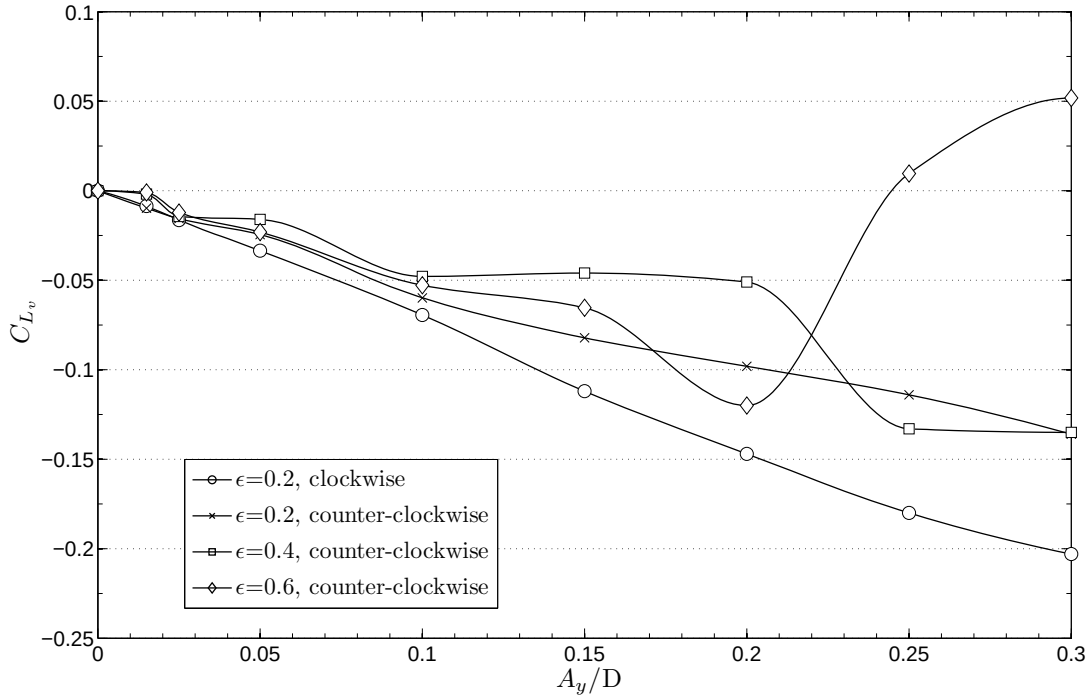

Figure 4.1.15: Y-direction excitation force coefficient C_{L_v} versus nondimensional excitation y-amplitude, for $\epsilon = 0.2$("clockwise" and "counter-clockwise" cylinder motion), $\epsilon = 0.4$ and $\epsilon = 0.6$("counter-clockwise" cylinder motion).

behaviors of C_M and C_{M_x} between the "clockwise" and "counter-clockwise" oscillation modes for $\epsilon = 0.2$. However, looking at Figs.4.1.19-20 we can draw a clearer and more consistent picture of the inertia force variations. Interestingly, the variations of C_{L_a} and C_{D_a} seem to appear in reverse order. For the "counter-clockwise" cases,the y-direction added mass coefficient takes its maximum values for $\epsilon = 0.2$ and "clockwise" motion and gradually decreases as we increase ϵ , while for the x-direction added mass coefficient happens exact the opposite; C_{D_a} is maximized for $\epsilon = 0.6$ and "counter-clockwise" oscillation mode, it decreases evenly as we decrease ϵ and it obtains its minimum values for $\epsilon = 0.2$ and "clockwise" motion.

Figures 4.1.21-23 illustrate the time-averaged values and the r.m.s fluctuations of the lift and drag coefficients. Note that the time-averaged lift coefficient takes values very close to zero for all cases, indicating the presence of a symmetric lift force signal. For $\epsilon = 0.2$ and "clockwise" mode we observe larger fluctuation intensities for both the lift and drag coefficients in comparison with the "counter-clockwise" simulations in which the r.m.s fluctuations vary proportionally with the reduced amplitudes ratio ϵ. Moreover, the time-averaged drag coefficient seems insensitive to A_y/D and constantly takes values close to 1.42 except the case of $\epsilon = 0.6$ and "counter-clockwise" mode where it rapidly increases for $A_y/D \succeq 0.22$, probably due to the large oscillation amplitudes and the formation of a complex and unstructured wake behind the cylinder see (Figs.4.3.5 (c)-(e)). Finally, note that these values are very close to the computed drag coefficient of the stationary cylinder (see beginning of Chapter 4).

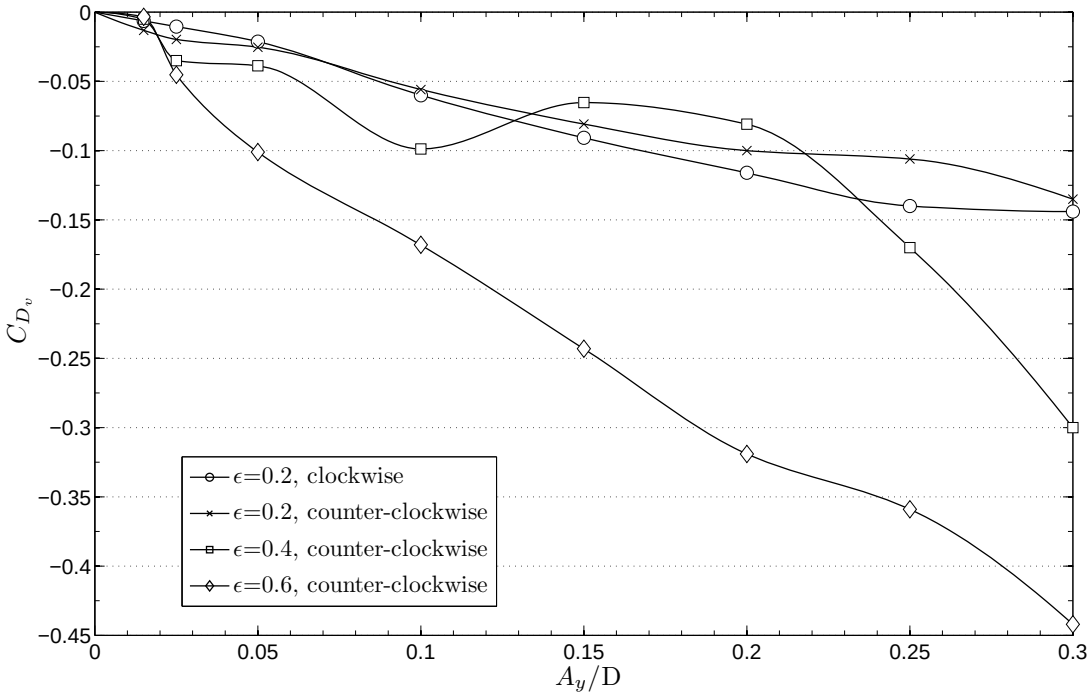

Figure 4.1.16: X-direction excitation force coefficient C_{D_v} versus nondimensional excitation y-amplitude, for $\epsilon = 0.2$("clockwise" and "counter-clockwise" cylinder motion), $\epsilon = 0.4$ and $\epsilon = 0.6$("counter-clockwise" cylinder motion).

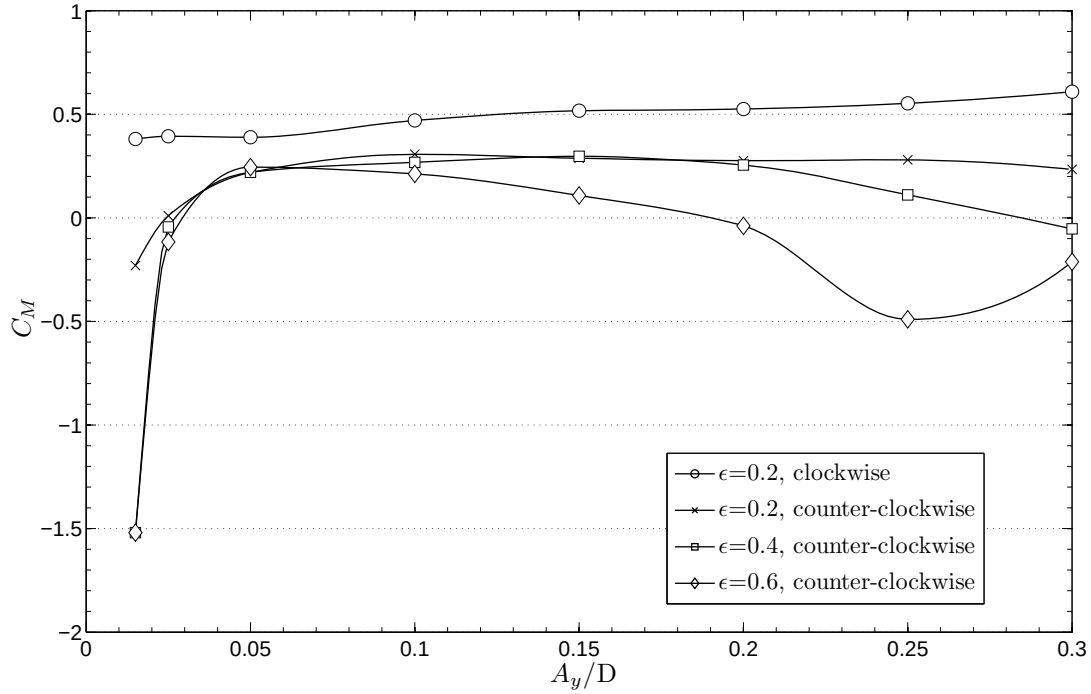

Figure 4.1.17: Y-direction inertia force coefficient C_M versus nondimensional excitation y-amplitude, for $\epsilon = 0.2$("clockwise" and "counter-clockwise" cylinder motion), $\epsilon = 0.4$ and $\epsilon = 0.6$("counter-clockwise" cylinder motion).

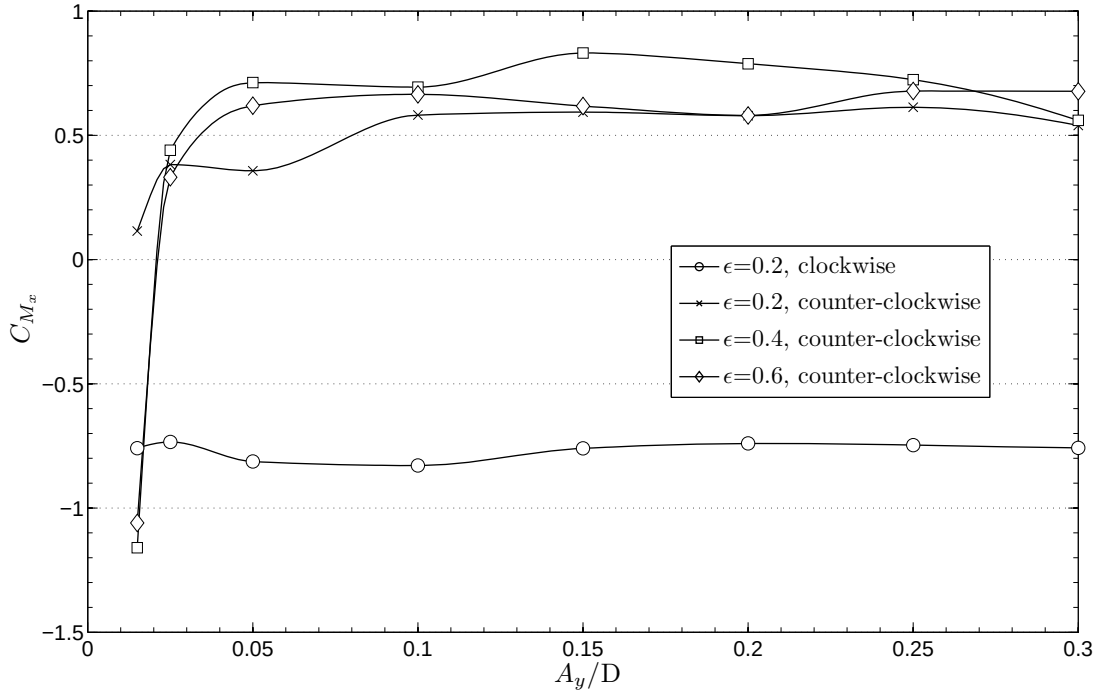

Figure 4.1.18: X-direction inertia force coefficient C_{M_x} versus nondimensional excitation y-amplitude, for $\epsilon = 0.2$("clockwise" and "counter-clockwise" cylinder motion), $\epsilon = 0.4$ and $\epsilon = 0.6$("counter-clockwise" cylinder motion).

Finally, it is meaningful to analyze the calculated forces in the frequency domain. In Figs.4.1.24-25 we can see the frequency spectra of the lift force acting on the cylinder for sub-harmonic forcing, $\epsilon = 0.2$ and "counter-clockwise" oscillation mode. These figures reveal the power content of measured lift force (values on the logarithmic scaled axis) over a range of reduced amplitudes. For all the examined values of A_y/D we note that the prevailing dynamics are dominated by the Strouhal frequency f_{st}, while the imposed excitation frequency f_{ex} corresponds to lower power densities, therefore suggesting that no lock-in phenomena appear (see Triantafyllou and Karniadakis [30]). Interestingly, this behavior was repeated consistently for all the other cases examined ($\epsilon = 0$, $\epsilon = 0.2$ ("clockwise" and "counter-clockwise" mode), $\epsilon = 0.4$, $\epsilon = 0.6$ ("counter-clockwise") and $\epsilon \to \infty$).

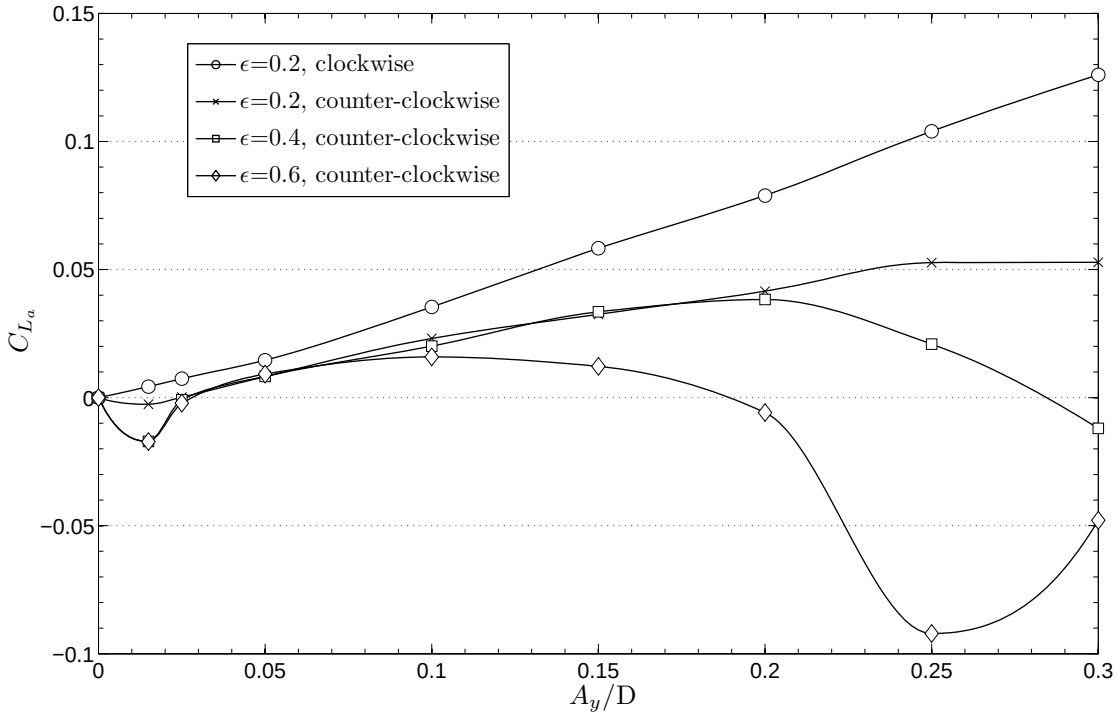

Figure 4.1.19: Y-direction inertia force coefficient C_{L_a} versus nondimensional excitation amplitude, for $\epsilon = 0.2$("clockwise" and "counter-clockwise" cylinder motion), $\epsilon = 0.4$ and $\epsilon = 0.6$("counter-clockwise" cylinder motion).

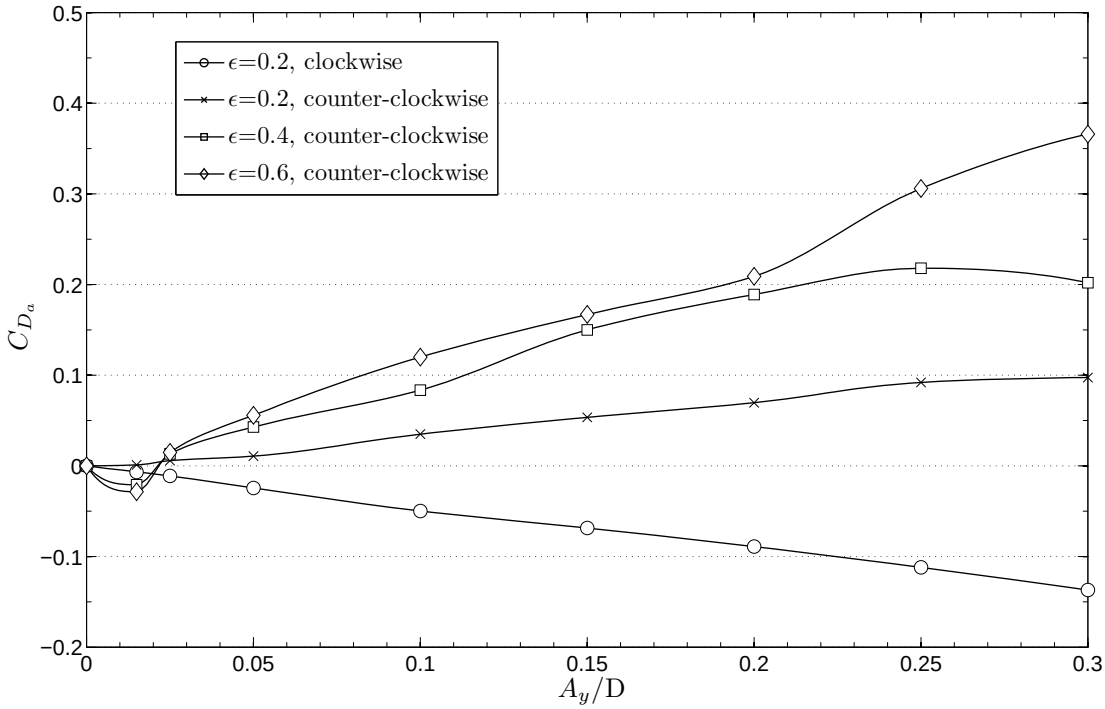

Figure 4.1.20: X-direction inertia force coefficient C_{D_a} versus nondimensional excitation amplitude, for $\epsilon = 0.2$("clockwise" and "counter-clockwise" cylinder motion), $\epsilon = 0.4$ and $\epsilon = 0.6$("counter-clockwise" cylinder motion).

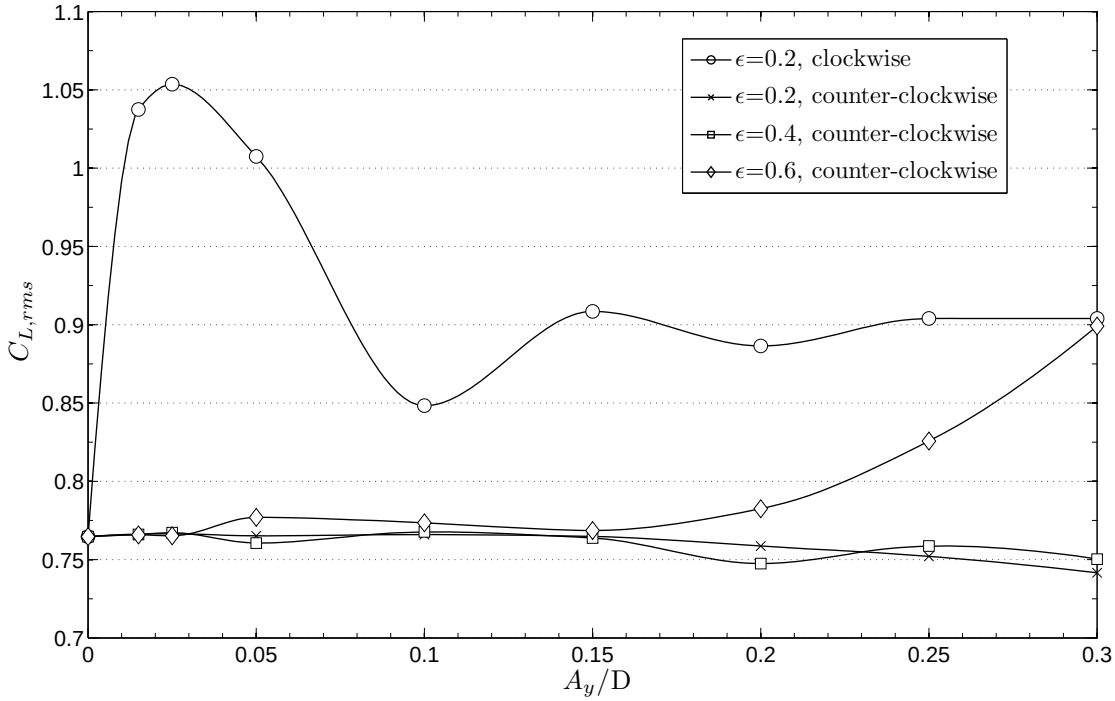

Figure 4.1.21: R.m.s fluctuation intensity of the lift coefficient versus nondimesnional excitation amplitude, for $\epsilon = 0.2$("clockwise" and "counter-clockwise" cylinder motion), $\epsilon = 0.4$ and $\epsilon = 0.6$("counter-clockwise" cylinder motion).

4.2 Power Transfer

The most important outcome of our simulations is the calculation of the energy transfer between the vibrating cylinder and the fluid stream. Integrating the hydrodynamic forces acting on the cylinder's surface we can calculate the power transfer (see Sec.3.2.3) and have a valuable input about whether energy flows from the cylinder to the fluid or vice versa. By examining the variation of the power transfer parameter over a range of reduced amplitudes A_y/D we can also get a qualitative perspective on vortex induced vibrations occurrence. Specifically, positive values of the power transfer parameter indicate that energy flows from the fluid stream to the vibrating cylinder, thus leading to self-excitation and vortex induced vibrations, while negative values assure that energy flows from the cylinder to the fluid, with the fluid having damping effects on the structure.

In Figs.4.2.1-3 we present the variation of the total power transfer parameter P over a range of reduced amplitudes, as well as, its x and y-direction components, denoted by P_x and P_y. All cases correspond to sub-harmonic excitation simulations, except the $\epsilon \to \infty$ case which occurs at resonant forcing.

We observe that P_x falls to smaller values on the negative axis in comparison with P_y, keeping their sum P always negative, in contrast with the results for resonant forcing where regions of positive power transfer existed (see Kaiktsis et. al. [1],[2]). Moreover, we note that in all cases $P \leq P_x \leq P_y$, except for $\epsilon = 0.6$,

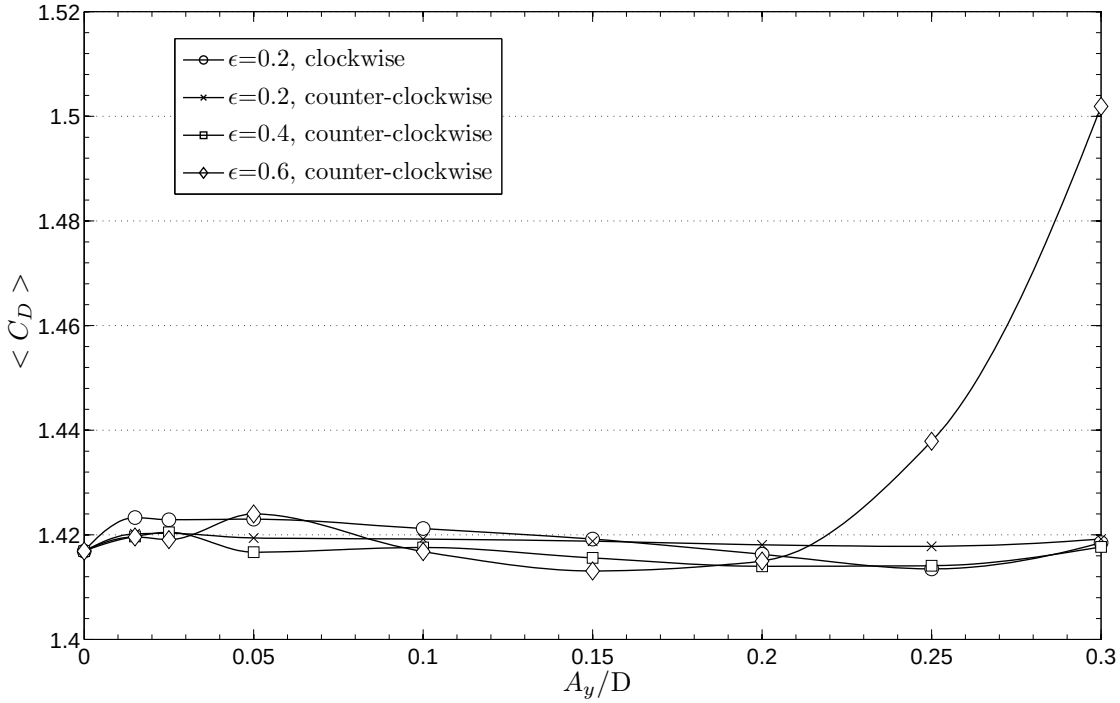

Figure 4.1.22: Time-averaged drag coefficient versus non-dimensional excitation amplitude, for $\epsilon = 0.2$("clockwise" and "counter-clockwise" cylinder motion), $\epsilon = 0.4$ and $\epsilon = 0.6$("counter-clockwise" cylinder motion).

where, for $A_y/D \geq 0.24$, P_y becomes positive and $P_x \leq P \leq P_y$. Comparison of our results with cases of resonant forcing can be found in the Appendix.

As we can see in Fig.4.2.3, the total power transfer remains always negative for every combination of $\{\epsilon, \xi$,oscillation mode$\}$, leading us to the conclusion that our problem setup cannot lead to vortex induced vibrations of the cylinder, as the surrounding fluid acts like damping on the motion of the structure.

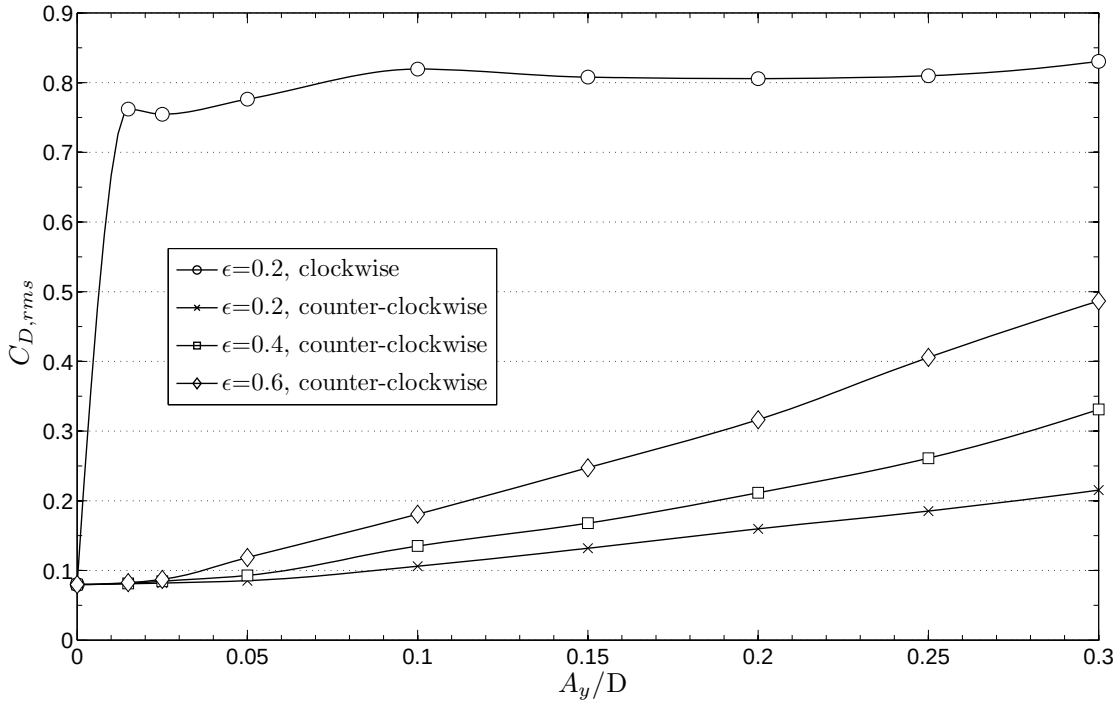

Figure 4.1.23: R.m.s fluctuation intensity of the drag coefficient versus nondimesnional excitation amplitude, for $\epsilon = 0.2$("clockwise" and "counter-clockwise" cylinder motion), $\epsilon = 0.4$ and $\epsilon = 0.6$("counter-clockwise" cylinder motion).

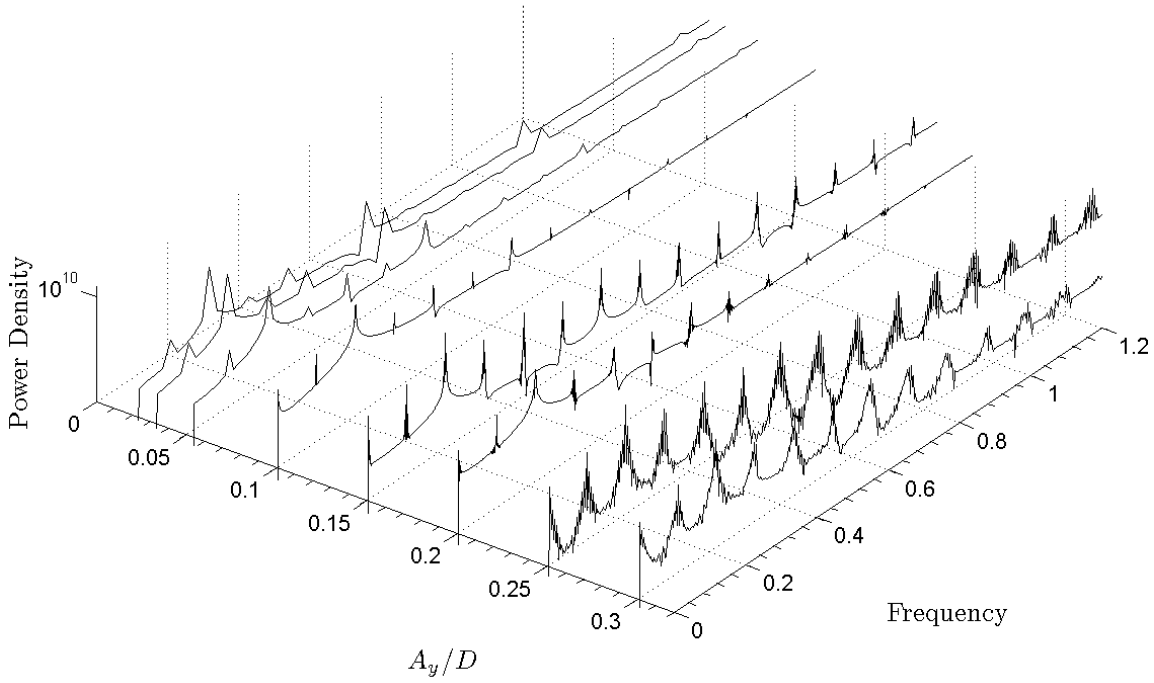

Figure 4.1.24: Lift frequency spectra for sub-harmonic forcing ($\epsilon = 0.2$, "counter-clockwise" cylinder motion).

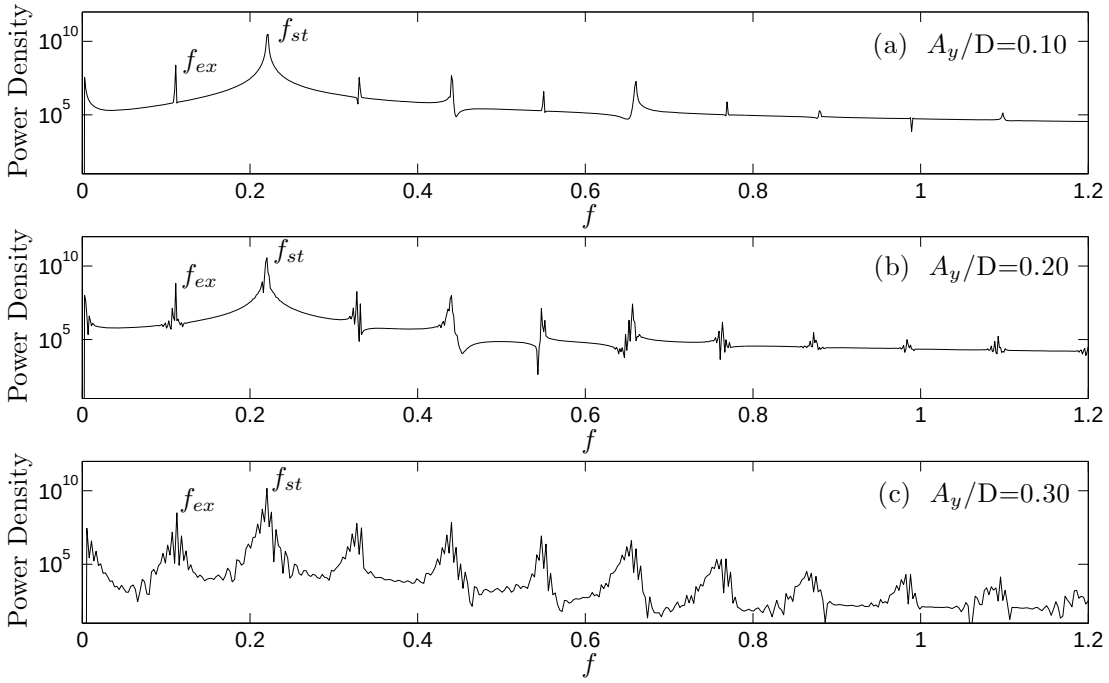

Figure 4.1.25: Lift frequency spectra for sub-harmonic forcing ($\epsilon = 0.2$, "counter-clockwise" cylinder motion).

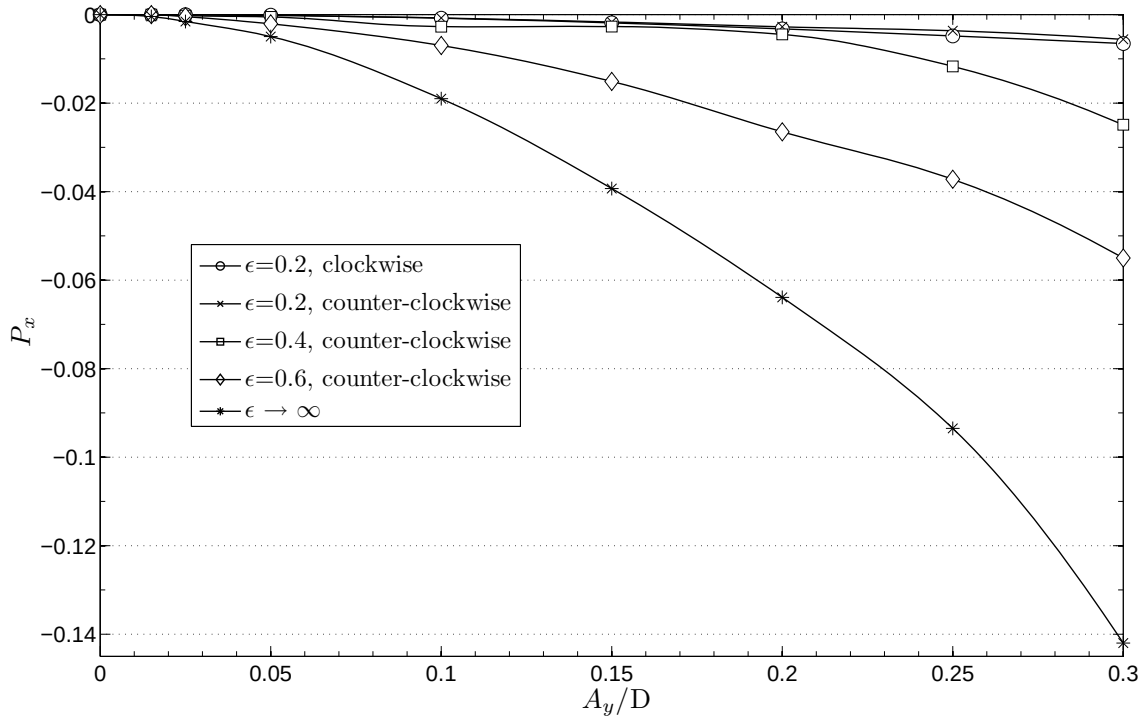

Figure 4.2.1: X-direction power transfer parameter values versus nondimensional excitation y-amplitude for $\epsilon = 0.2$("clockwise" and "counter-clockwise" mode), $\epsilon = 0.4$, $\epsilon = 0.6$("counter-clockwise") and $\epsilon \to \infty$.

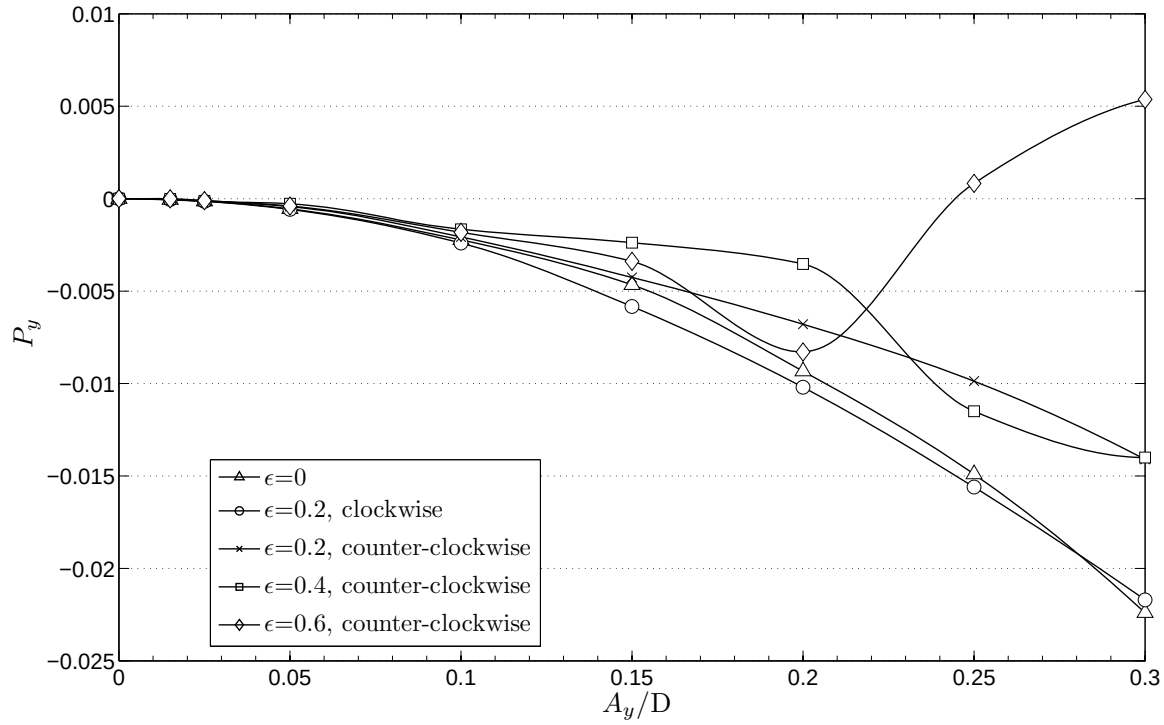

Figure 4.2.2: Y-direction power transfer parameter values versus nondimensional excitation y-amplitude for $\epsilon = 0$, $\epsilon = 0.2$("clockwise" and "counter-clockwise" mode), $\epsilon = 0.4$ and $\epsilon = 0.6$("counter-clockwise") .

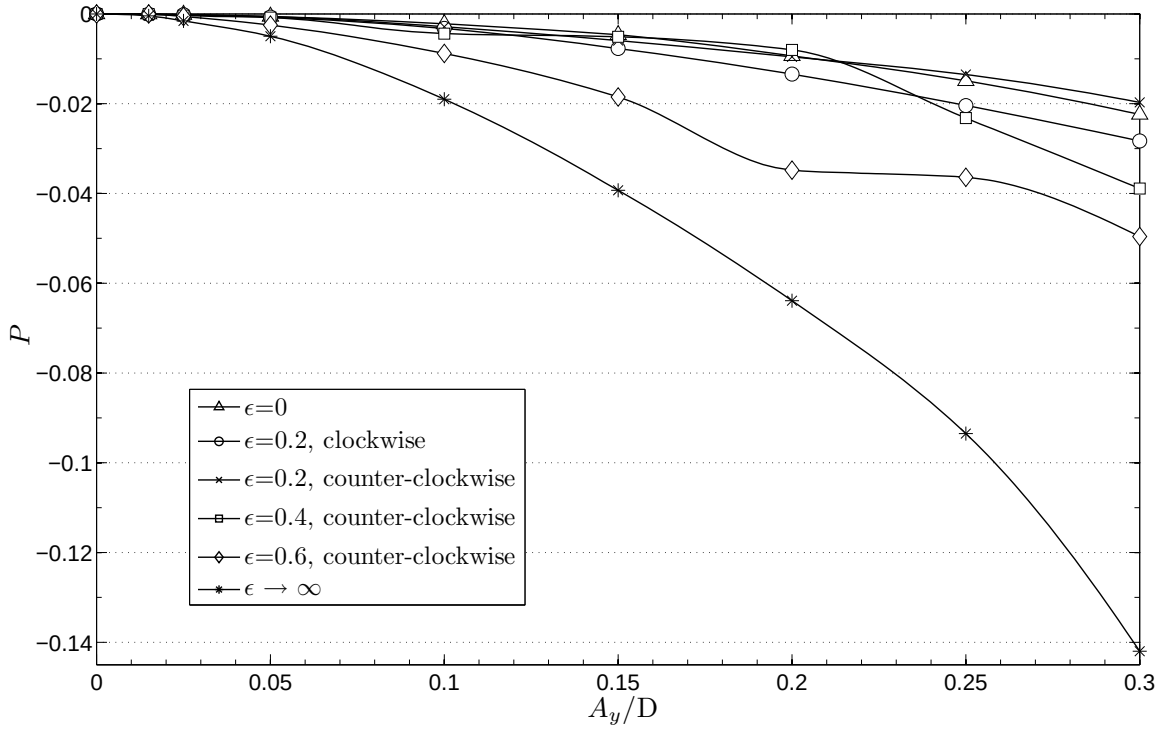

Figure 4.2.3: Total power transfer parameter values versus nondimensional excitation y-amplitude for $\epsilon = 0$, $\epsilon = 0.2$("clockwise" and "counter-clockwise" mode), $\epsilon = 0.4$, $\epsilon = 0.6$("counter-clockwise") and $\epsilon \to \infty$.

4.3 Visualization of the Flow

In this section we present several instantaneous visualizations of the flow in the wake behind the vibrating cylinder. For each case, we have included a number of visualizations over a range of reduced amplitudes in order to demonstrate the evolution of the wake dynamics and its dependence on A_y/D.

Flow visualization can help us relate the variations of the computed hydrodynamic forces to changes noticed in the flow patterns and vortex formation in the wake. Of course, one should be very cautious making such relations because of the fact that these relations are not by any means obvious and straightforward. Particularly, we must notice that changes observed in the flow state (especially if they occur at a distance behind the cylinder) do not necessarily cause changes in the forces acting on the cylinder and vice versa.

Finally, visualizing the flow gives us the ability to make compare the patterns we observe here and the three basic patterns observed experimentally by Williamson and Roshko [16] (see the "Williamson-Roshko map" in 2.2.1), which can be summarized here for easy reference:

- the 2S type of vortex street, in which single vortices are formed on both sides of the cylinder.

- the S+P type of vortex street, in which a single vortex is formed on the one side of the cylinder and a pair of vortices of opposite sign are formed on the other side.

- the 2P type of vortex street, in which pairs of vortices of opposite sign are formed on both sides of the cylinder.

At this point we should also refer to another type of vortex street observed in the previous studies of Kaiktsis et. al. [1], the "partial S+P" mode. This type of vortex street describes the case in which on the one side of the cylinder we see the appearance of vortex pairs, whereas on the other side we see only single vortices.

4.3.1 $\epsilon = 0$

In Figs.4.3.1 (a)-(e) we can see five different visualizations for the case of sub-harmonic y-excitation, which correspond to values of the reduced amplitude A_y/D equal to 0.10, 0.15, 0.20, 0.25 and 0.30, respectively. In all cases we observe the formation of a typical 2S vortex street behind the cylinder. All snapshots are qualitatively similar to each other, indicating that the wake state is rather insensitive to the increasing amplitudes. Eventually, the vortices break up and move away from the center of the wake far downstream, with this transition happening closer to the cylinder as we increase the oscillation amplitude.

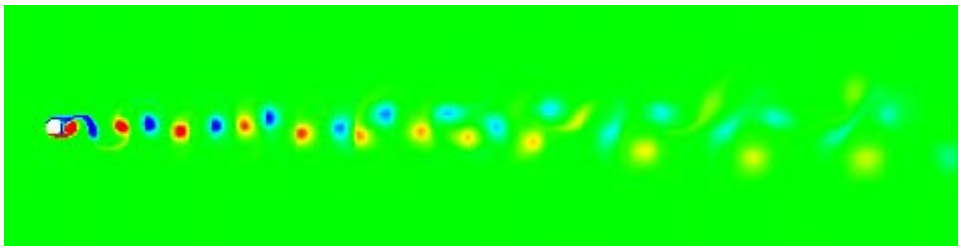

(a) $A_y/D = 0.10$

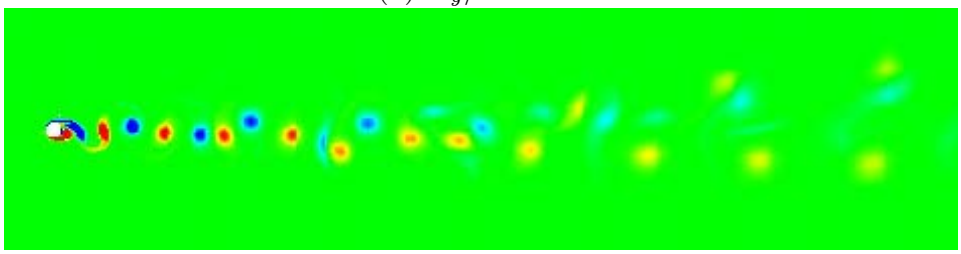

(b) $A_y/D = 0.15$

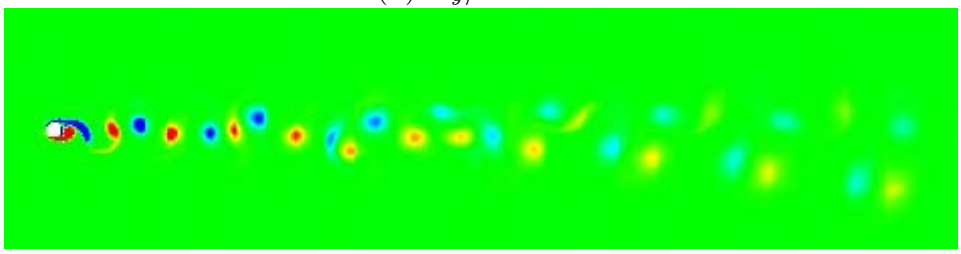

(c) $A_y/D = 0.20$

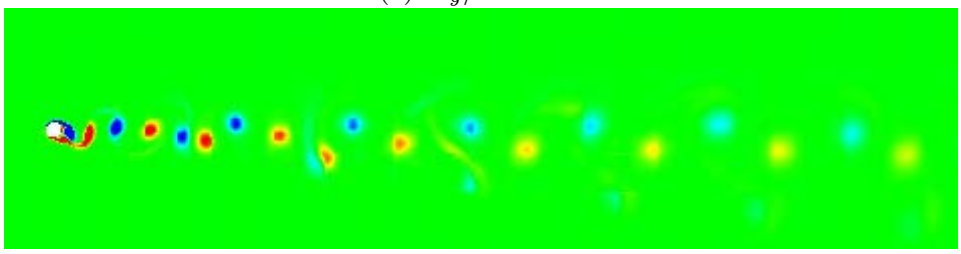

(d) $A_y/D = 0.25$

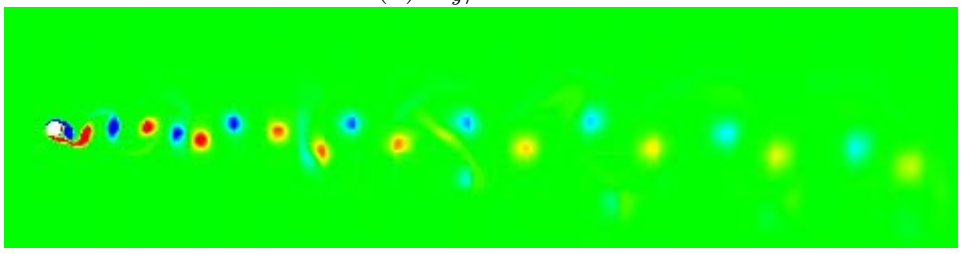

(e) $A_y/D = 0.30$

Figure 4.3.1: Instantaneous vorticity iso-contours for different values of nondimensional excitation amplitude, for $\epsilon = 0$.

4.3.2 $\epsilon = 0.2$, "clockwise" oscillation mode

Figs.4.3.2 (a)-(e) demonstrate the wake structure behind a cylinder oscillating both transversely and in-line to a steady stream, tracing an "8-figure" path the follows the clockwise direction. A regular 2S type vortex street is observed in consistency with the hydrodynamic force variations presented above. Note that in snapshots (d) and (e) the vortices far downstream move away from the center of the wake, indicating a non-symmetric vortex street which causes the appearance

of a non-zero lift force acting on the cylinder (time-averaged lift coefficient values of the order of 0.01).

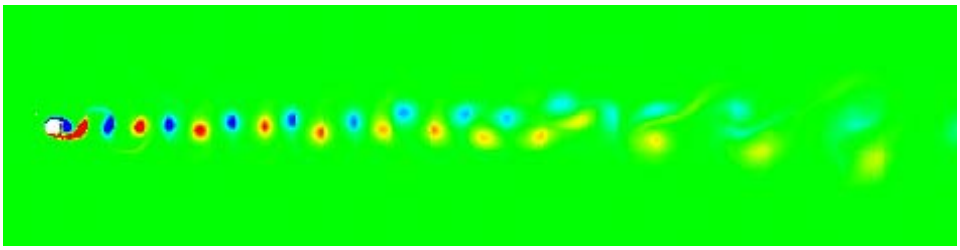

(a) $A_y/D = 0.10$

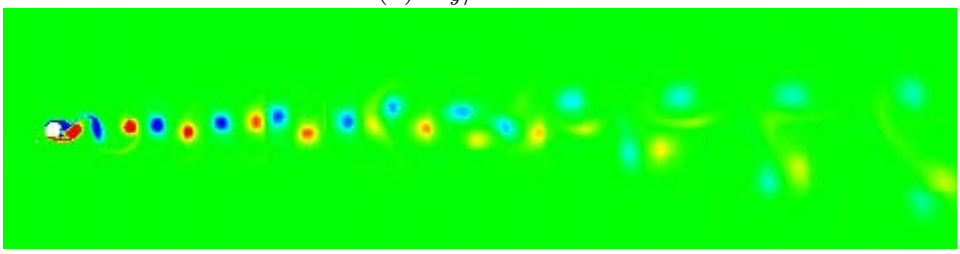

(b) $A_y/D = 0.15$

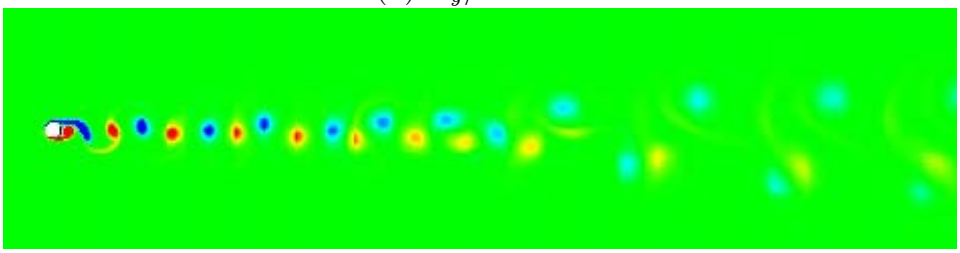

(c) $A_y/D = 0.20$

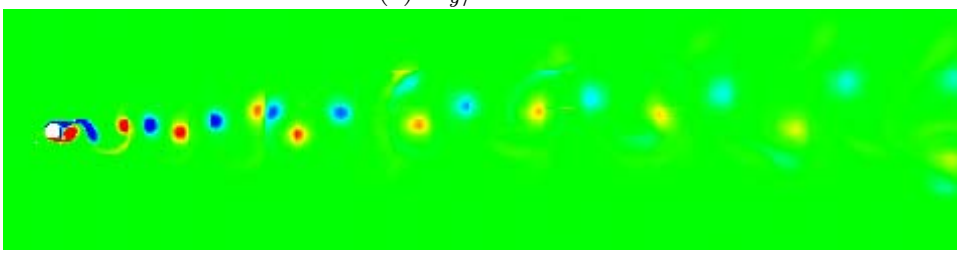

(d) $A_y/D = 0.25$

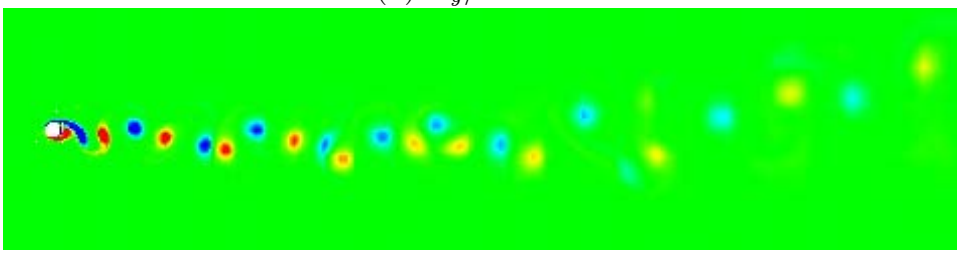

(e) $A_y/D = 0.30$

Figure 4.3.2: Instantaneous vorticity iso-contours for different values of nondimensional excitation y-amplitude, for $\epsilon = 0.2$ and "clockwise" oscillation mode.

4.3.3 $\epsilon = 0.2$, "counter-clockwise" oscillation mode

Fig.4.3.3 (a)-(e) show characteristic vortex streets for the case of $\epsilon = 0.2$ and "counter-clockwise" oscillation mode. The vortex street appears consistently as an orderly 2S type which ends up disordered in the far wake. Note that this break up

of vortices occurs closer to the cylinder as we increase the oscillation amplitude.

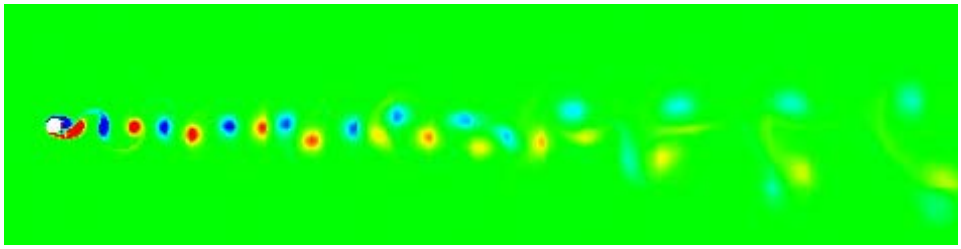

(a) $A_y/D = 0.10$

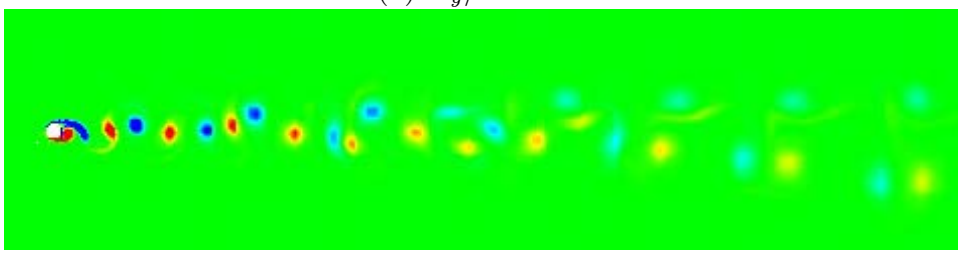

(b) $A_y/D = 0.15$

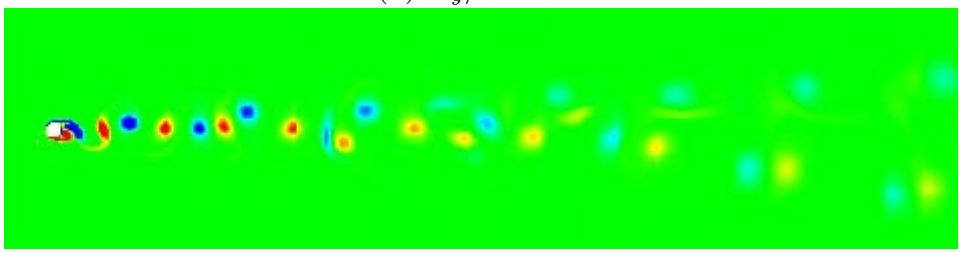

(c) $A_y/D = 0.20$

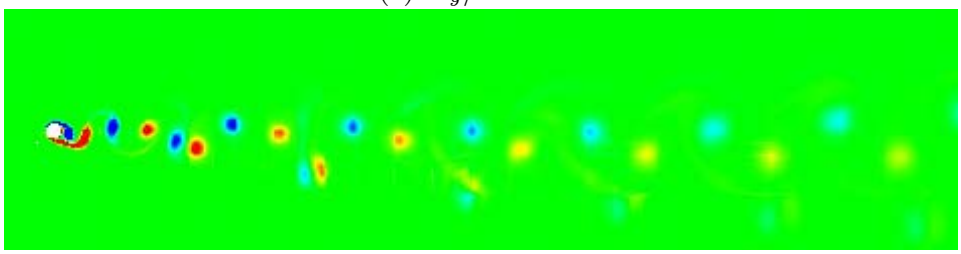

(d) $A_y/D = 0.25$

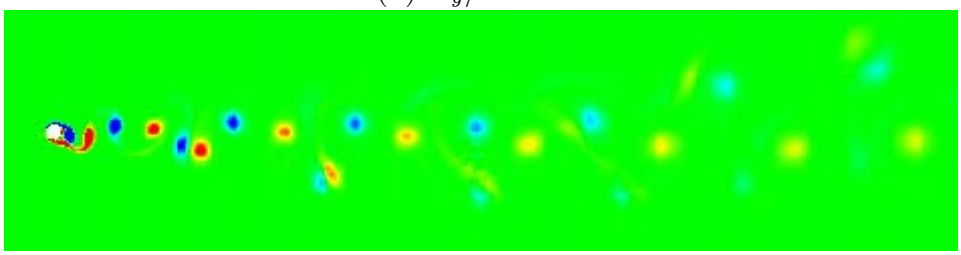

(e) $A_y/D = 0.30$

Figure 4.3.3: Instantaneous vorticity iso-contours for different values of nondimensional excitation y-amplitude, for $\epsilon = 0.2$ and "counter-clockwise" oscillation mode.

4.3.4 $\epsilon = 0.4$, "counter-clockwise" oscillation mode

In Fig.4.3.4 (a)-(e) we have five representative flow visualizations for $\epsilon = 0.4$ and "counter-clockwise" oscillation mode. Again the typical 2S vortex street behavior dominates the flow structure in the wake behind the cylinder. Due to increased oscillation amplitudes, vortices break up and move away from the center

of the wake, forming a non-symmetric unstructured flow pattern.

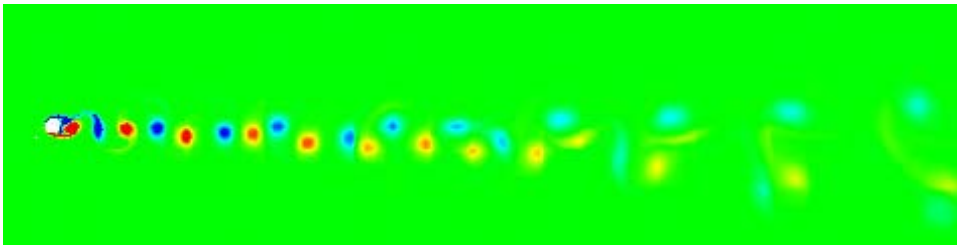

(a) $A_y/D = 0.10$

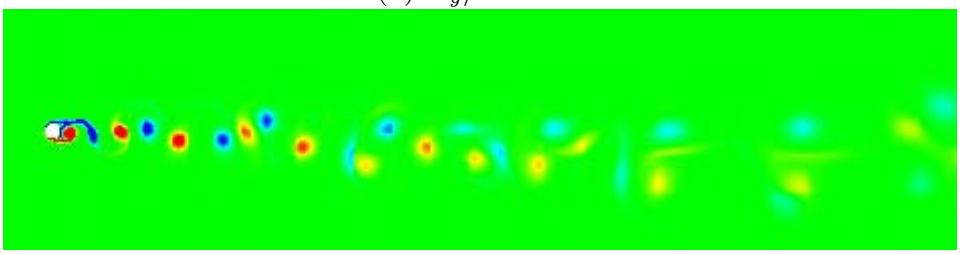

(b) $A_y/D = 0.15$

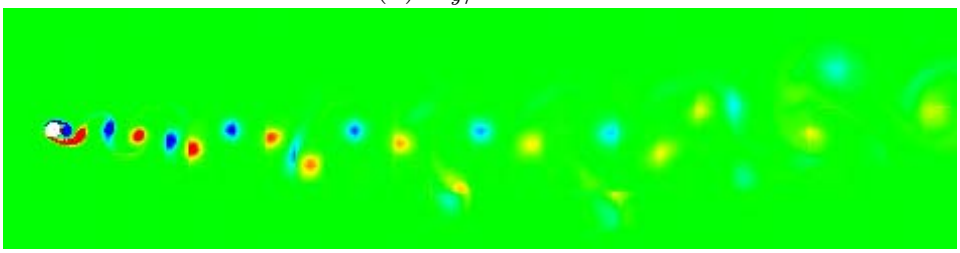

(c) $A_y/D = 0.20$

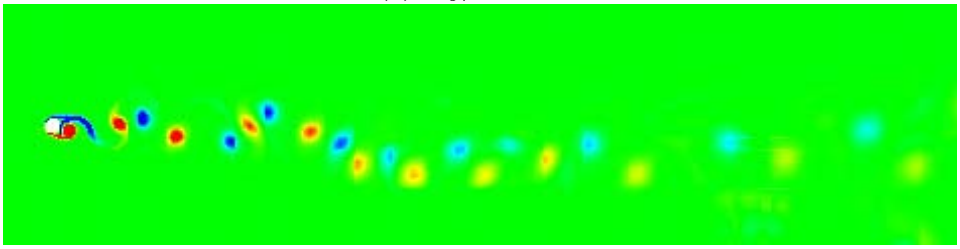

(d) $A_y/D = 0.25$

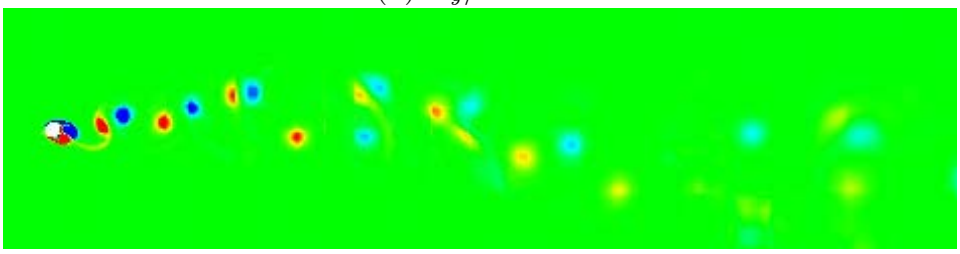

(e) $A_y/D = 0.30$

Figure 4.3.4: Instantaneous vorticity iso-contours for different values of nondimensional excitation y-amplitude, for $\epsilon = 0.4$ and "counter-clockwise" oscillation mode.

4.3.5 $\epsilon = 0.6$, "counter-clockwise" oscillation mode

Fig.4.3.5 (a)-(e) show vorticity iso-contour snapshots for the case of $\epsilon = 0.6$ and "counter-clockwise" oscillation mode. It is straightforward to see that the increased oscillation amplitudes lead to the formation of random and unstructured vortex patterns in the cylinder's wake (snapshots (d),(e)). For lower amplitudes

we can clearly observe the 2S mode for a number of diameters behind the cylinder and a non-symmetric vortex brake up far downstream (snapshots (a)-(c)). It is also reasonable to relate the flow structures observed with the hydrodynamic force variations presented in Sec.4.1.2.

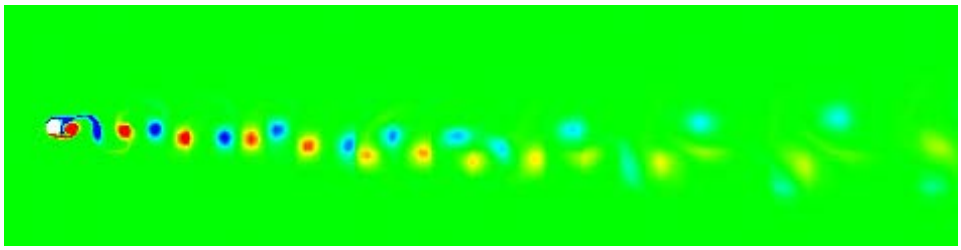

(a) $A_y/D = 0.10$

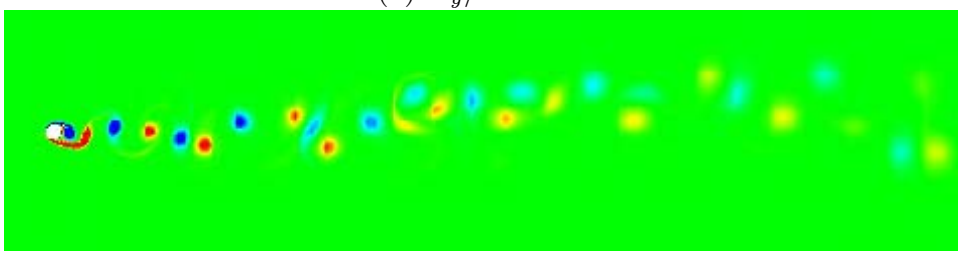

(b) $A_y/D = 0.15$

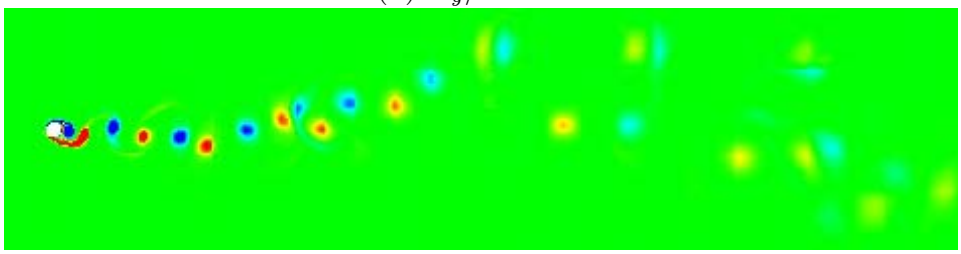

(c) $A_y/D = 0.20$

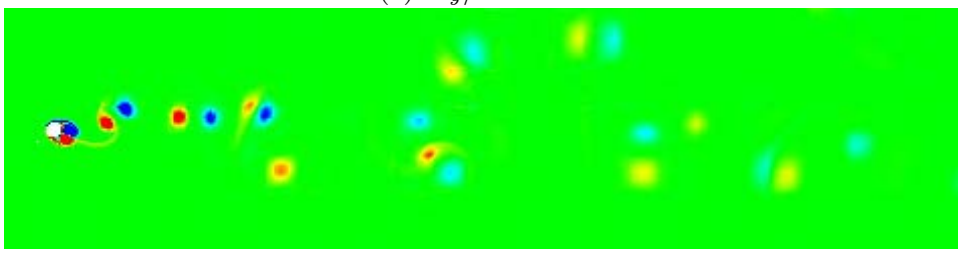

(d) $A_y/D = 0.25$

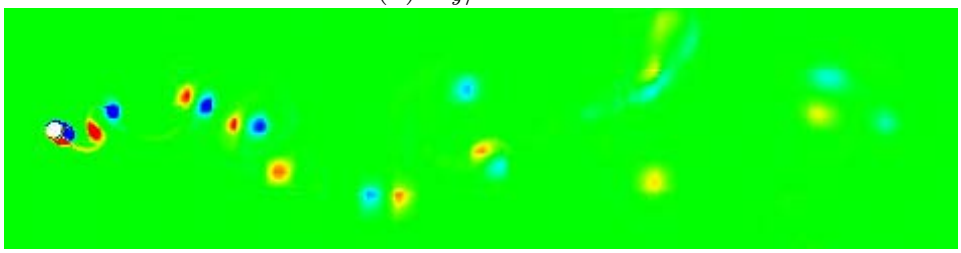

(e) $A_y/D = 0.30$

Figure 4.3.5: Instantaneous vorticity iso-contours for different values of nondimensional excitation y-amplitude, for $\epsilon = 0.6$ and "counter-clockwise" oscillation mode.

4.3.6 $\epsilon \to \infty$

Finally we examine the unique case of in-line only vibrations at resonant forcing. As we can see in Fig.4.3.6 (a), low amplitude oscillations lead to the typical 2S type of vortex street. However, as we gradually increase the oscillation amplitude, the wake becomes considerably more complicated. Interestingly, we note that for $A_y/D \geq 0.15$ the transition in the wake structure is accompanied with a notable transition in the hydrodynamic forces acting upon the cylinder (see Sec.4.1.1). Consequently, one can relate these unstructured flow states with the significant increase of the time-averaged drag coefficient (from 1.42 for $A_y/D = 0.050$ to 1.62 for $A_y/D = 0.30$).

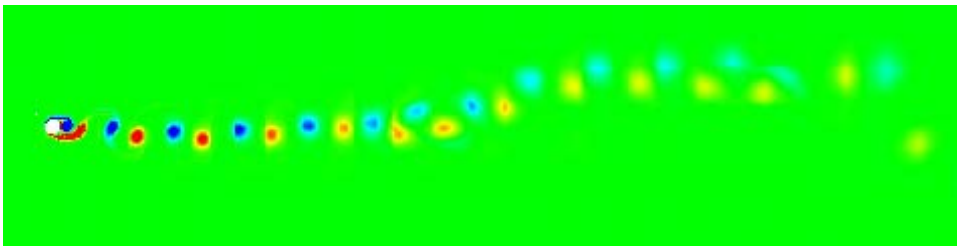

(a) $A_y/D = 0.10$

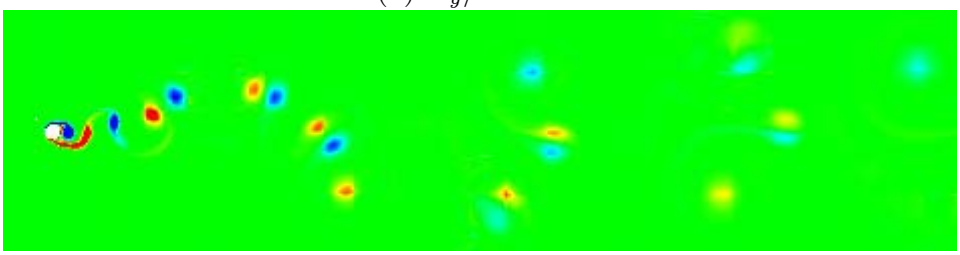

(b) $A_y/D = 0.15$

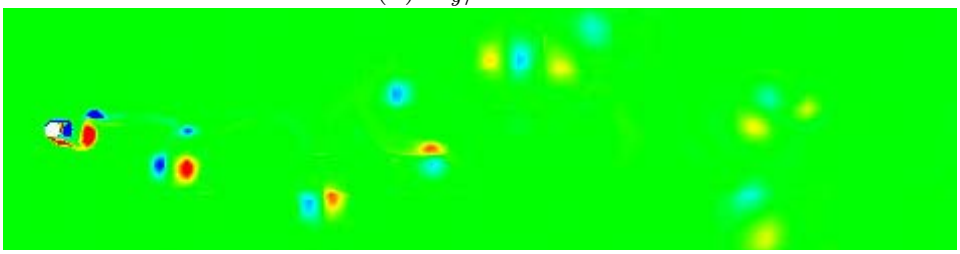

(c) $A_y/D = 0.20$

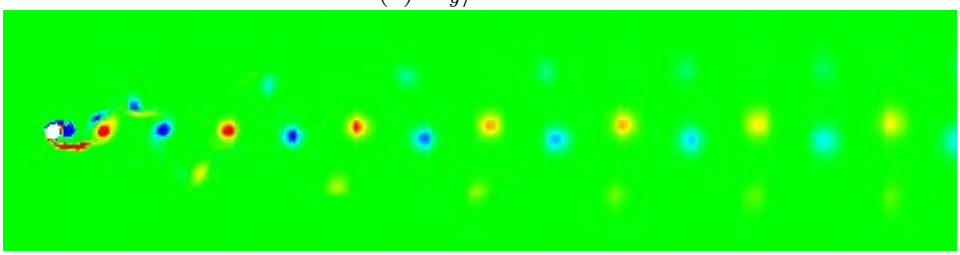

(d) $A_y/D = 0.25$

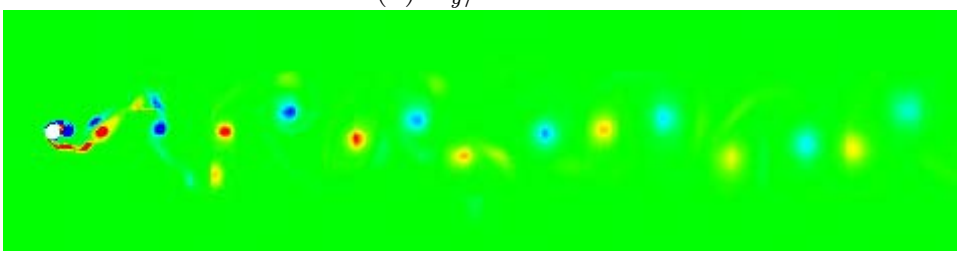

(e) $A_y/D = 0.30$

Figure 4.3.6: Instantaneous vorticity iso-contours for different values of nondimensional excitation y-amplitude, for $\epsilon \to \infty$.

Conclusions

We have presented numerical results for the variation of the forces acting on an oscillating cylinder. We have considered a range of amplitude-over-diameter ratios from 0 to 0.30 for several different cases of cylinder excitation. Our simulations were performed for a relatively low Reynolds number equal to 400, however, conclusions drawn are of interest in the development of models for the dynamics of typical real applications and structures.

A total of three fundamentally different cases was examined in detail. Firstly, we considered the case of purely transverse cylinder oscillation at half the natural frequency of vortex shedding (sub-harmonic forcing). This case is of unique interest not only in terms of modeling flow induced vibrations but also as a non-linear flow dynamics problem. Interestingly, we found that for the range of amplitudes studied here, lock-in does not occur. This conclusion contradicts the literature results of Olinger & Sreenivasan [31] and Stansby [32] in which is stated that vortex shedding can lock on at various submultiples of the natural vortex shedding frequency of the cylinder and for a wide range of excitation amplitudes, including small amplitudes.

Secondly, we performed simulations for the case of purely in-line cylinder oscillation at a frequency equal to the vortex shedding frequency of the stationary cylinder (Strouhal frequency). While pure in-line oscillations are not observed in real structures, this case illustrates some very interesting aspects from the non-linear flow dynamics point of view. Specifically, we observed large variations of the drag force acting on the cylinder, as well as unique complex vortex patterns in the cylinder's wake.

Finally, the case of combined in-line and crossflow excitation was concerned. In this case, the in-line frequency is equal to twice the transverse frequency, while the ratio of the in-line to the transverse oscillation amplitude takes values of 0.2, 0.4 and 0.6. For a flow from left to right, we have distinguished between a "counter-clockwise" mode (if the upper part of the trajectory is traversed counter-clockwise) and a "clockwise" mode (if the upper part of the trajectory is traversed clockwise). The cylinder's transverse excitation is imposed at half the natural vortex shedding frequency while the structure follows an "eight"-like of trajectory, emulating the motion of real cylindrical structures undergoing vortex-induced vibrations. Our primary conclusion is that hydro-elastic resonance is not possible for all cases studied. In particular, the computed power transfer from the fluid to the structure is negative, implying that the presence of the external flow acts as a damper. Even the purely in-line oscillation at the Strouhal frequency is characterized by negative power transfer.

The present results are in accordance to Kaiktsis et. al. [1] in that the value of the power transfer for the "counter-clockwise" mode is less negative than the "clockwise" mode with the same amplitudes, indicating that, in general, the worse scenario for a real structure undergoing VIV is the "counter-clockwise" mode. Fur-

thermore, we found that scaling the excitation component of the lift force with the cylinder acceleration is not always justified, and that, in general, both the excitation and the inertia forces should be scaled with the dynamic pressure. Following the methodology first put forth by Kaiktsis et. al. [1] based on this observation, we deal with the low-amplitudes divergence of the added mass coefficient C_M by scaling both components of the lift force with the dynamic pressure, in other words using coefficient C_{L_a} instead of C_M.

Regarding vortex shedding, all cases exhibited vortex streets resembling the 2-S type. We did not observe any sharp transitions as those reported for the case of transverse oscillation at a frequency near the Strouhal frequency. This behavior was anticipated since the variation of forces with the amplitudes of oscillation is much smoother than in the case of transverse oscillation at a frequency near the Strouhal frequency. The only exception occurred for the case of purely in-line oscillations were we noted a large increase in the drag force with increasing oscillation amplitudes, coupled with very complex vortex patterns in the wake, illustrating the presence of vortex splitting and pairing phenomena.

Subjects for Future Research

Based on the experience gained from the present work the following recommendations are privided for further work on the topic of flow past an oscillating cylinder:

- Implementation of a numerical method dealing with the simulation of a cylinder undergoing free vortex induced vibrations. The method should be capable of solving for each time step both the system of the differential equations governing the motion of the cylinder as a rigid body and the corresponding Navier-Stokes equations governing the fluid flow.

- Computational study of a cylinder vibrating both transversly and in-line to a steady flow, focusing on the effects of super-harmonic excitation.

- Direct numerical two dimensional flow simulations at higher Reynolds numbers. Such simulations should aim at validating and extending our present knowledge in a regime closer to engineering applications.

- Three dimensional direct numerical simulations of a vibrating cylinder in a steady stream.

- Developent of a consistent systematic approach towards the prediction of vortex induced vibrations of engineering structures, combining all tools available (numerical simulations, experimental data, field tests and empirical formulations).

Bibliography

[1] Kaiktsis, L., Triantafyllou, G.S. and Özbas M., 2007. "Excitation, inertia, and drag forces on a cylinder vibrating transversely to a steady flow". *Journal of Fluids and Structures,* **23**(1), pp. 1–21.

[2] Kaiktsis, L. and Triantafyllou, G.S., 2007. "Computational study of hydrodynamic forces on a cylinder vibrating transversely and in-line to a steady stream". Proceedings, Fifth Conference on Bluff Body Wakes and Vortex-Induced Vibrations, Brazil, December 2007 pp. 19–23.

[3] Blevins, R.D., 2001. *Flow-induced vibration*, 2^{nd} ed. Krieger Publishing Company, Malabar, Florida.

[4] Newman, J.N., 1977. *Marine Hydrodynamics.* The MIT Press, Cambridge, Massachusetts.

[5] Sarpkaya, T., 2004. "A critical review of the intrinsic nature of vortex-induced vibrations". *Journal of Fluids and Structures,* **19**(4), pp. 389–447.

[6] Aronsen K.H., 2007. "An experimental investigation of in-line and combined in-line and cross-flow vortex induced vibrations". PhD Thesis, Norwegian University of Science and Technology, Trondheim.

[7] Zdravkovich, M.M., 1997. *Flow around circular cylinders, Vol.1: Fundamentals.* Oxford University Press, Oxford, England.

[8] Zdravkovich, M.M., 2003. *Flow around circular cylinders, Vol.2: Fundamentals.* Oxford University Press, Oxford, England.

[9] Williamson, C.H.K., 1996. "Vortex dynamics in the cylinder wake". *Annual Review of Fluid Mechanics,* **28**, pp. 477–539.

[10] Strogatz, S.H., 2001. *Nonlinear dynamics and chaos.* Westview Press.

[11] Karniadakis, G.E and Triantafyllou, G.S, 1992. "Three-dimensional dynamics and transition to turbulence in the wake of bluff objects". *Journal of Fluid Mechanics,* **238**, pp. 1.

[12] Henderson, R.D and Barkley, D., 1996. "Three-dimensional Floquet stability analysis of the wake of a circular cylinder". *Journal of Fluid Mechanics,* **322**, pp. 215–241.

[13] Moe, G. and Wu, Z.J., 1990. "The lift force on a cylinder vibrating in a current". *ASME Journal of Offshore Mechanics and Arctic Engineering,* **112**, pp. 297–303.

[14] Moe, G., Holden, K. and Yttervol, P.O., 1994. "Motion of spring supported cylinders in subcritical and critical water flows". Proceedings, Fourth International Offshore and Polar Engineering Conference, Osaka, Japan 1994 pp. 468–475.

[15] Sarpkaya, T., 1994. "Hydrodynamic damping, flow-induced oscillations and biharmonic response".. *ASME Journal of Offshore Mechanics and Arctic Engineering,* **117**, pp. 232–238.

[16] Williamson, C.H.K. and Roshko, A., 1988. "Vortex formation in the wake of an oscillating cylinder". *Journal of Fluids and Structures,* **2**, pp. 355–381.

[17] Bearman, P.W., 1984. "Vortex shedding from oscillating objects". *Annual Review of Fluid Mechanics,* **16**, pp. 195–222.

[18] Williamson, C.H.K. and Govardhan, R., 2004. "Vortex-induced vibrations". *Annual Review of Fluid Mechanics,* **36**, pp. 413–455.

[19] Grinstein, F.F. and Karniadakis, G.E., 2002. "Alternative LES and hybrid RANS/LES for turbulent flows". *Journal of Fluids Engineering,* **124**, pp. 821–822.

[20] Patera, T.A., 1984. "A spectral element method for fluid dynamics - Laminar flow in a channel expansion". *Journal of Computational Physics,* **54**, pp. 468–488.

[21] Karniadakis, G.E and Sherwin, S.J., 2005. *Spectral/hp element methods for CFD*, 2^{nd} ed. Oxford University Press, New York, USA.

[22] Pozrikidis, C., 1997. *Introduction to Theoretical and Computational Fluid Dynamics*. Oxford University Press, New York, USA.

[23] Pozrikidis, C., 2005. *Introduction to Finite and Spectral Element Methods using Matlab*. Chapman Hall/CRC Press, Virginia, USA.

[24] Karniadakis, G.E., 1989 "Spectral element simulations of laminar and turbulent flows in complex geometries". *Applied Numerical Mathematics,* **6**, pp. 58–105.

[25] Karniadakis, G.E., Israeli, M. and Orszag, S.A., 1991. "High-order splitting methods for the incompressible Navier-Stokes equations". *Journal of Computational Physics,* **97**, pp. 414–443.

[26] Delaunay, Y. and Kaiktsis, L., 2001. "Control of circular cylinder wakes using base mass transpiration". *Physics of Fluids,* **13**(11), pp. 3285–3302.

[27] Kaiktsis, L. and Monkewitz, P.A., 2003. "Global destabilization of flow over a backward-facing step". *Physics of Fluids,* **15**(12), pp. 3647–3685.

[28] Evangelinos, C. ang Karniadakis, G.E., 1999. "Dynamics and flow structures in the turbulent wake of rigid and flexible cylinders subject to vortex induced vibrations". *Journal of Fluid Mechanics,* **400**, pp. 91–124.

[29] Blackburn, H.M. and Henderson, R.D., 1999. "A study of two-dimensional flow past an oscillating cylinder". *Journal of Fluid Mechanics,* **385**, pp. 255–286.

[30] Karniadakis, G.E. and Triantafyllou, G.S., 1989. "Frequency selection and asymptotic states in laminar wakes". *Journal of Fluid Mechanics,* **199**, pp. 441–469.

[31] Olinger D.J. , Sreenivasan, K.R., 1988. "Nonlinear dynamics in the wake of an oscillating cylinder". *Physical Review Letters,* **60**(9), pp. 797–800.

[32] Stansby P.K. ,1976. "The locking-on of vortex shedding due to the cross-stream vibration of circular cylinders in uniform and shear flows". *Journal of Fluid Mechanics,* **74**(4), pp. 641–665.

Appendix

Comparison of Results with Resonant Forcing Simulations

In this section we compare the main results of the present simulations (corresponding to sub-harmonic excitation) against those of previous studies ([1], [2]) dealing with the case of resonant excitation. Thus, we examine the cases of sub-harmonic forcing i.e. at a transverse frequency equal to half the natural vortex shedding frequency ($F = 0.5$), and resonant forcing (excitation at a frequency equal with the natural vortex shedding frequency of the stationary cylinder, $F = 1$). For each of those two cases we present results for $\epsilon = 0, 0.2$ ("clockwise" and "counter-clockwise") and 0.4 ("counter-clockwise"). Figures 0.1-12 illustrate the qualitative difference of the cases examined, as depicted by the total power transfer parameter P, the excitation force coefficient C_{L_v} and the inertia force coefficients C_M and C_{L_a}.

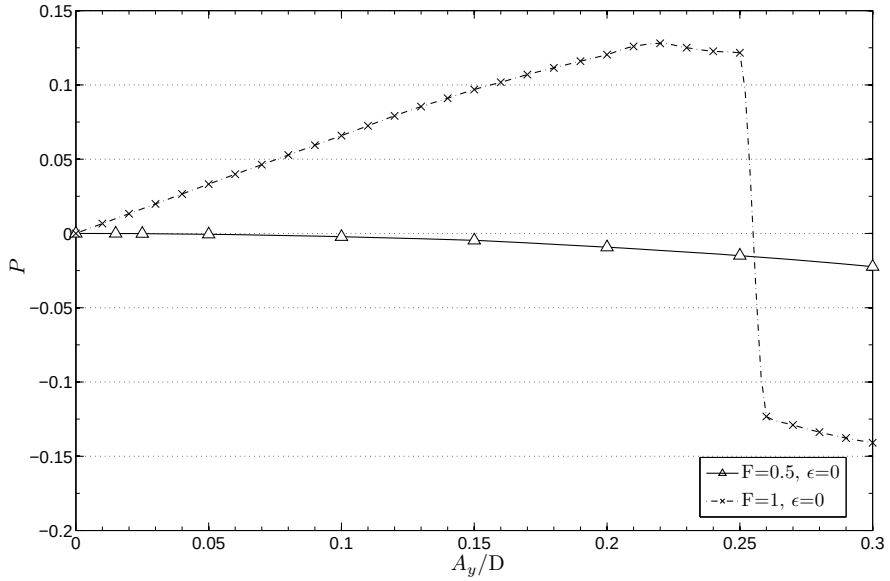

Figure .0.1: Total power transfer parameter values versus nondimensional excitation y-amplitude for $\epsilon = 0$: $F = 0.5$ (sub-harmonic excitation), $F = 1$ (resonant excitation).

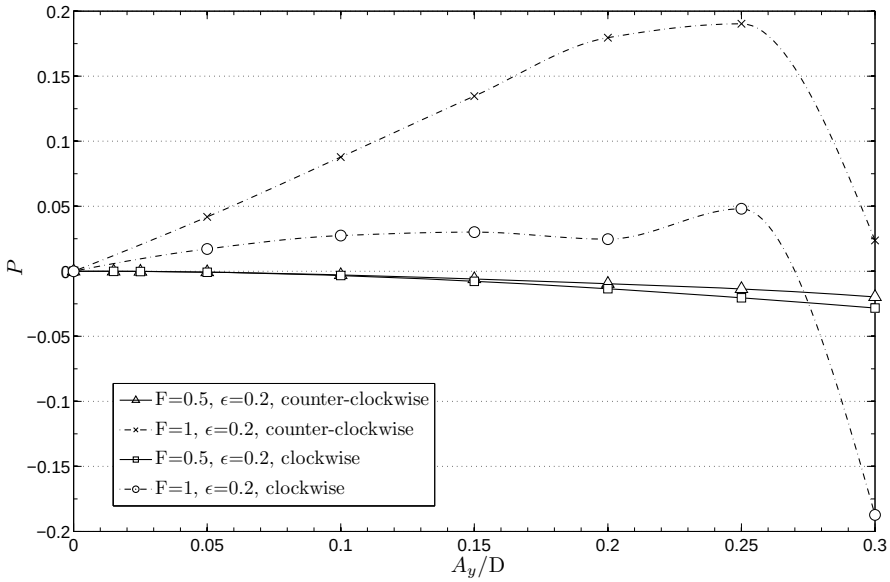

Figure .0.2: Total power transfer parameter values versus nondimensional excitation y-amplitude for $\epsilon = 0.2$ ("clockwise and "counter-clockwise" mode): $F = 0.5$ (sub-harmonic excitation), $F = 1$ (resonant excitation).

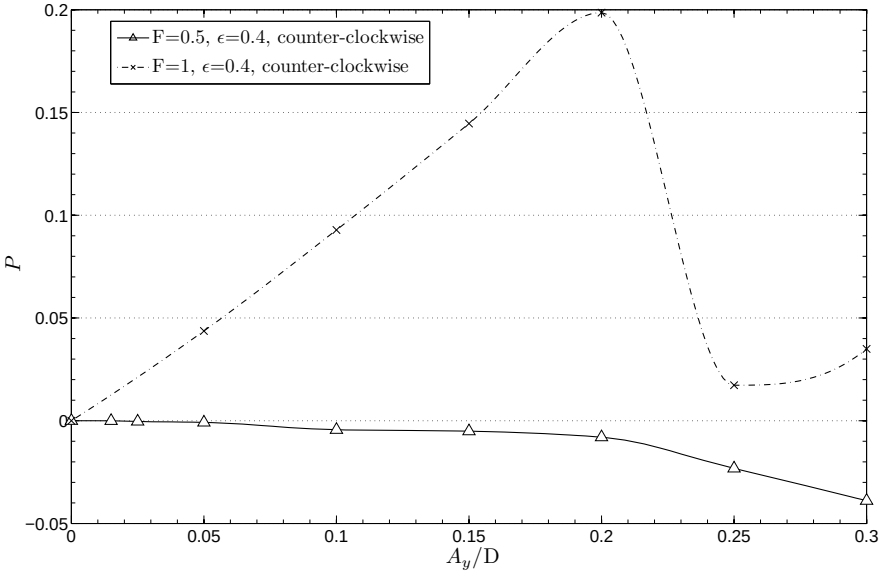

Figure .0.3: Total power transfer parameter values versus nondimensional excitation y-amplitude for $\epsilon = 0.4$ ("counter-clockwise" mode): $F = 0.5$ (sub-harmonic excitation), $F = 1$ (resonant excitation).

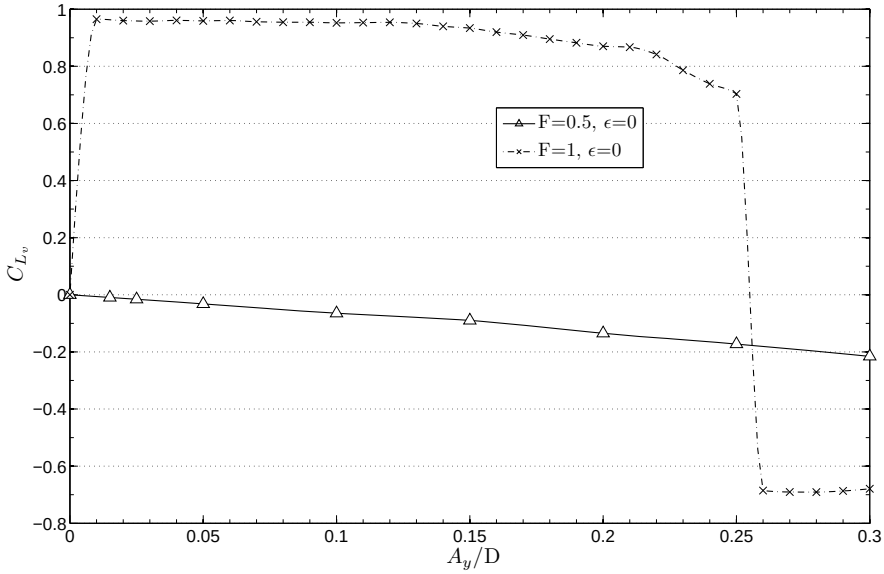

Figure .0.4: Excitation force coefficient C_{L_v} versus nondimensional excitation y-amplitude for $\epsilon = 0$: $F = 0.5$ (sub-harmonic excitation), $F = 1$ (resonant excitation).

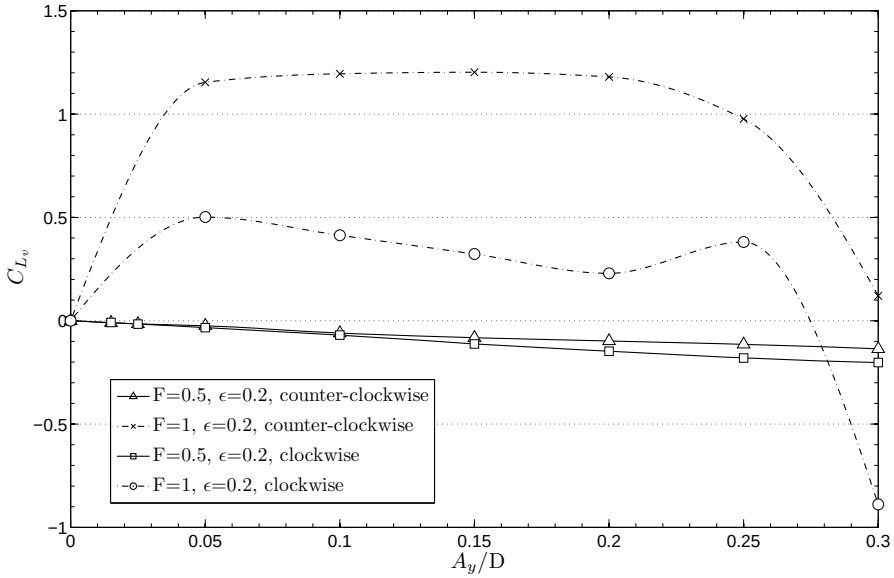

Figure .0.5: Excitation force coefficient C_{L_v} versus nondimensional excitation y-amplitude for $\epsilon = 0.2$ ("clockwise and "counter-clockwise" mode): $F = 0.5$ (sub-harmonic excitation), $F = 1$ (resonant excitation).

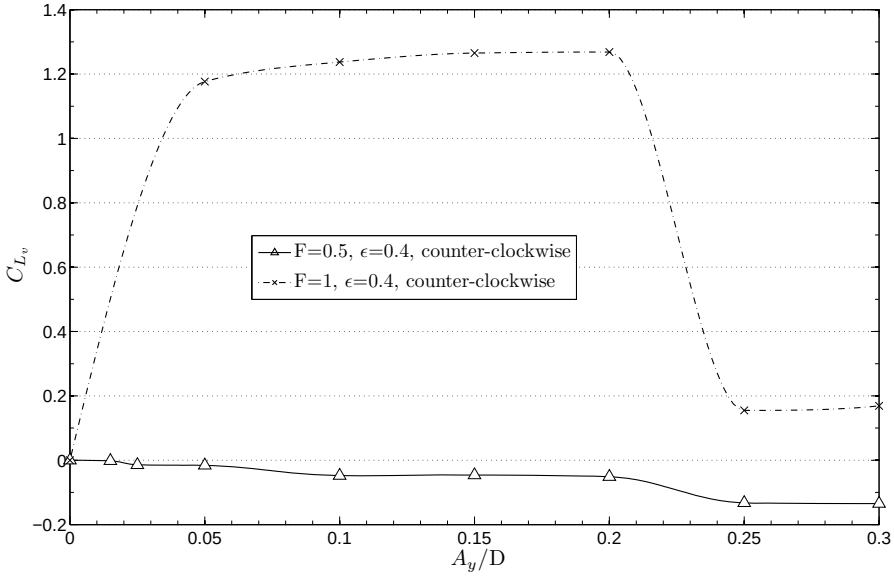

Figure .0.6: Excitation force coefficient C_{L_v} versus nondimensional excitation y-amplitude for $\epsilon = 0.4$ ("counter-clockwise" mode): $F = 0.5$ (sub-harmonic excitation), $F = 1$ (resonant excitation).

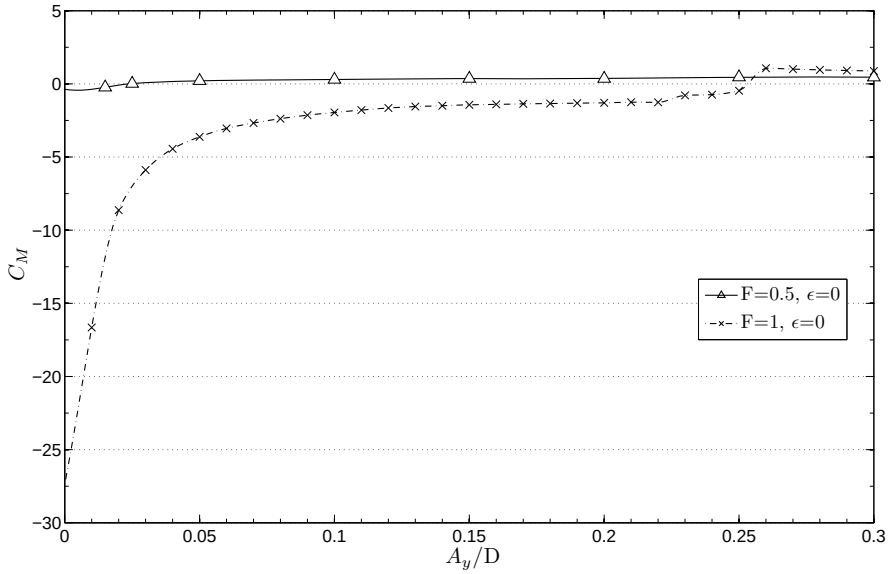

Figure .0.7: Inertia force coefficient C_M versus nondimensional excitation y-amplitude for $\epsilon = 0$: $F = 0.5$ (sub-harmonic excitation), $F = 1$ (resonant excitation).

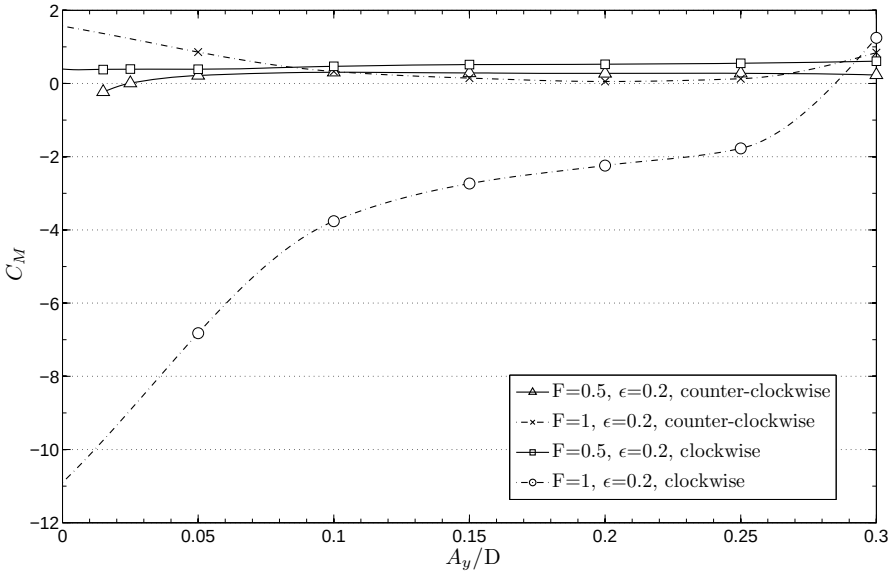

Figure .0.8: Inertia force coefficient C_M versus nondimensional excitation y-amplitude for $\epsilon = 0.2$ ("clockwise and "counter-clockwise" mode): $F = 0.5$ (sub-harmonic excitation), $F = 1$ (resonant excitation).

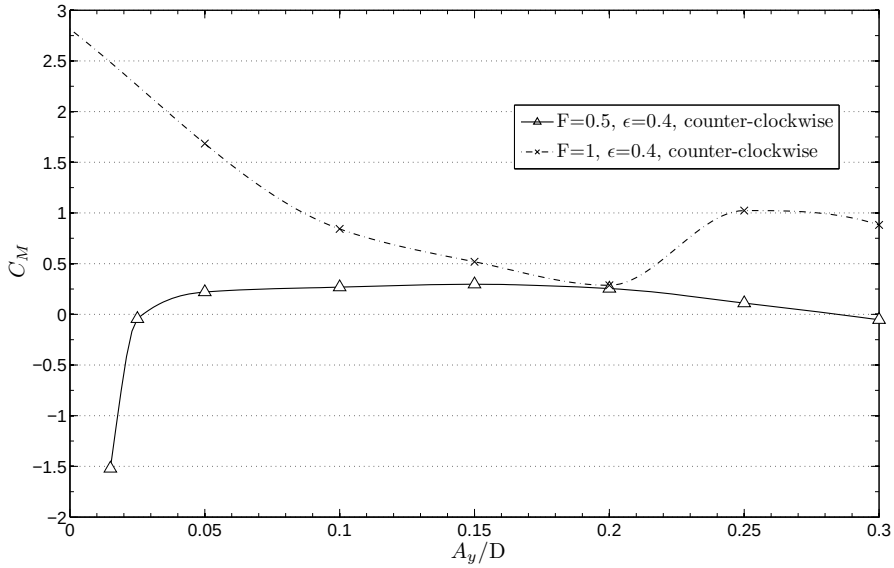

Figure .0.9: Inertia force coefficient C_M versus nondimensional excitation y-amplitude for $\epsilon = 0.4$ ("counter-clockwise" mode): $F = 0.5$ (sub-harmonic excitation), $F = 1$ (resonant excitation).

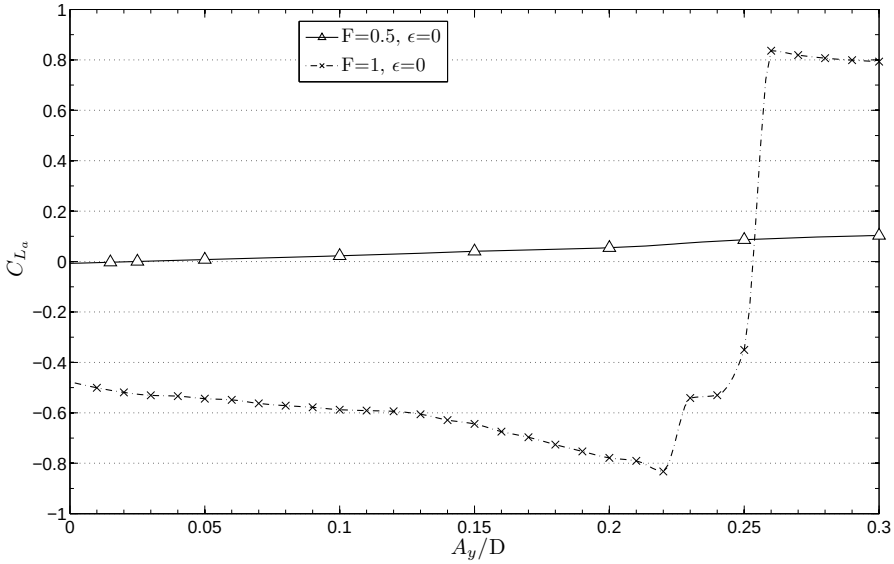

Figure .0.10: Inertia force coefficient C_{L_a} versus nondimensional excitation y-amplitude for $\epsilon = 0$: $F = 0.5$ (sub-harmonic excitation), $F = 1$ (resonant excitation).

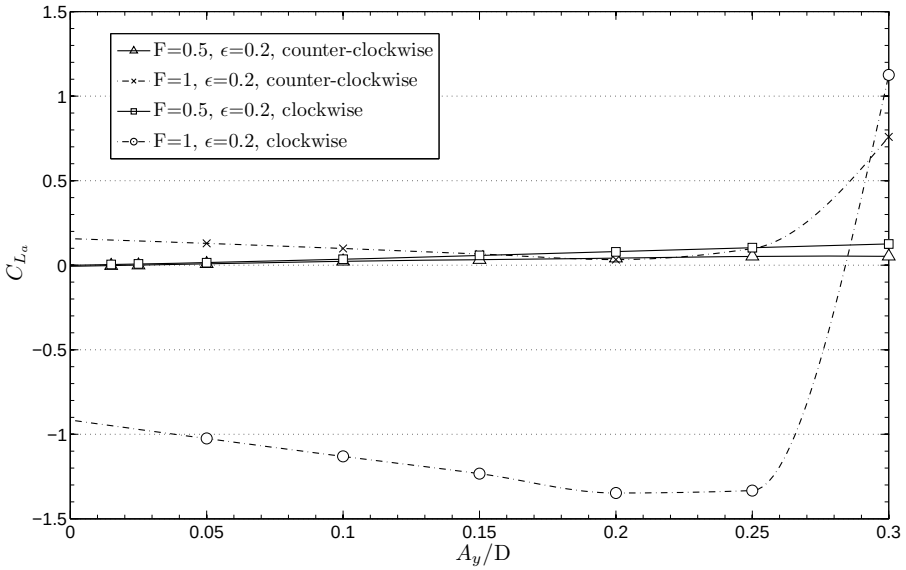

Figure .0.11: Inertia force coefficient C_{L_a} versus nondimensional excitation y-amplitude for $\epsilon = 0.2$ ("clockwise and "counter-clockwise" mode): $F = 0.5$ (sub-harmonic excitation), $F = 1$ (resonant excitation).

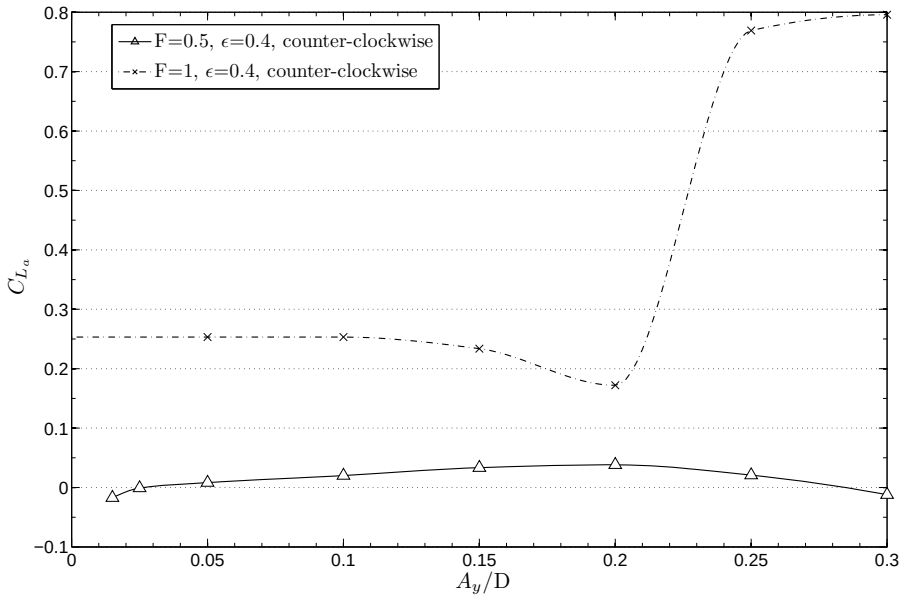

Figure .0.12: Inertia force coefficient C_{L_a} versus nondimensional excitation y-amplitude for $\epsilon = 0.4$ ("counter-clockwise" mode): $F = 0.5$ (sub-harmonic excitation), $F = 1$ (resonant excitation).